Supporting information

Eu(III)-dilution of Er(III) and Yb(III) molecular nanomagnets as a route for improving magnetic features and linking with optical thermometry

Aleksander Hoffman,[a,b] Maja Romanowska,[a] Mikolaj Zychowicz,[a,b] Sebastian Baś,[a]
Jakub J. Zakrzewski[a] and Szymon Chorazy*[a]

[a]Faculty of Chemistry, Jagiellonian University, Gronostajowa 2, 30-387 Kraków, Poland

[b]Doctoral School of Exact and Natural Sciences, Jagiellonian University, Łojasiewicza 11, 30-348 Kraków, Poland

*Corresponding author: simon.chorazy@uj.edu.pl

Experimental section

Materials

Europium(III) trifluoromethanesulfonate, $Eu^{III}(CF_3SO_3)_3$ (or $Eu^{III}(OTf)_3$), erbium(III) trifluoromethanesulfonate, $Er^{III}(CF_3SO_3)_3$ (or $Er^{III}(OTf)_3$), ytterbium(III) trifluoromethanesulfonate, $Yb^{III}(CF_3SO_3)_3$ (or $Yb^{III}(OTf)_3$), and potassium dicyanidoargentate, $K[Ag^{I}(CN)_2]$, were purchased from Sigma-Aldrich (Merck), while bis(diphenylphosphino)methane (dppm) was purchased from TCI (Tokyo Chemical Industry) Chemicals. All other reagents and solvents were purchased from Sigma-Aldrich or TCI Chemicals and used as received unless stated otherwise.

Synthesis of bis(diphenylphosino)methane dioxide (dppmO$_2$)

This organic ligand of bis(diphenylphosino)methane dioxide (dppmO$_2$) was synthesized by adapting the previously reported procedure.[S1] In a two-neck flask, an organic dppm precursor (5.00 g, 26.01 mmol) was placed and dissolved in the mixture of DCM (dichlorometane, 140 mL) and MeOH (methanol, 60 mL). Then, the reaction mixture was cooled to –78 °C (using a dry ice/acetone bath), and an ozone and oxygen gas mixture, generated by the Prozonex ozone generator system, was passed through it (oxygen flow of 4 mL/min, power 70%). The reaction was carried out until the solution turned colour to light blue, leading to full conversion of the substrate. Full conversion of the substrate was confirmed by the TLC analysis (hexane/ethyl acetate, 1:4 v/v). After completion, the reaction mixture was warmed to room temperature (RT) and purged with argon before further handling. Then, the solvent was evaporated to dryness, and the resulting precipitate was dried on a vacuum pump, obtaining a pure, white crystalline product of dppmO$_2$. Yield: 5.36 g (99%). The structure and purity of the obtained product were checked by NMR, IR, and ESI-MS studies.

^{1}H NMR (600 MHz, chloroform-d): δ 7.81 – 7.66 (m, 8H), 7.43 – 7.37 (m, 4H), 7.34 – 7.27 (m, 8H), 3.59 (t, J = 14.7 Hz, 2H).

^{13}C NMR (151 MHz, chloroform-d): δ 132.9 (s), 132.2 (s), 131.8 (s), 131.4 – 130.7 (m), 128.4 (p, J = 7,1 Hz).

^{31}P NMR (121 MHz, chloroform-d): δ 25.08 (s),

IR v: 3318, 3053, 2925, 1589, 1437, 1205, 1189, 780, 741, 699 [cm^{-1}].

LC-MS (ESI) [M+1] = 417 m/z .

General procedure for the synthesis of EuAg, ErAg, YbAg, Er@EuAg, and Yb@EuAg

The organic ligand, dppmO$_2$ (100.0 mg, 0.24 mmol, 3.0 eq.), $Ln^{III}(OTf)_3$ (0.08 mmol, 1.0 eq.), and $K[Ag^{I}(CN)_2]$ (15.9 mg, 0.08 mmol, 1.0 eq.) were dissolved together in the mixture of acetonitrile (3 mL) and methanol (3 mL), and layered with an excess of diethyl ether. After a few days, the crystals of the respective compound formed. Then, they were filtered and washed with Et_2O, distilled water, Et_2O, and dried in air.

Synthesis of EuAg

EuAg was synthesized using the general procedure described above, taking $Eu^{III}(OTf)_3$ as a lanthanide precursor. This results in colorless crystals obtained with an 85% yield. Their composition, $\{[Eu^{III}(dppmO_2)_3][Ag^{I}(CN)_2]\}[OTf]_2 \cdot 0.5MeOH$ (M_W = 1875.21 g·mol^{-1}), was determined by the SC-XRD analysis, while the phase purity and its air stability were proven by the P-XRD method (Fig. S8). Upon exposure of **EuAg** to an air atmosphere, a loss of MeOH molecules occurs, which does not cause any significant structural transformation, as was confirmed by the P-XRD results, CHNS elemental analysis, and TG experiment (Fig. S2). Elemental analysis calculated for the air stable form, $\{[Eu^{III}(dppmO_2)_3][Ag^{I}(CN)_2]\}[OTf]_2$ (M_W = 1859.18 g·mol^{-1}): C, 51.0%; H, 3.6%; N, 1.5%; S, 3.5%. Found: C, 50.9%; H, 3.7%, N, 1.6%; S, 3.1%. IR spectrum (Fig. S1), the bands of $C{\equiv}N^-$ stretching vibrations, located at 2170 cm^{-1} and 2160 cm^{-1}, indicate the presence of bridging cyanido ligands.[S2]

Synthesis of ErAg

ErAg was synthesized using the general procedure described above, taking $Er^{III}(OTf)_3$ as a lanthanide precursor. This results in colorless crystals obtained with an 82% yield. Their composition, $\{[Er^{III}(dppmO_2)_3][Ag^{I}(CN)_2]\}[OTf]_2 \cdot 0.5MeOH$ (M_W = 1887.09 g·mol^{-1}), was determined by the SC-XRD analysis, while the phase purity and its air stability were proven by the P-XRD method (Fig. S8). Upon exposure of **ErAg** to an air atmosphere, a loss of MeOH molecules occurs, which does not cause any significant structural transformation, as was confirmed by the P-XRD results, CHNS elemental analysis, and TG experiment (Fig. S2). Elemental analysis calculated for the air stable form, $\{[Er^{III}(dppmO_2)_3][Ag^{I}(CN)_2]\}[OTf]_2$ (M_W = 1874.48 g·mol^{-1}): C, 50.6%;

H, 3.6%; N, 1.5%; S, 3.4%. Found: C, 50.3%; H, 3.7%, N, 1.8%; S, 3.4%. IR spectrum (Fig. S1), the bands of C≡N$^-$ stretching vibrations, located at 2170 cm^{-1} and 2160 cm^{-1}, indicate the presence of bridging cyanido ligands.[S2]

Synthesis of YbAg

YbAg was synthesized using the general procedure described above, taking Yb^{III}(OTf)$_3$ as a lanthanide precursor. This results in colorless crystals obtained with a 78% yield. Their composition, {[Yb^{III}(dppmO$_2$)$_3$][Ag^I(CN)$_2$]}[OTf]$_2$·0.5MeOH (M_W = 1896.29 g·mol^{-1}), was determined by the SC-XRD analysis, while the phase purity and its air stability were proven by the P-XRD method (Fig. S8). Upon exposure of **YbAg** to an air atmosphere, a loss of MeOH molecules occurs, which does not cause any significant structural transformation, as was confirmed by the P-XRD results, CHNS elemental analysis, and TG experiment (Fig. S2). Elemental analysis calculated for the air stable form, {[Yb^{III}(dppmO$_2$)$_3$][Ag^I(CN)$_2$]}[OTf]$_2$ (M_W = 1880.27 g·mol^{-1}): C, 50.5%; H, 3.5%; N, 1.5%; S, 3.4%. Found: C, 50.1%; H, 3.7%, N, 1.2%; S, 3.5%. IR spectrum (Fig. S1), the bands of C≡N$^-$ stretching vibrations, located at 2170 cm^{-1} and 2160 cm^{-1}, indicate the presence of bridging cyanido ligands.[S2]

Synthesis of Er@EuAg

Er@EuAg was synthesized using a modified general procedure, taking the proper mixture of Er^{III}(OTf)$_3$ (4.9 mg, 0.008 mmol, 0.1 eq.) and Eu^{III}(OTf)$_3$ (43.1 mg, 0.072 mmol, 0.9 eq.), which gives the 9:1 molar ratio for lanthanide ions. This results in colorless crystals with a 75% yield. Their composition, {[Eu$^{III}_{0.95}$Er$^{III}_{0.05}$(dppmO$_2$)$_3$][Ag^I(CN)$_2$]}[OTf]$_2$·0.5MeOH (M_W = 1875.97 g·mol^{-1}), was determined by the SC-XRD analysis and SEM-EDX measurements (Table S9), while the phase purity and its air stability were proven by the P-XRD method (Fig. S8). Upon exposure of **Er@EuAg** to an air atmosphere, a loss of MeOH molecules occurs, which does not cause any significant structural transformation, as was confirmed by the P-XRD results, CHNS elemental analysis, and TG experiment (Fig. S2). Elemental analysis calculated for the air stable form, {[Eu$^{III}_{0.95}$Er$^{III}_{0.05}$(dppmO$_2$)$_3$][Ag^I(CN)$_2$]}[OTf]$_2$ (M_W = 1859.95 g·mol^{-1}): C, 51.0%; H, 3.6%; N, 1.5%; S, 3.5%. Found: C, 50.4%; H, 3.6%, N, 1.6%; S, 3.3%. IR spectrum (Fig. S1), the bands of C≡N$^-$ stretching vibrations, located at 2170 cm^{-1} and 2160 cm^{-1}, indicate the presence of bridging cyanido ligands.[S2]

Synthesis of Yb@EuAg

Yb@EuAg was synthesized using a modified general procedure, taking the proper mixture of Yb^{III}(OTf)$_3$ (5.0 mg, 0.008 mmol, 0.1 eq.) and Eu^{III}(OTf)$_3$ (43.1 mg, 0.072 mmol, 0.9 eq.), which gives the 9:1 molar ratio. This results in colorless crystals with a 77% yield. Their composition, {[Eu$^{III}_{0.96}$Yb$^{III}_{0.04}$(dppmO$_2$)$_3$][Ag^I(CN)$_2$]}[OTf]$_2$·0.5MeOH (M_W = 1874.92 g·mol^{-1}), was determined by the SC-XRD analysis and SEM-EDX measurements (Table S10), while the phase purity and its air stability were proven by the P-XRD method (Fig. S8). Upon exposure of **Yb@EuAg** to an air atmosphere, a loss of MeOH molecules occurs, which does not cause any significant structural transformation, as was confirmed by the P-XRD results, CHNS elemental analysis, and TG experiment (Fig. S2). Elemental analysis calculated for the air stable form, {[Eu$^{III}_{0.96}$Yb$^{III}_{0.04}$(dppmO$_2$)$_3$][Ag^I(CN)$_2$]}[OTf]$_2$ (M_W = 1858.91 g·mol^{-1}): C, 51.0%; H, 3.6%; N, 1.5%; S, 3.5%. Found: C, 50.8%; H, 3.7%, N, 1.7%; S, 3.3%. IR spectrum (Fig. S1), the bands of C≡N$^-$ stretching vibrations, located at 2170 cm^{-1} and 2160 cm^{-1}, indicate the presence of bridging cyanido ligands.[S2]

Structural studies

The single crystal X-ray diffraction (SC-XRD) data for **EuAg**, **ErAg**, **YbAg**, **Er@EuAg**, and **Yb@EuAg** were collected using a Bruker D8 Venture diffractometer, equipped with a Photon III CPAD detector, Mo Kα (0.71073 Å) INCOATEC IµS 3.0 microfocus sealed tube radiation source, Helios® optics, and Oxford Cryostream 800 Plus low temperature device. The single crystals for **EuAg**, **ErAg**, **YbAg**, **Er@EuAg**, and **Yb@EuAg** were selected for the SC-XRD experiment directly from the mother solution, covered in Apiezon® N grease, mounted on the Micro Mounts™ holder, and measured at 100(2) K. The SAINT and SADABS programs were used for data reduction and cell refinement processes. The absorption correction was established using a multi-scan procedure using the SADABS program.[S3] The crystal structures were solved by an intrinsic phasing method using the SHELXT program within the Apex4 package.[S3,S4] The further crystal structure refinement was carried out by a weighted full-matrix least squares method on an F^2 factor of SHELX-2014/7 within WinGX (ver. 2018.3) software.[S4,S5] All non-hydrogen atoms were refined anisotropically. Hydrogen atoms were refined isotropically; those belonging to the metal complexes were calculated in their idealized positions. Due to the partial occupancy of MeOH molecules that appeared in the large structural disorder, their positions were not localized. A riding model was used for the further refinement of all hydrogen atoms. Some restraints of the

DFIX and ISOR types were applied for non-hydrogen atoms to ensure the proper geometry of selected molecular components. DELU and SIMU restraints were applied for the MeOH molecule and triflate anions in **EuAg** and **YbAg** to ensure the convergence of the refinement procedure. Some of the reflections with intensities endowed with large experimental errors (affected by the X-ray beam) were removed from the final refinement using the OMIT command. Using all of these procedures, satisfactory refinement parameters were achieved. The CCDC numbers for **EuAg**, **ErAg**, **YbAg**, **Er@EuAg**, and **Yb@EuAg** are 2454863, 2454864, 2454865, 3454866, and 2454867, respectively. Details of the crystal data and refinement of the structure are summarized in Table S1, while representative structural parameters are gathered in Tables S2–S6. The structural figures (Fig. S3–S7) were prepared using the Mercury 4.0 software.[S6] Powder XRD (P-XRD) data were collected using a Bruker D8 Advance Eco powder diffractometer equipped with a Cu Kα (1.5419 Å) radiation source. The P-XRD measurements were conducted at room temperature for the dried polycrystalline samples, inserted into 0.7 mm diameter glass capillaries using the appropriate experimental setup for a rotating capillary geometry.

Physical techniques

All physical measurements, discussed below, were performed on freshly prepared and filtered samples. All ^{1}H and ^{13}C NMR spectra were recorded at room temperature using a Bruker AVANCE III 600 MHz spectrometer, while ^{31}P NMR spectra were recorded at room temperature using a Bruker AVANCE II 300 MHz spectrometer. CHNS elemental analyses were performed with standard microanalysis procedures using an Elementar Vario Micro Cube CHNS analyzer. The infrared (IR) absorption spectra for **EuAg**, **ErAg**, **YbAg**, **Er@EuAg**, and **Yb@EuAg** were collected on a Thermo Scientific Nicolet iN10 MX FT-IR microscope in transmission mode in the 3800−670 cm^{-1} range for the selected single crystals placed on BaF_2 windows, while for dppmO$_2$ ligand the analogous spectra were collected on a FT-IR Thermo Scientific Nicolet 6700 spectrometer in the 3850−650 cm^{-1} range. Additional IR spectra (enabling the broader wavenumber range) for **EuAg**, **ErAg**, **YbAg**, **Er@EuAg**, and **Yb@EuAg** were collected on the respective polycrystalline samples using a Thermo Scientific Nicolet iS5 FT-IR Spectrometer, equipped with an iD7 ATR accessory (monolithic diamond) in the 4000−400 cm^{-1} range. It was found that the uncorrected spectra were more convenient for discussing the small differences between the compounds, and these are presented. Thermogravimetric (TG) measurements were performed on a NETZSCH TG 209 F1 Libra apparatus under inert gas (N_2) at a heating rate of 1 $°C \cdot min^{-1}$ in the temperature range of 20–380 °C. Solid-state UV-vis absorption spectra were measured in the 200−700 nm range on a Shimadzu UV-3600i plus spectrometer using the thin films of powder samples inserted between two quartz plates. Solid-state photoluminescent (PL) properties were investigated using an FS5 spectrofluorometer equipped with an Xe (150 W) arc lamp as an excitation source and a Hamamatsu photomultiplier of the R928P type as a detector. Emission lifetime measurements were conducted on the FS5 spectrofluorometer using a time-correlated single photon counting method with a 5 W μs-flashlamp. The temperature-dependent emission and excitation spectra, as well as emission decay profiles, were collected using a CS204SI-FMX-1SS cooling power optical He cryostat equipped with DE-204SI closed cycle cryocooler (cold head), water-cooled compressor (ARS-4HW model), and a model 335 cryogenic temperature controller attached to the FS5 spectrofluorometer via SC-80 Cryostat Module. For all types of temperature-dependent PL studies, freshly prepared polycrystalline ground samples were packed in thin heat-sealed PE foil (0.02 mm), covered with a minimal amount of silicon grease (type C), and placed between two quartz plates. Absolute luminescence quantum yields (QY) were determined by a direct excitation method using an integrating sphere module (SC-30) and $LaCl_3 \cdot 6H_2O$ as a reference material.[S7] Emission background corrections were performed within the Fluoracle software (Edinburgh Instruments). Investigation of magnetic properties was performed using a Quantum Design MPMS-3 Evercool magnetometer. For magnetic studies, the powder samples were packed in the capsule, covered by a small amount of paraffin oil and cotton, and placed in plastic straws. Diamagnetic corrections for the sample, paraffin oil, and the sample holder were taken into account.

Calculations

Continuous Shape Measure (CShM) analyses for metal complexes in the **EuAg**, **ErAg**, **YbAg**, **Er@EuAg**, and **Yb@EuAg** were performed using the SHAPE software ver. 2.1.21.[S8] The detailed analysis of *ac* magnetic data, including the determination of magnetic relaxation times from the simultaneous fitting of all *ac* magnetic characteristics (frequency dependences of out-of-phase and in-phase magnetic susceptibilities together with the related Argand plots) using models for complex-valued *ac* susceptibility at the indicated conditions of *dc* magnetic field and temperature, as well as further determination of final parameters of operating relaxation processes from the simultaneous 3-D fitting of temperature- and field-dependences of relaxation times, were performed using the relACs program.[S9] For details of the *ab initio* calculations, see page S33 (below).

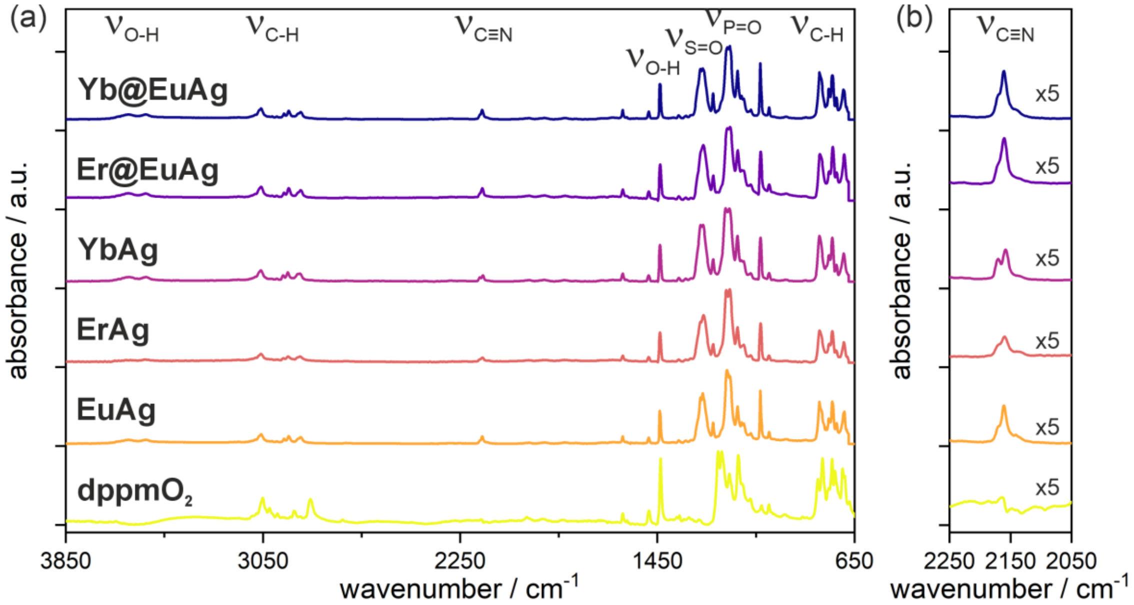

Fig. S1 Infrared (IR) absorption spectra of the selected crystals of **EuAg**, **ErAg**, **YbAg**, **Er@EuAg**, and **Yb@EuAg**, compared with the analogous spectrum of dppmO$_2$ ligand presented in the 3850–650 cm^{-1} range (a) and the enlarged spectra for the limited 2250–2050 cm^{-1} range containing characteristic stretching modes of bridging cyanido ligands (b).[S2]

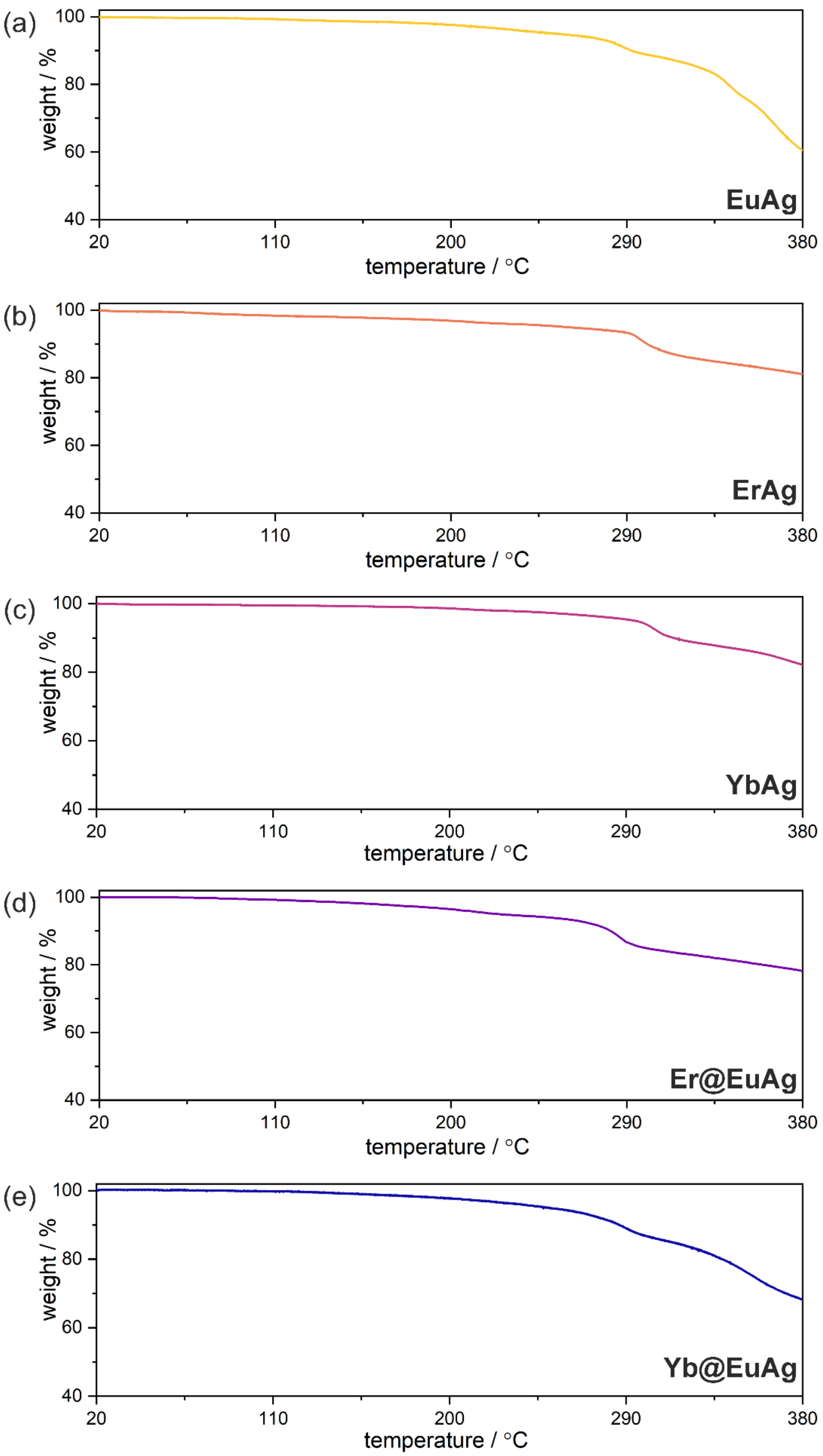

Fig. S2 Thermogravimetric (TG) curves of **EuAg** (a), **ErAg** (b), **YbAg** (c), **Er@EuAg** (d), and **Yb@EuAg** (e), collected in the 20–380 °C temperature range.

Table S1 Crystal data and structure refinement parameters for **EuAg**, **ErAg**, **YbAg**, **Er@EuAg**, and **Yb@EuAg**.

Compound	**EuAg**	**ErAg**	**YbAg**	**Er@EuAg**	**Yb@EuAg**
Formula	$C_{159}H_{132}Ag_2Eu_2F_{12}N_4O_{25}P_{12}S_4$	$C_{159}H_{132}Ag_2Er_2F_{12}N_4O_{25}P_{12}S_4$	$C_{159}H_{132}Ag_2F_{12}N_4O_{25}P_{12}S_4Yb_2$	$C_{159}H_{132}Ag_2Er_{0.10}Eu_{1.90}F_{12}N_4O_{25}P_{12}S_4$	$C_{159}H_{132}Ag_2Eu_{1.92}F_{12}N_4O_{25}P_{12}S_4Yb_{0.08}$
Formula weight / g·mol^{-1}	3746.25	3776.83	3788.39	3747.78	3747.94
T / K	100(2)				
λ / Å	0.71073 (Mo Kα)				
Crystal system	triclinic	triclinic	triclinic	triclinic	triclinic
Space group	$P\bar{1}$	$P\bar{1}$	$P\bar{1}$	$P\bar{1}$	$P\bar{1}$
a / Å	11.112(3)	11.0523(6)	11.0554(4)	11.0368(2)	11.106(3)
b / Å	14.682(4)	14.6703(8)	14.6220(5)	14.6552(3)	14.701(5)
c / Å	25.121(6)	25.1417(13)	25.1213(9)	25.1310(7)	25.114(7)
α / °	85.939(7)	86.331(2)	86.1550(10)	86.2950(10)	86.195(8)
β / °	87.260(7)	86.941(2)	86.7200(10)	86.8580(10)	87.427(7)
γ / °	83.100(7)	83.433(2)	83.4230(10)	83.4710(10)	83.222(8)
V / Å^3	4055.0(17)	4037.1(4)	4020.1(2)	4025.43(16)	4060(2)
Z	1	1	1	1	1
Density / g·cm^{-1}	1.534	1.554	1.565	1.547	1.533
Absorption coefficient / cm^{-1}	1.252	1.521	1.645	1.288	1.266
F(000)	1886	1896	1900	1887	1886.6
Θ range / °	1.848–25.026	2.082–25.027	2.064–25.026	2.083–25.026	1.991–25.027
Limiting indices	$-11 < h < 13$ $-17 < k < 17$ $-29 < l < 29$	$-12 < h < 13$ $-17 < k < 17$ $-29 < l < 29$	$-13 < h < 12$ $-17 < k < 17$ $-29 < l < 29$	$-13 < h < 12$ $-17 < k < 17$ $-29 < l < 29$	$-13 < h < 13$ $-17 < k < 17$ $-29 < l < 29$
Collected reflections	50687	65104	67892	69976	35287
R_{int}	0.0622	0.0368	0.0397	0.0576	0.1146
Completeness / %	98.5	99.7	99.7	99.9	99.8
Data/restraints/parameters	14129/14/1000	14215/1/1000	14163/8/1000	14212/44/1000	14320/37/1000
GOF on F^2	1.074	1.064	1.035	1.068	1.021
Final R indices (R_1 for $[I > 2\sigma(I)]$ wR_2 for all data)	$R_1 = 0.044$ $wR_2 = 0.1151$	$R_1 = 0.0413$ $wR_2 = 0.1021$	$R_1 = 0.0334$ $wR_2 = 0.0848$	$R_1 = 0.0484$ $wR_2 = 0.1207$	$R_1 = 0.0772$ $wR_2 = 0.1779$
Largest diff. peak and hole /e·Å^{-3}	2.182/–1.811	3.801/–1.773	2.689/–2.200	4.882/–1.555	2.425/–2.607

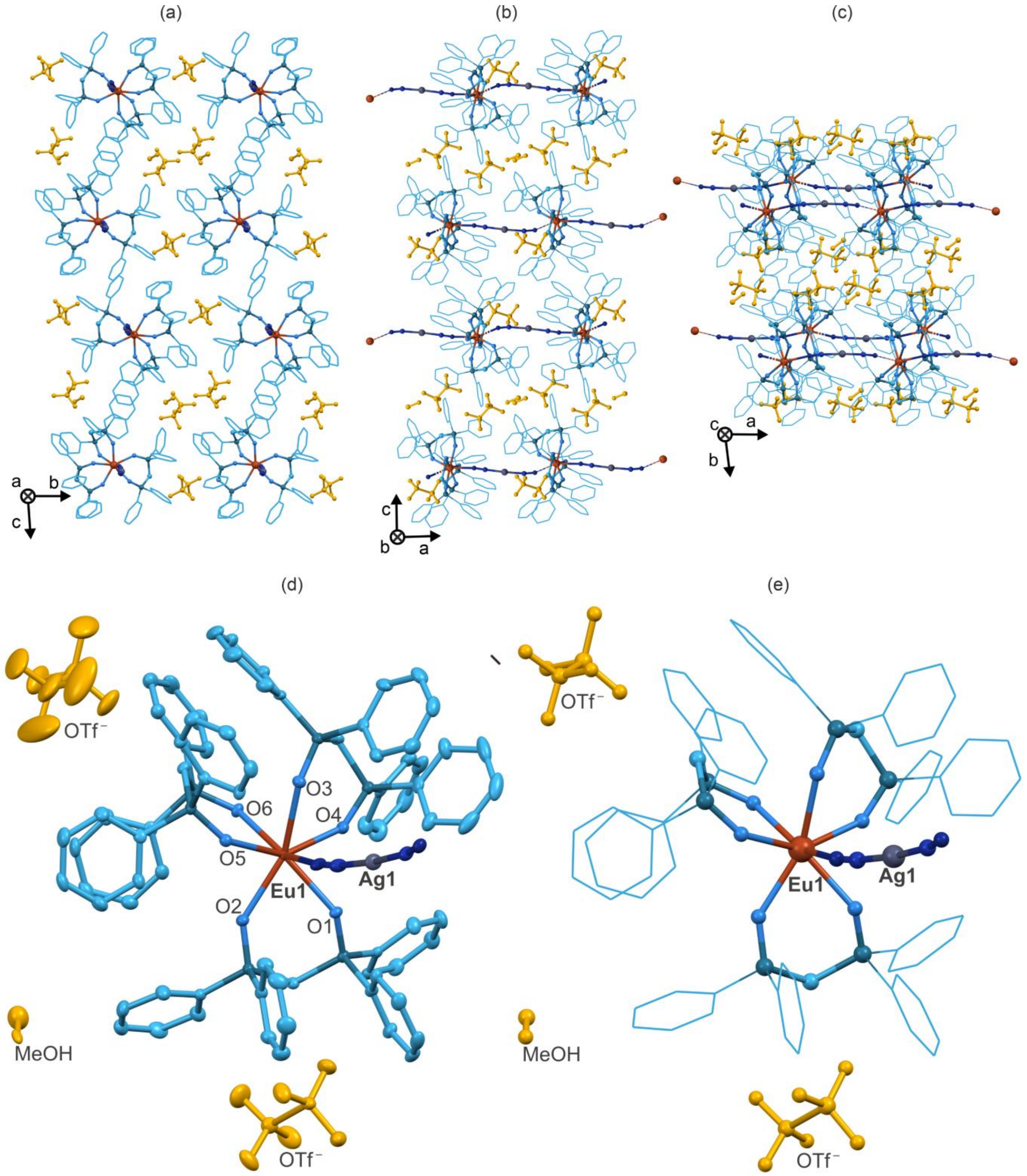

Fig. S3 The representative views of the crystal structure of **EuAg** along the main *a*, *b*, and *c* crystallographic axes (a−c, respectively), the asymmetric unit containing atoms with their thermal ellipsoids and the labelling scheme for the selected atoms (d), and molecular building unit with labelling scheme for Eu and Ag, triflate anions and solvent molecule of crystallization (e). Thermal ellipsoids in (d) are presented with a 50% probability level. Hydrogen atoms were omitted for clarity. Colours: red = Eu, various hues of blue = dppmO$_2$ ligands, grey = Ag, dark blue = CN$^-$, yellow = triflate anions, and MeOH solvent molecules.

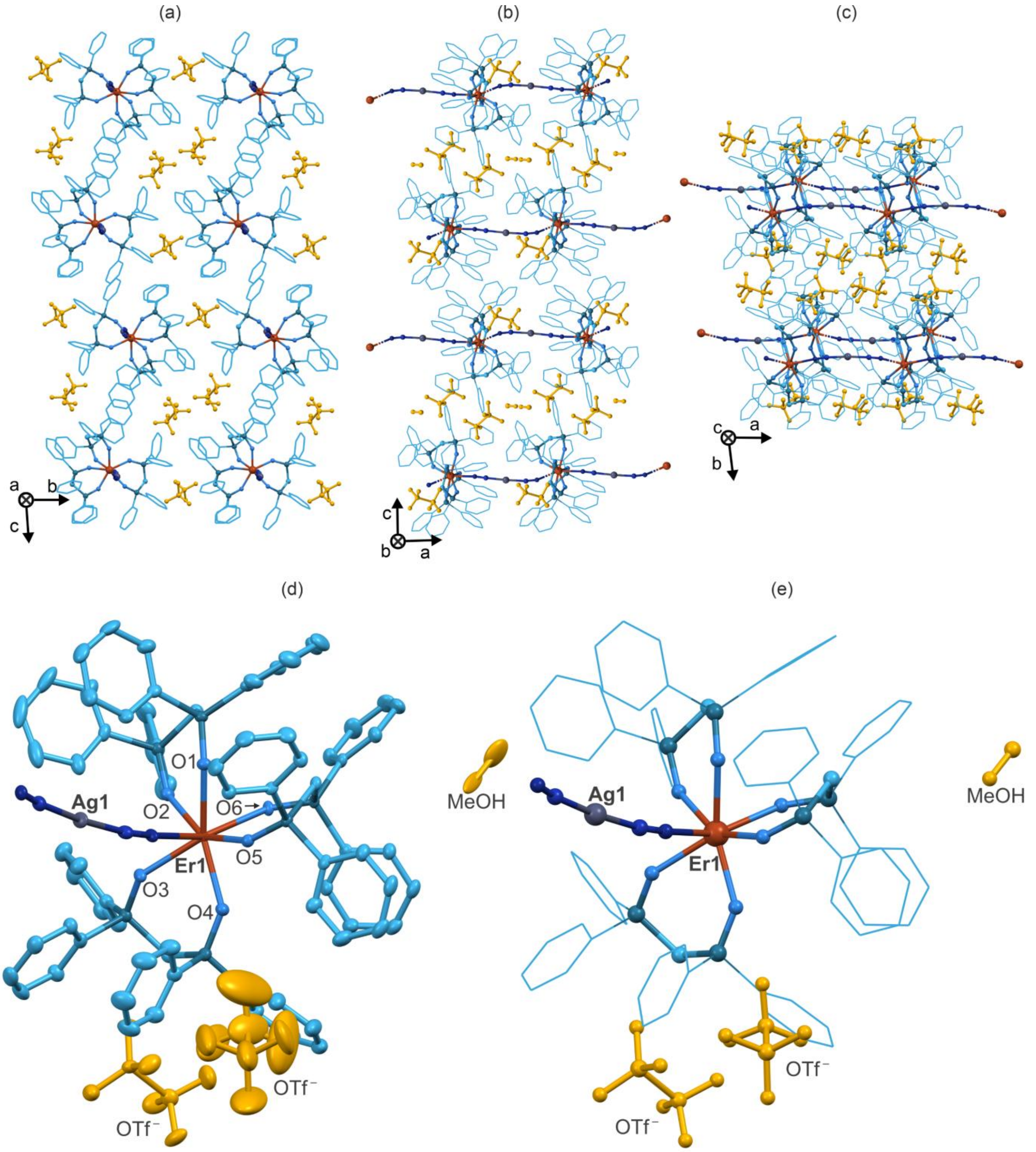

Fig. S4 The representative views of the crystal structure of **ErAg** along the main *a*, *b*, and *c* crystallographic axes (a−c, respectively), the asymmetric unit containing atoms with their thermal ellipsoids and the labelling scheme for the selected atoms (d), and molecular building unit with labelling scheme for Er and Ag, triflate anions, and solvent molecule of crystallization (e). Thermal ellipsoids in (d) are presented with a 50% probability level. Hydrogen atoms were omitted for clarity. Colours: red = Er, various hues of blue = dppmO$_2$ ligands, grey = Ag, dark blue = CN$^-$, yellow = triflate anions, and MeOH solvent molecules.

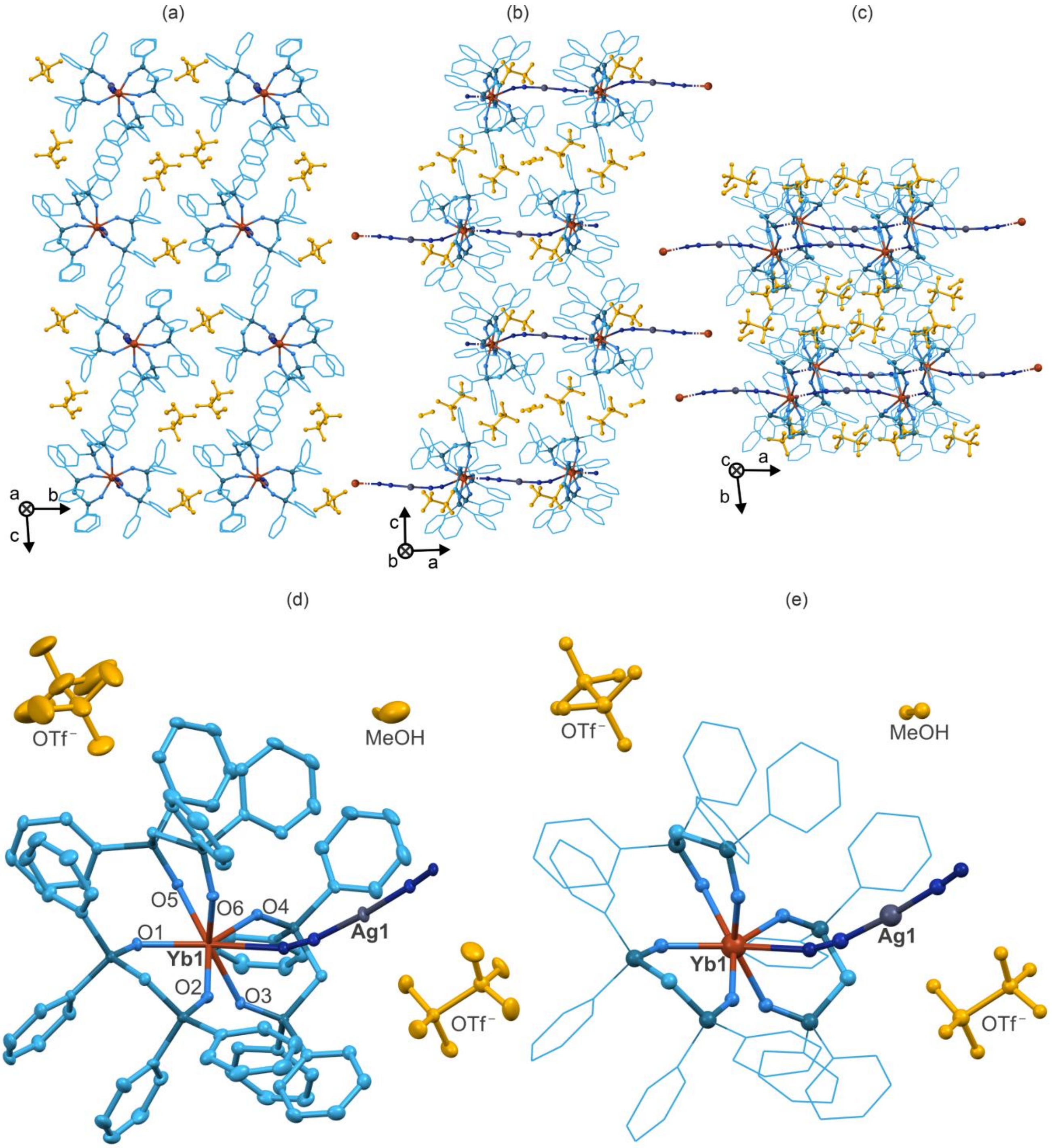

Fig. S5 The representative views of the crystal structure of **YbAg** along the main *a*, *b*, and *c* crystallographic axes (a−c, respectively), the asymmetric unit containing atoms with their thermal ellipsoids and the labelling scheme for the selected atoms (d), and molecular building unit with labelling scheme for Yb and Ag, triflate anions, and solvent molecule of crystallization (e). Thermal ellipsoids in (d) are presented with a 50% probability level. Hydrogen atoms were omitted for clarity. Colours: red = Yb, various hues of blue = dppmO$_2$ ligands, grey = Ag, dark blue = CN$^-$, yellow = triflate anions, and MeOH solvent molecules.

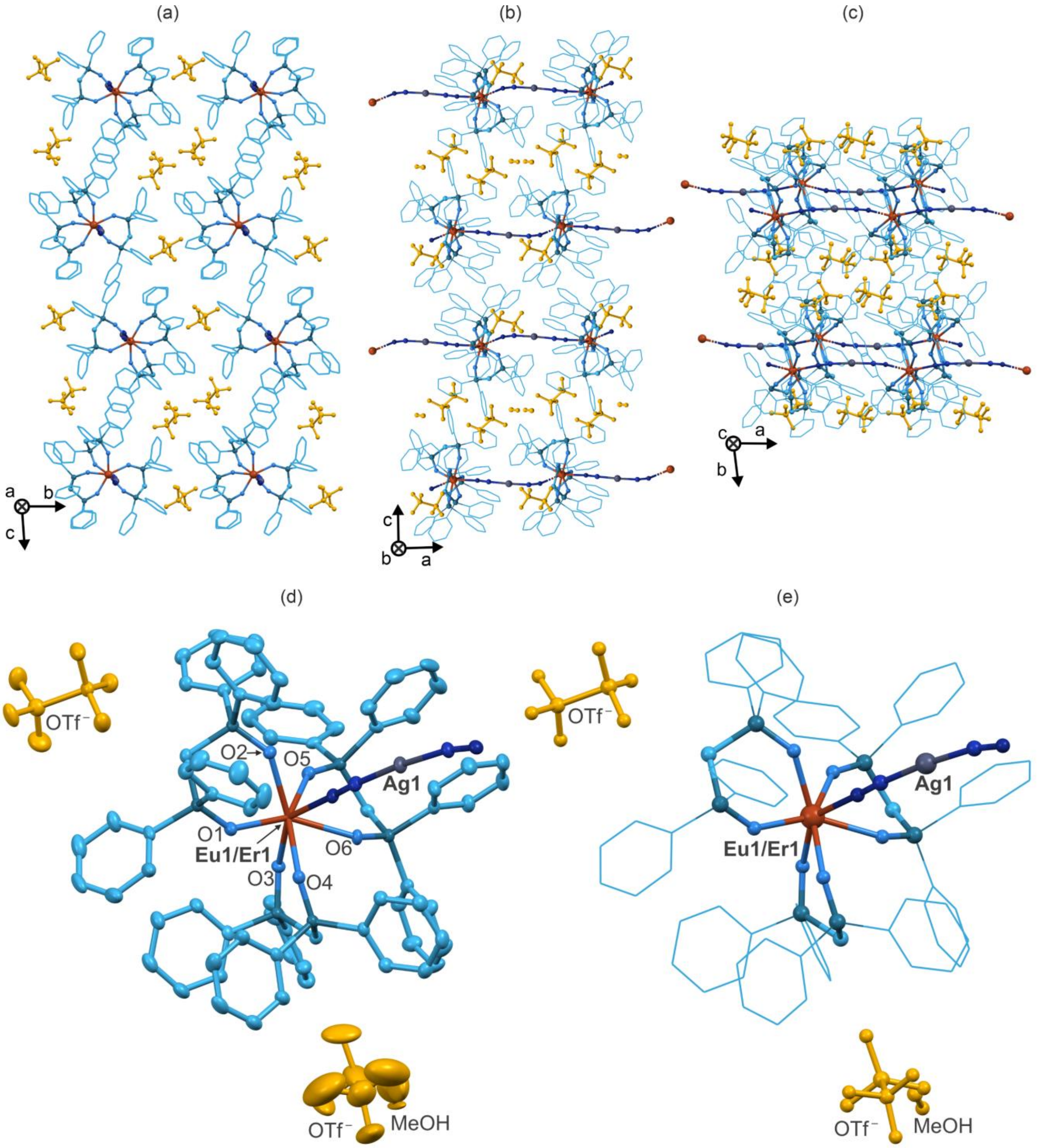

Fig. S6 The representative views of the crystal structure of **Er@EuAg** along the main *a*, *b*, and *c* crystallographic axes (a−c, respectively), the asymmetric unit containing atoms with their thermal ellipsoids and the labelling scheme for the selected atoms (d), and molecular building unit with labelling scheme for Eu, Er and Ag, triflate anions, and solvent molecule of crystallization (e). Thermal ellipsoids in (d) are presented with a 50% probability level. Hydrogen atoms were omitted for clarity. Colours: red = Eu/Er, various hues of blue = dppmO$_2$ ligands, grey = Ag, dark blue = CN$^-$, yellow = triflate anions, and MeOH solvent molecules.

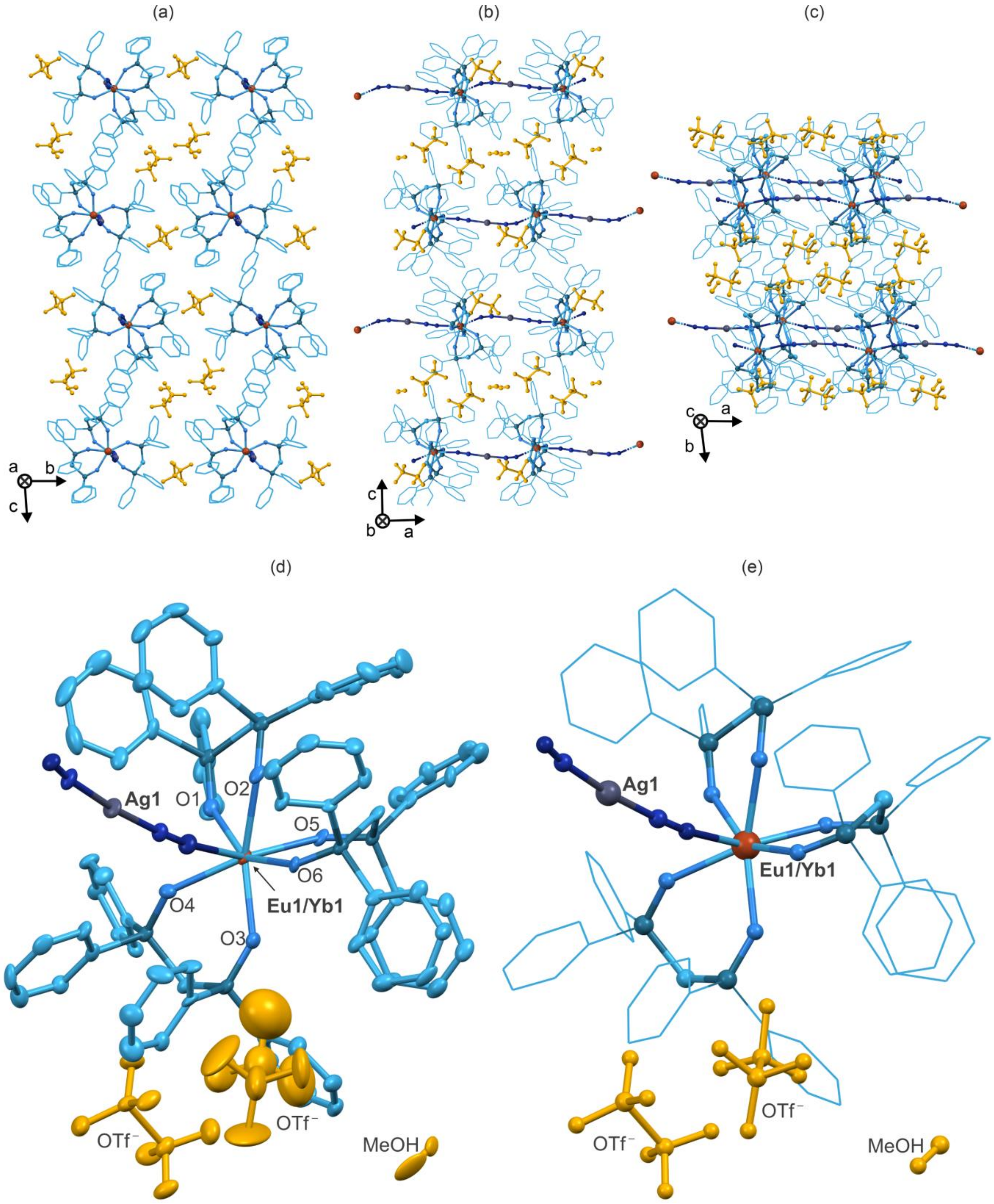

Fig. S7 The representative views of the crystal structure of **Yb@EuAg** along the main *a*, *b*, and *c* crystallographic axes (a−c, respectively), the asymmetric unit containing atoms with their thermal ellipsoids and the labelling scheme for the selected atoms (d), and molecular building unit with labelling scheme for Eu, Yb and Ag, triflate anions, and solvent molecule of crystallization (e). Thermal ellipsoids in (d) are presented with a 50% probability level. Hydrogen atoms were omitted for clarity. Colours: red = Eu/Yb, various hues of blue = dppmO$_2$ ligands, grey = Ag, dark blue = CN$^-$, yellow = triflate anions, and MeOH solvent molecules.

Table S2 Selected detailed structure parameters for **EuAg**.

Selected bond lengths in **EuAg** / Å					
Eu1-O1	2.374(3)	Eu1-O4	2.340(3)	Eu1-N1	2.530(4)
Eu1-O2	2.383(3)	Eu1-O5	2.333(3)	Eu1-N2	2.593(4)
Eu1-O3	2.434(3)	Eu1-O6	2.365(3)	Ag1-C1N	2.038(5)
				Ag1-C2N	2.041(5)
Selected bond angles in **EuAg** / °					
O1-Eu1-O2	74.44(10)	O3-Eu1-O5	76.06(10)	N1-Eu1-O6	144.17(11)
O1-Eu1-O3	123.90(10)	O3-Eu1-O6	76.94(10)	N2-Eu1-O1	75.44(11)
O1-Eu1-O4	75.50(10)	O4-Eu1-O5	147.98(10)	N2-Eu1-O2	72.32(11)
O1-Eu1-O5	131.00(10)	O4-Eu1-O6	88.05(10)	N2-Eu1-O3	133.70(11)
O1-Eu1-O6	146.24(10)	O5-Eu1-O6	76.31(10)	N2-Eu1-O4	72.66(12)
O2-Eu1-O3	148.39(10)	N1-Eu1-O1	69.15(11)	N2-Eu1-O5	125.88(11)
O2-Eu1-O4	138.32(10)	N1-Eu1-O2	93.47(12)	N2-Eu1-O6	71.54(11)
O2-Eu1-O5	73.00(10)	N1-Eu1-O3	73.43(11)	N1-Eu1-N2	144.29(11
O2-Eu1-O6	101.55(11)	N1-Eu1-O4	102.05(12)	C1N-Ag1-C2N	175.30(18)
O3-Eu1-O4	73.24(10)	N1-Eu1-O5	77.36(12)		

Table S3 Selected detailed structure parameters for **ErAg**.

Selected bond lengths in ErAg / Å					
Er1-O1	2.388(3)	Er1-O4	2.322(3)	Er1-N1	2.468(3)
Er1-O2	2.272(3)	Er1-O5	2.289(3)	Er1-N2	2.548(4)
Er1-O3	2.326(3)	Er1-O6	2.311(3)	Ag1-C1N	2.049(5)
				Ag1-C2N	2.045(5)
Selected bond angles in **ErAg** / °					
O1-Er1-O2	73.95(10)	O3-Er1-O5	130.13(10)	N1-Er1-O6	144.05(11)
O1-Er1-O3	124.46(10)	O3-Er1-O6	146.18(10)	N2-Er1-O1	133.24(11)
O1-Er1-O4	147.63(10)	O4-Er1-O5	72.51(10)	N2-Er1-O2	72.67(11)
O1-Er1-O5	75.50(10)	O4-Er1-O6	100.69(11)	N2-Er1-O3	76.27(11)
O1-Er1-O6	76.70(10)	O5-Er1-O6	77.35(10)	N2-Er1-O4	72.48(11)
O2-Er1-O3	75.14(11)	N1-Er1-O1	73.13(11)	N2-Er1-O5	126.22(11)
O2-Er1-O4	138.40(10)	N1-Er1-O2	101.38(12)	N2-Er1-O6	70.62(11)
O2-Er1-O5	148.53(10)	N1-Er1-O3	69.28(11)	N1-Er1-N2	145.33(12)
O2-Er1-O6	88.44(10)	N1-Er1-O4	94.58(11)	C1N-Ag1-C2N	174.72(18)
O3-Er1-O4	75.15(10)	N1-Er1-O5	76.56(11)		

Table S4 Selected detailed structure parameters for **YbAg**.

Selected bond lengths in **YbAg** / Å					
Yb1-O1	2.380(2)	Yb1-O4	2.299(2)	Yb1-N1	2.553(3)
Yb1-O2	2.247(2)	Yb1-O5	2.263(2)	Yb1-N2	2.444(3)
Yb1-O3	2.303(2)	Yb1-O6	2.288(2)	Ag1-C1N	2.044(4)
				Ag1-C2N	2.048(4)
Selected bond angles in **YbAg** / °					
O1-Yb1-O2	74.13(9)	O3-Yb1-O5	130.63(9)	N1-Yb1-O6	70.37(9)
O1-Yb1-O3	124.08(8)	O3-Yb1-O6	145.82(9)	N2-Yb1-O1	73.14(9)
O1-Yb1-O4	147.57(9)	O4-Yb1-O5	72.51(9)	N2-Yb1-O2	101.78(10)
O1-Yb1-O5	75.49(9)	O4-Yb1-O6	100.97(9)	N2-Yb1-O3	69.17(9)
O1-Yb1-O6	76.85(9)	O5-Yb1-O6	77.48(9)	N2-Yb1-O4	94.37(9)
O2-Yb1-O3	74.93(9)	N1-Yb1-O1	133.54(9)	N2-Yb1-O5	76.86(9)
O2-Yb1-O4	138.30(9)	N1-Yb1-O2	72.63(9)	N2-Yb1-O6	144.40(9)
O2-Yb1-O5	148.52(9)	N1-Yb1-O3	76.34(9)	N1-Yb1-N2	145.22(10)
O2-Yb1-O6	87.78(9)	N1-Yb1-O4	72.30(9)	C1N-Ag1-C2N	175.44(15)
O3-Yb1-O4	75.47(9)	N1-Yb1-O5	125.79(9)		

Table S5 Selected detailed structure parameters for **Er@EuAg**.

Selected bond lengths in **Er@EuAg** / Å					
Er1/Eu1-O1	2.302(4)	Er1/Eu1-O4	2.273(4)	Er1/Eu1-N1	2.438(5)
Er1/Eu1-O2	2.308(4)	Er1/Eu1-O5	2.249(4)	Er1/Eu1-N2	2.543(5)
Er1/Eu1-O3	2.278(4)	Er1/Eu1-O6	2.380(4)	Ag1-C1N	2.052(6)
				Ag1-C2N	2.037(6)
Selected bond angles in **Er@EuAg** / °					
O1-Er1/Eu1-O2	75.54(13)	O3-Er1/Eu1-O5	88.14(13)	N1-Er1/Eu1-O6	73.06(14)
O1-Er1/Eu1-O3	100.29(13)	O3-Er1/Eu1-O6	76.89(13)	N2-Er1/Eu1-O1	72.10(14)
O1-Er1/Eu1-O4	72.47(13)	O4-Er1/Eu1-O5	148.64(13)	N2-Er1/Eu1-O2	76.15(14)
O1-Er1/Eu1-O5	138.27(13)	O4-Er1/Eu1-O6	75.54(13)	N2-Er1/Eu1-O3	70.53(14)
O1-Er1/Eu1-O6	147.70(13)	O5-Er1/Eu1-O6	74.03(13)	N2-Er1/Eu1-O4	126.33(14)
O2-Er1/Eu1-O3	145.92(13)	N1-Er1/Eu1-O1	95.14(14)	N2-Er1/Eu1-O5	72.56(14)
O2-Er1/Eu1-O4	130.07(13)	N1-Er1/Eu1-O2	69.10(14)	N2-Er1/Eu1-O6	133.42(14)
O2-Er1/Eu1-O5	75.08(13)	N1-Er1/Eu1-O3	144.42(14)	N1-Er1/Eu1-N2	145.05(15)
O2-Er1/Eu1-O6	124.31(13)	N1-Er1/Eu1-O4	76.69(14)	C1N-Ag1-C2N	175.4(2)
O3-Er1/Eu1-O4	77.74(13)	N1-Er1/Eu1-O5	101.29(15)		

Table S6 Selected detailed structure parameters for **Yb@EuAg**.

Selected bond lengths in **Yb@EuAg** / Å					
Yb1/Eu1-O1	2.323(6)	Yb1/Eu1-O4	2.372(6)	Yb1/Eu1-N1	2.526(7)
Yb1/Eu1-O2	2.442(7)	Yb1/Eu1-O5	2.366(6)	Yb1/Eu1-N2	2.591(7)
Yb1/Eu1-O3	2.369(6)	Yb1/Eu1-O6	2.331(6)	Ag1-C1N	2.039(8)
				Ag1-C2N	2.047(8)
Selected bond angles in **Yb@EuAg** / °					
O1-Yb1/Eu1-O2	73.3(2)	O3-Yb1/Eu1-O5	101.6(2)	N1-Yb1/Eu1-O6	77.0(2)
O1-Yb1/Eu1-O3	138.3(2)	O3-Yb1/Eu1-O6	73.0(2)	N2-Yb1/Eu1-O1	72.9(2)
O1-Yb1/Eu1-O4	75.8(2)	O4-Yb1/Eu1-O5	146.5(2)	N2-Yb1/Eu1-O2	133.4(2)
O1-Yb1/Eu1-O5	87.9(2)	O4-Yb1/Eu1-O6	130.2(2)	N2-Yb1/Eu1-O3	72.0(2)
O1-Yb1/Eu1-O6	148.1(2)	O5-Yb1/Eu1-O6	77.07(19)	N2-Yb1/Eu1-O4	76.0(2)
O2-Yb1/Eu1-O3	148.4(2)	N1-Yb1/Eu1-O1	101.8(2)	N2-Yb1/Eu1-O5	71.3(2)
O2-Yb1/Eu1-O4	124.32(19)	N1-Yb1/Eu1-O2	74.1(2)	N2-Yb1/Eu1-O6	126.1(2)
O2-Yb1/Eu1-O5	76.3(2)	N1-Yb1/Eu1-O3	93.6(2)	N1-Yb1/Eu1-N2	144.2(3)
O2-Yb1/Eu1-O6	75.9(2)	N1-Yb1/Eu1-O4	68.6(2)	C1N-Ag1-C2N	174.8(4)
O3-Yb1/Eu1-O4	74.4(2)	N1-Yb1/Eu1-O5	144.4(2)		

Table S7 Results of Continuous Shape Measure (CShM) analyses for eight−coordinated Ln(III) centers in **EuAg**, **ErAg**, **YbAg**, **Er@EuAg**, and **Yb@EuAg**.

Compound	CShM parameter for Ln(III) centers (C.N. = 8)*						Geometry
	CU-8	SAPR-8	TDD-8	BTPR-8	JSD-8	TT-8	
EuAg	8.387	1.713	**0.430**	2.219	3.119	9.190	**TDD-8**
ErAg	8.318	1.1895	**0.399**	2.314	3.002	9.057	**TDD-8**
YbAg	8.410	1.836	**0.469**	2.306	2.989	9.100	**TDD-8**
Er@EuAg	8.387	1.945	**0.425**	2.323	2.921	9.065	**TDD-8**
Yb@EuAg	8.369	1.784	**0.431**	2.278	3.076	9.132	**TDD-8**

Table S8 Results of Continuous Shape Measure (CShM) analysis for two-coordinated Ag(I) centers in **EuAg**, **ErAg**, **YbAg**, **Er@EuAg**, and **Yb@EuAg** complexes.

Compound	CShM parameter for for Ag(I) centers (C.N. = 2)*			Geometry
	L-2	vT-2	vOC-2	
EuAg	**0.055**	12.685	22.999	**L-2**
ErAg	**0.071**	12.471	22.727	**L-2**
YbAg	**0.053**	12.714	23.035	**L-2**
Er@EuAg	**0.056**	12.679	22.991	**L-2**
Yb@EuAg	**0.069**	12.497	22.760	**L-2**

*Continuous Shape Measure (CShM) Parameters:[S8,S10]

eight-coordinated complexes

CShM CU-8	–	the parameter related to the cube geometry (O_h)
CShM SAPR-8	–	the parameter related to the square antiprism geometry (D_{4d})
CShM TDD-8	–	the parameter related to the triangular dodecahedron geometry (D_{2d})
CShM BTPR-8	–	the parameter related to the biaugmented trigonal prism geometry (C_{2v})
CShM JSD-8	–	the parameter related to the snub disphenoid geometry (D_{2d})
CShM TT-8	–	the parameter related to the tetrakis tetrahedron geometry (T_d)

two-coordinated complexes

CShM L-2	–	the parameter related to the linear geometry ($D_{\infty h}$)
CShM vT-2	–	the parameter related to the divacant tetrahedron geometry (C_{2v})
CShM vOC-2	–	the parameter related to the tetravacant octahedron geometry (C_{2v})

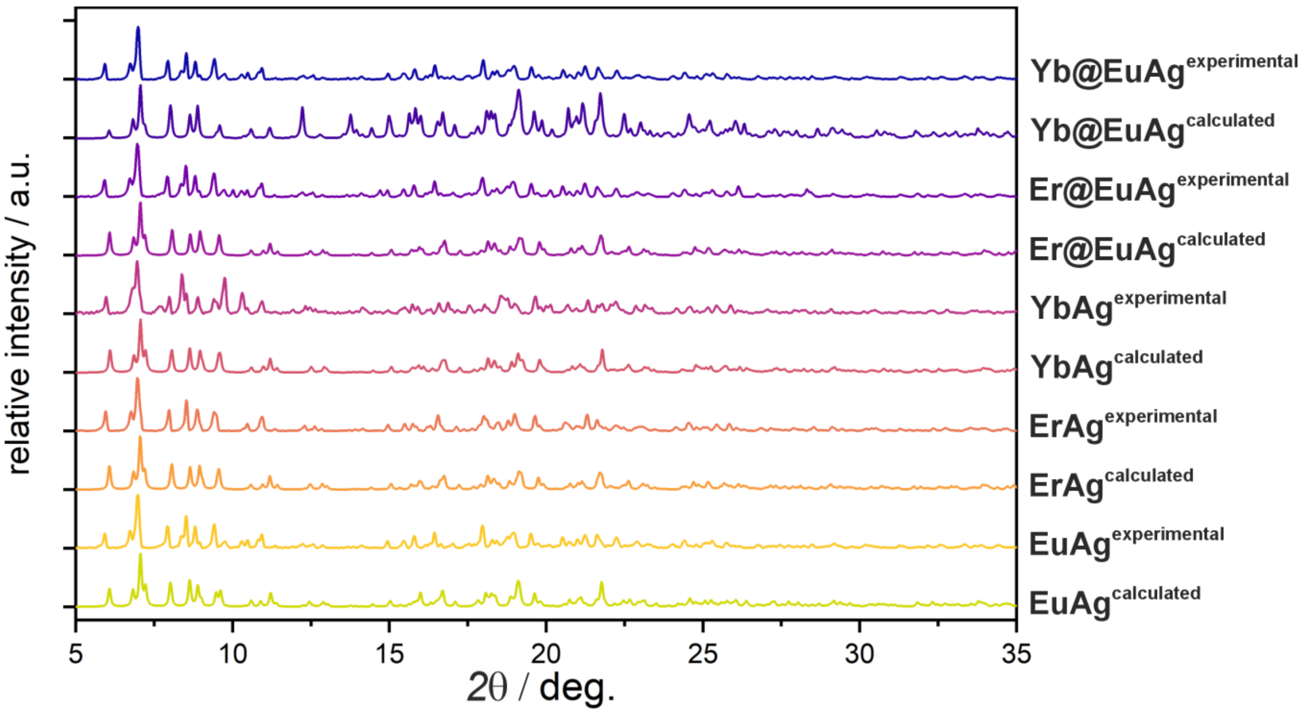

Fig. S8 Comparison of experimental (room temperature) and calculated powder X-ray diffraction (P-XRD) patterns for **EuAg**, **ErAg**, **YbAg**, **Er@EuAg**, and **Yb@EuAg**, presented in the selected 5–35° range of the 2*Θ* angle. The calculated P-XRD patterns were obtained from the structural model determined within the single-crystal X-ray diffraction (SC-XRD) structural analysis (T = 100(2) K).

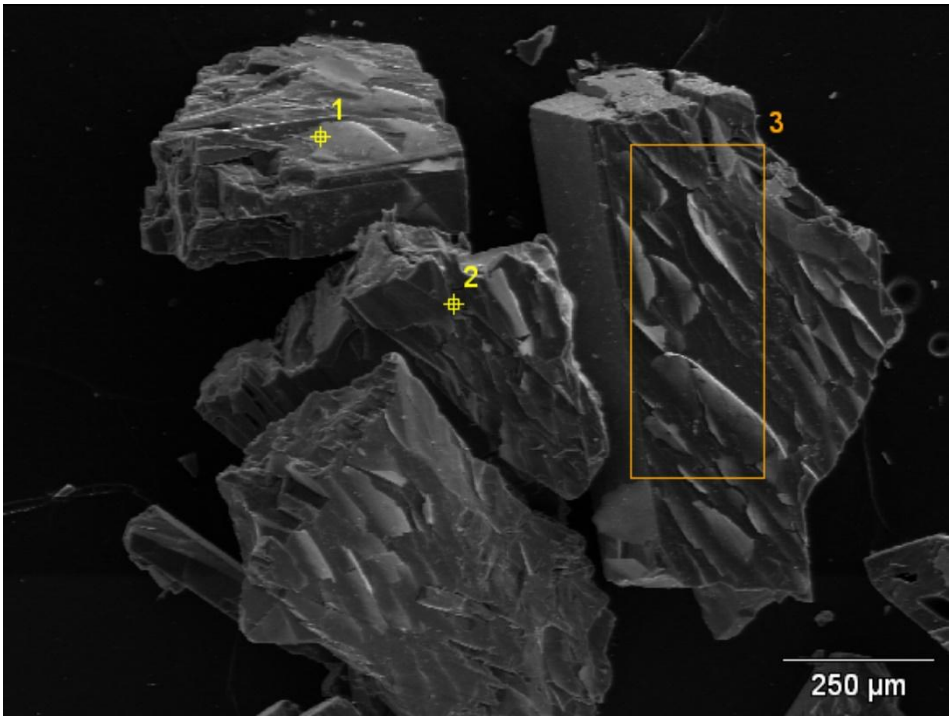

Fig. S9 The SEM image of the polycrystalline ground sample of **Er@EuAg** with the indication of the points 1–2 and the area 3 targeted for the EDX analysis. The related results of the analysis are gathered in Table S9.

Table S9 Results of SEM-EDX analysis of the lanthanides composition in **Er@EuAg** (Fig. S9).

Metal	Er^{III}	Eu^{III}
measured atomic composition (only lanthanides included) / %	0.63(23)	8.75(44)
	0.51(27)	9.11(54)
	0.32(19)	7.33(38)
	0.79(28)	9.24(56)
	0.54(26)	8.87(50)
	0.27(21)	7.05(41)
	0.54(21)	7.65(42)
	0.48(22)	8.00(45)
relative atomic composition (calculated for 1 Ln^{III} center)	0.05(8)	0.95(2)
proposed metal composition	0.05	0.95

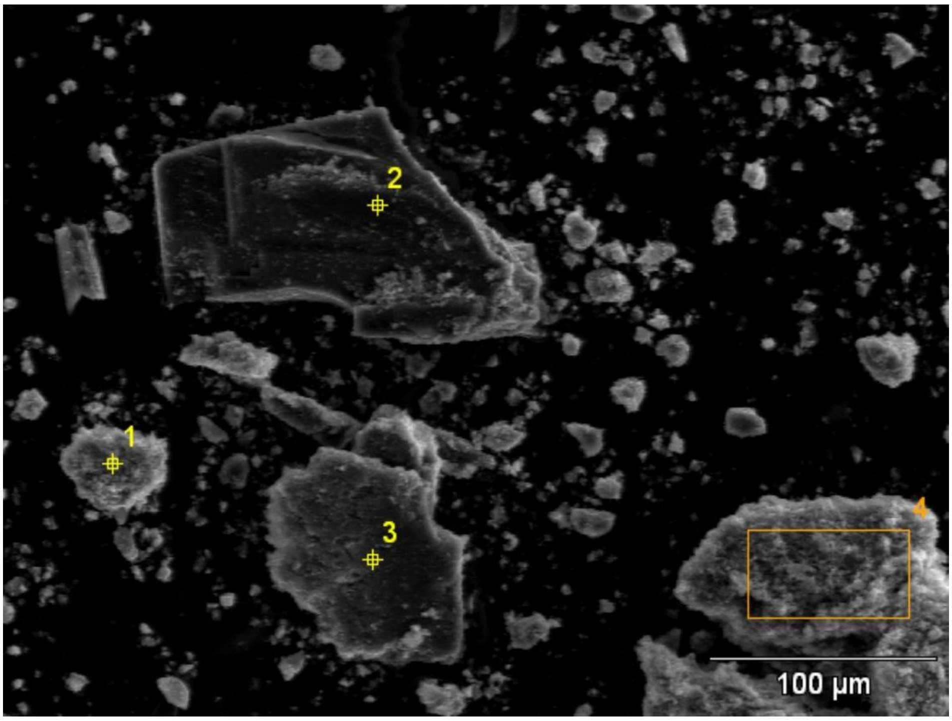

Fig. S10 The SEM image of the polycrystalline ground sample of **Yb@EuAg** with the indication of the points 1–3 and the area 4 targeted for the EDX analysis. The related results of the analysis are gathered in Table S10.

Table S10 Results of SEM-EDX analysis of the lanthanides composition in **Yb@EuAg** (Fig. S10).

Metal	Yb^{III}	Eu^{III}
measured atomic composition (only lanthanides included) / %	1.02(88)	29.75(285)
	0.46(56)	18.50(176)
	2.71(79)	27.12(161)
	2.73(91)	33.91(14)
	1.34(75)	27.21(239)
	1.30(95)	37.57(309)
	0.59(105)	42.23(135)
	1.50(104)	40.72(131)
	1.21(104)	40.85(131)
relative atomic composition (calculated for 1 Ln^{III} center)	0.04(2)	0.96(4)
proposed metal composition	0.04	0.96

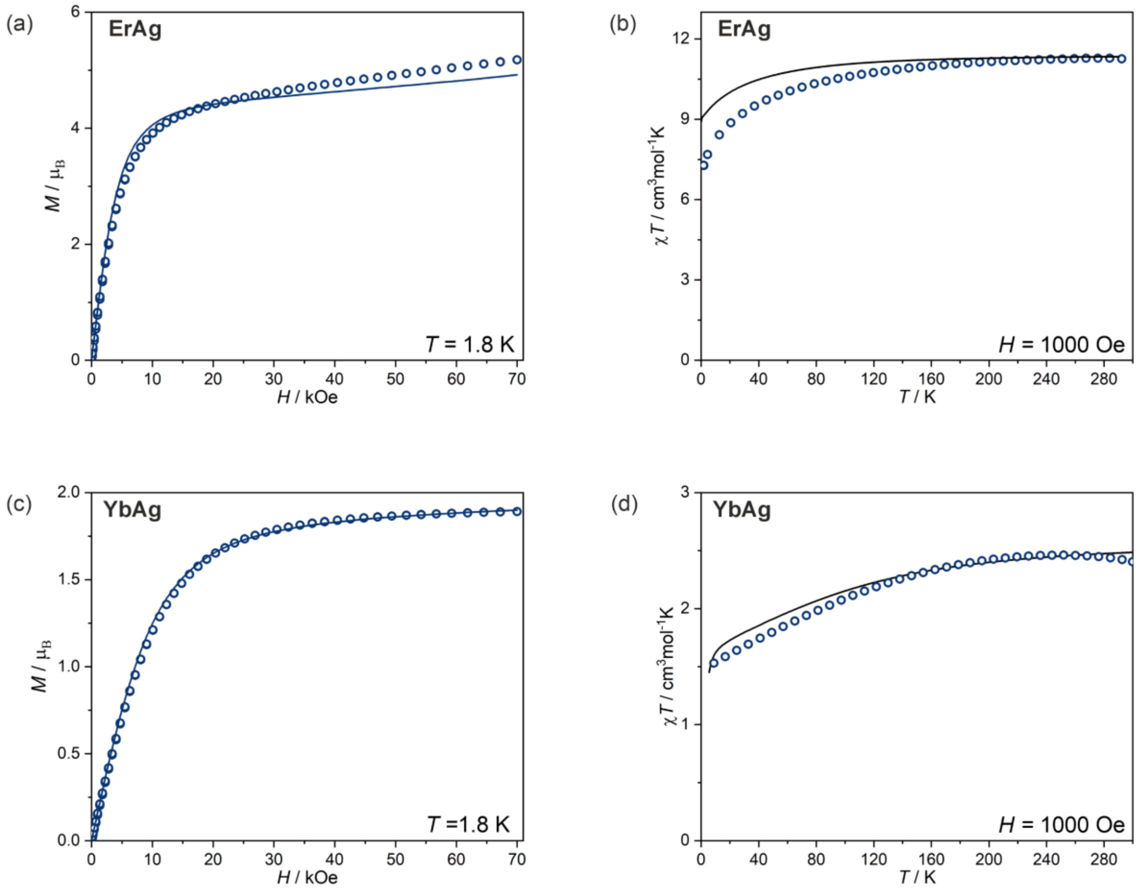

Fig. S11 Direct-current (*dc*) magnetic properties of **ErAg** (a–b) and **YbAg** (c–d): the field dependencies of molar magnetization (*M)* at *T* = 1.8 K (left panel), and temperature dependencies of the $\chi_M T$ product at H_{dc} = 1000 Oe (right panel). The experimental data (empty circles) are compared with the calculated curves based on the results of *ab initio* calculations performed for lanthanide(III) centers in the perfect magnetic isolation (solid lines).

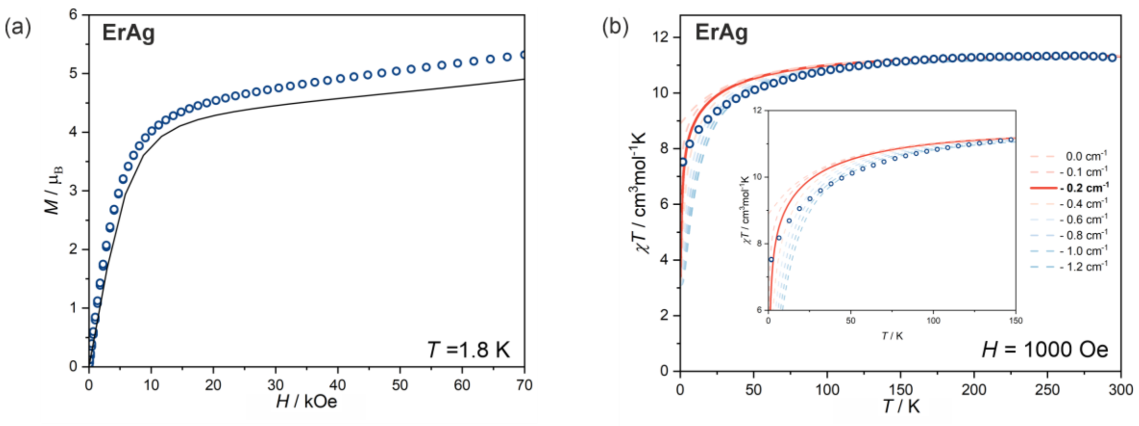

Fig. S12 Direct-current (*dc*) magnetic properties of **ErAg**, together with the comparison of the experimental curves (blue empty points) and the theoretical ones (solid lines), which were obtained by taking into account the *ab initio*-calculated single-ion properties of Er(III) centers and the Er-Er coupling interactions; the field dependences of molar magnetization (*M)* collected at T = 1.8 K, compared with the theoretical model with $J = -0.2$ cm^{-1} (a) and the temperature dependence of the $\chi_M T$ product at H_{dc} = 1000 Oe with the theoretical curves with variable J constant, indicating the best fit for the mentioned $J = -0.2$ cm^{-1} (b).

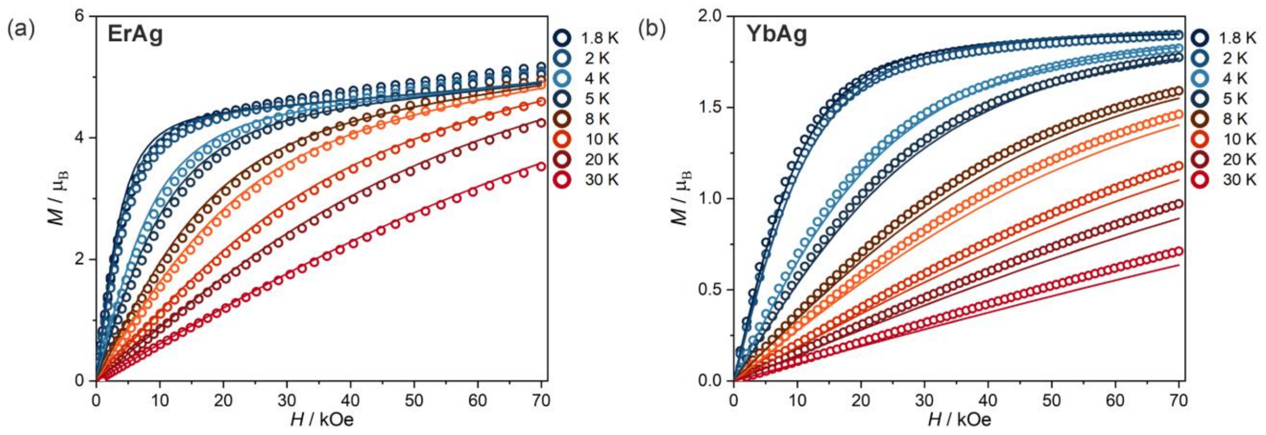

Fig. S13 Magnetization (*M*) versus field curves for **ErAg** (a) and **YbAg** (b) at the indicated temperatures. The experimental data are compared with the curves simulated based on the results of *ab initio* calculations. In (a), the presence of $J = -0.2$ cm^{-1} coupling constant is included (see Fig. S12 for comparison).

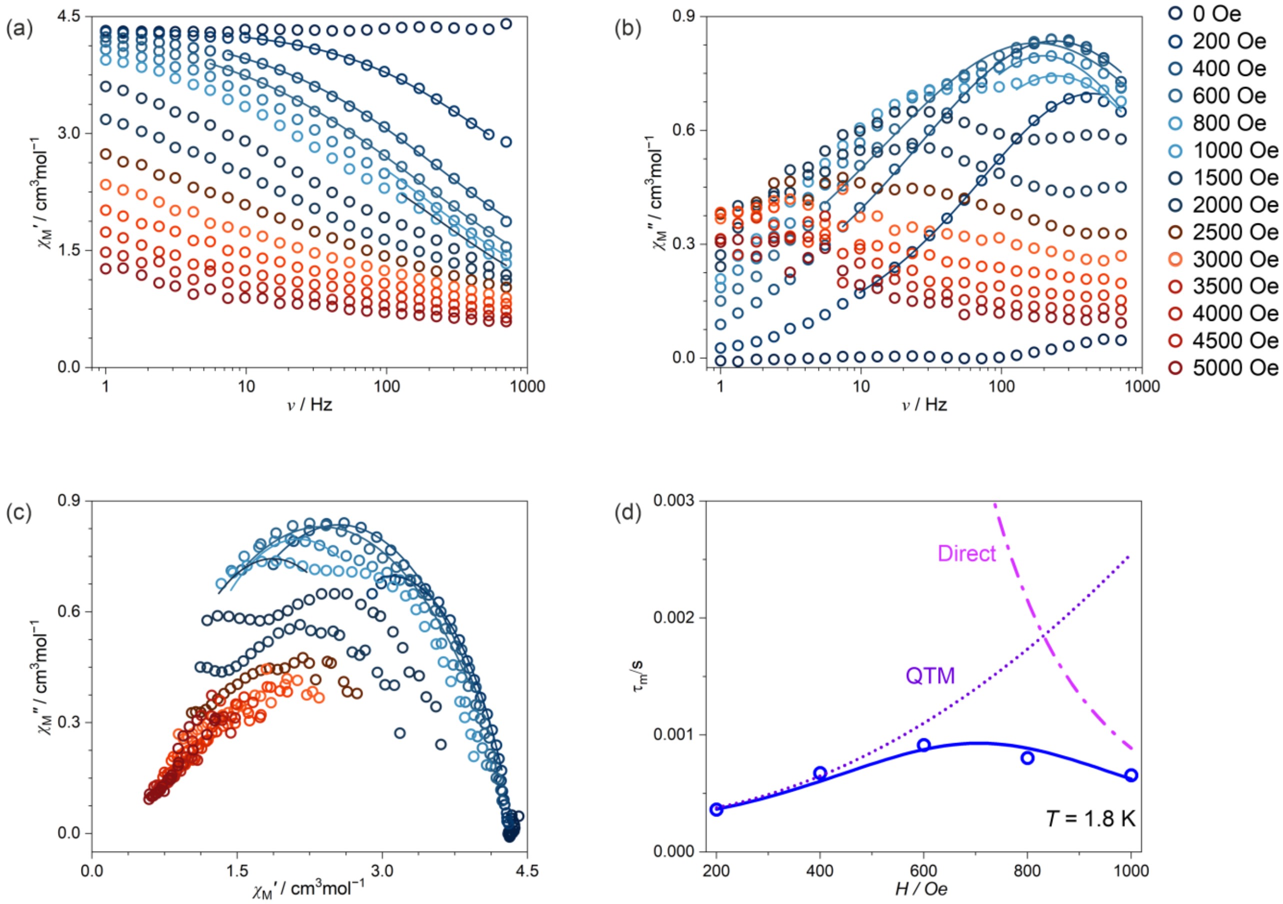

Fig. S14 Magnetic-field-variable alternate-current (*ac*) magnetic characteristics for **ErAg** at T = 1.8 K, including the frequency dependences of the in-phase susceptibility, χ_M', (a) and the out-of-phase susceptibility, χ_M'', (b) under variable indicated *dc* fields, the related Argand plots (c), and the field dependence of the resulting relaxation time, τ_m (d). Colored solid lines in (a–c) represent the best fits using the generalized Debye model for a single relaxation process. The blue solid line in (d) shows the best fit taking into account the indicated relaxation processes, while the dashed colored lines represent the respective course of individual magnetic relaxation processes. The results in (d) were obtained within a simultaneous fit of both temperature- and field-variable data (this figure and Fig. S15). Best-fit parameters for the (d) part are gathered in Tables 1 and S11.

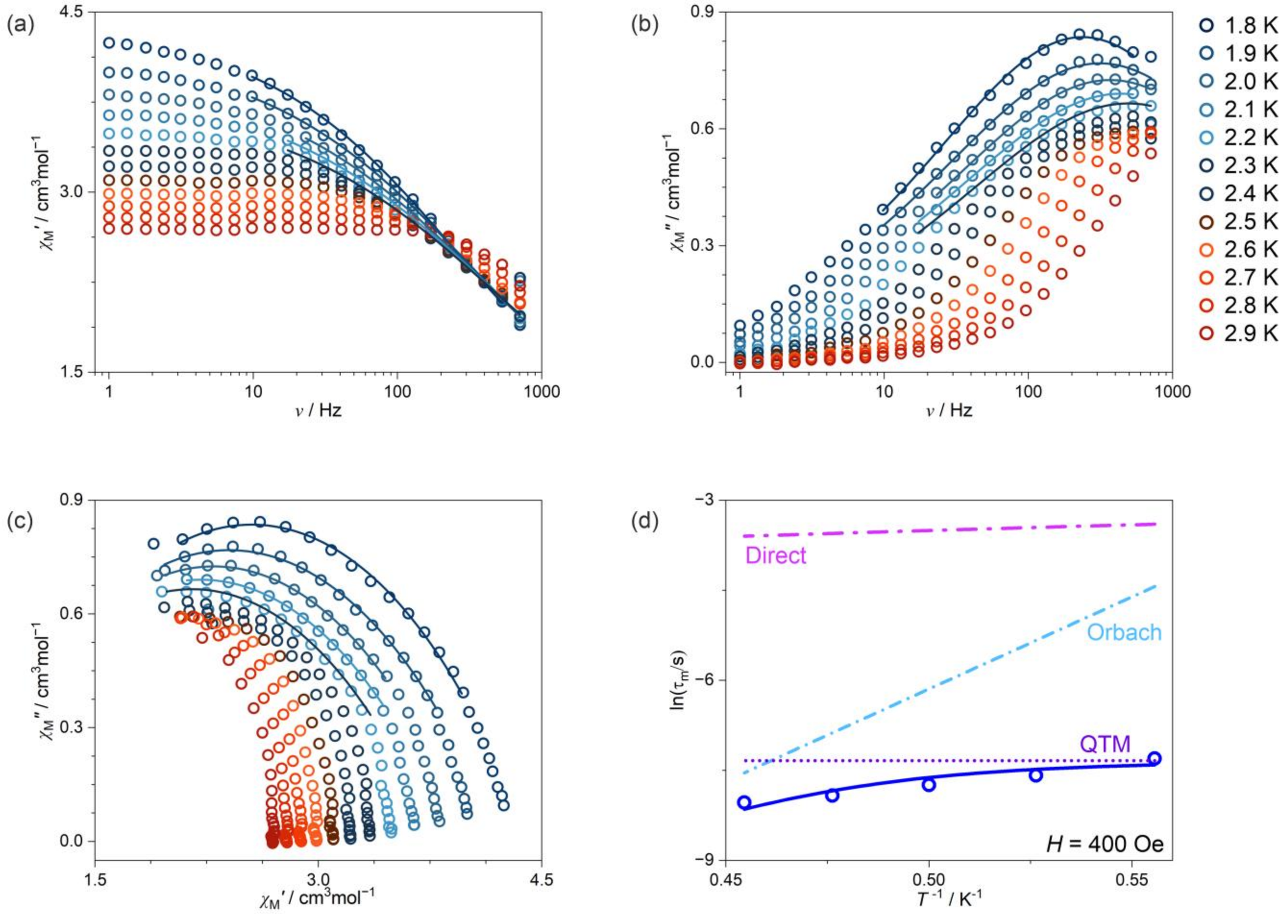

Fig. S15 Temperature-variable alternate-current (*ac*) magnetic characteristics for **ErAg** at H_{dc} = 400 Oe, including the frequency dependences of the in-phase susceptibility, χ_M', (a) and the out-of-phase susceptibility, χ_M'', (b) under variable indicated *dc* fields, the related Argand plots (c), and the temperature dependence of the resulting relaxation time, τ_m (d). Colored solid lines in (a–c) represent the best fits using the generalized Debye model for a single relaxation process. The blue solid line in (d) shows the best fit taking into account the indicated relaxation processes, while the dashed colored lines represent the respective course of individual magnetic relaxation processes. The results in (d) were obtained within a simultaneous fit of both temperature- and field-variable data (this figure and Fig. S14). Best-fit parameters for the (d) part are gathered in Tables 1 and S11.

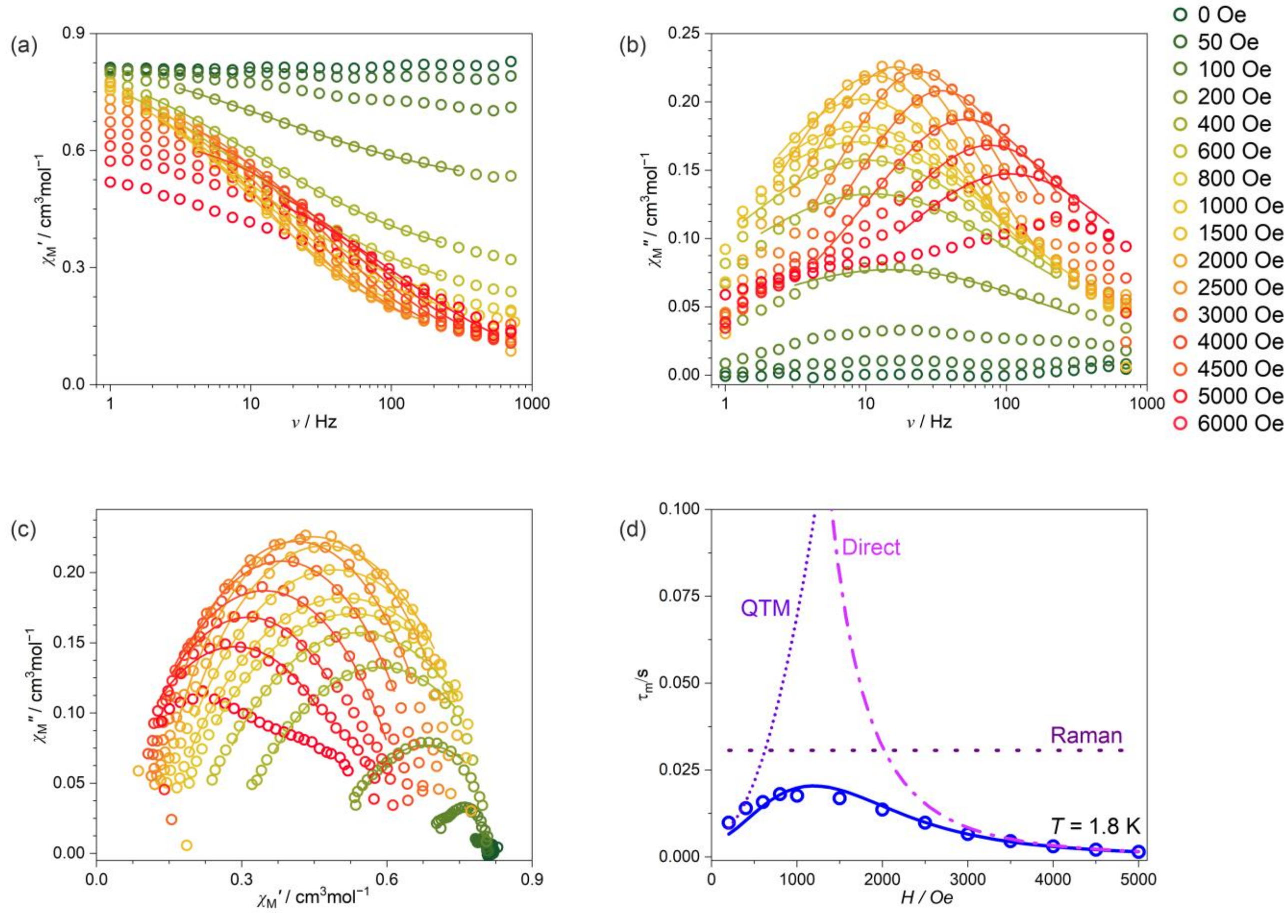

Fig. S16 Magnetic-field-variable alternate-current (*ac*) magnetic characteristics for **YbAg** at T = 1.8 K, including the frequency dependences of the in-phase susceptibility, χ_M', (a) and the out-of-phase susceptibility, χ_M'', (b) under variable indicated *dc* fields, the related Argand plots (c), and the field dependence of the resulting relaxation time, τ_m (d). Colored solid lines in (a–c) represent the best fits using the generalized Debye model for a single relaxation process. The blue solid line in (d) shows the best fit taking into account the indicated relaxation processes, while the dashed colored lines represent the respective course of individual magnetic relaxation processes. The results in (d) were obtained within a simultaneous fit of both temperature- and field-variable data (this figure and Fig. S17). Best-fit parameters for the (d) part are gathered in Tables 1 and S11.

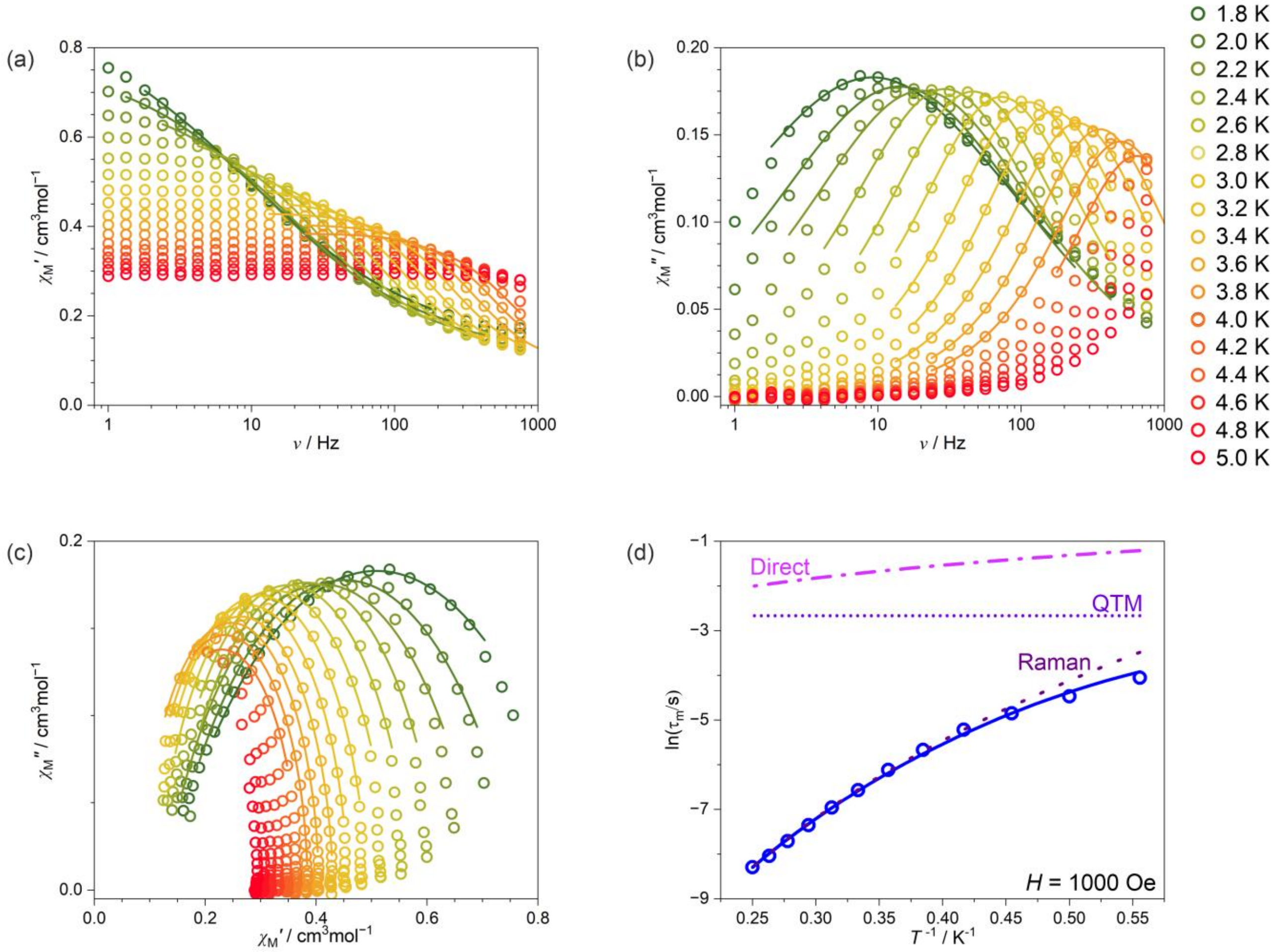

Fig. S17 Temperature-variable alternate-current (*ac*) magnetic characteristics for **YbAg** at H_{dc} = 1 kOe, including the frequency dependences of the in-phase susceptibility, χ_M', (a) and the out-of-phase susceptibility, χ_M'', (b) under variable indicated *dc* fields, the related Argand plots (c), and the temperature dependence of the resulting relaxation time, τ_m (d). Colored solid lines in (a–c) represent the best fits using the generalized Debye model for a single relaxation process. The blue solid line in (d) shows the best fit taking into account the indicated relaxation processes, while the dashed colored lines represent the respective course of individual magnetic relaxation processes. The results in (d) were obtained within a simultaneous fit of both temperature- and field-variable data (this figure and Fig. S16). Best-fit parameters for the (d) part are gathered in Tables 1 and S11.

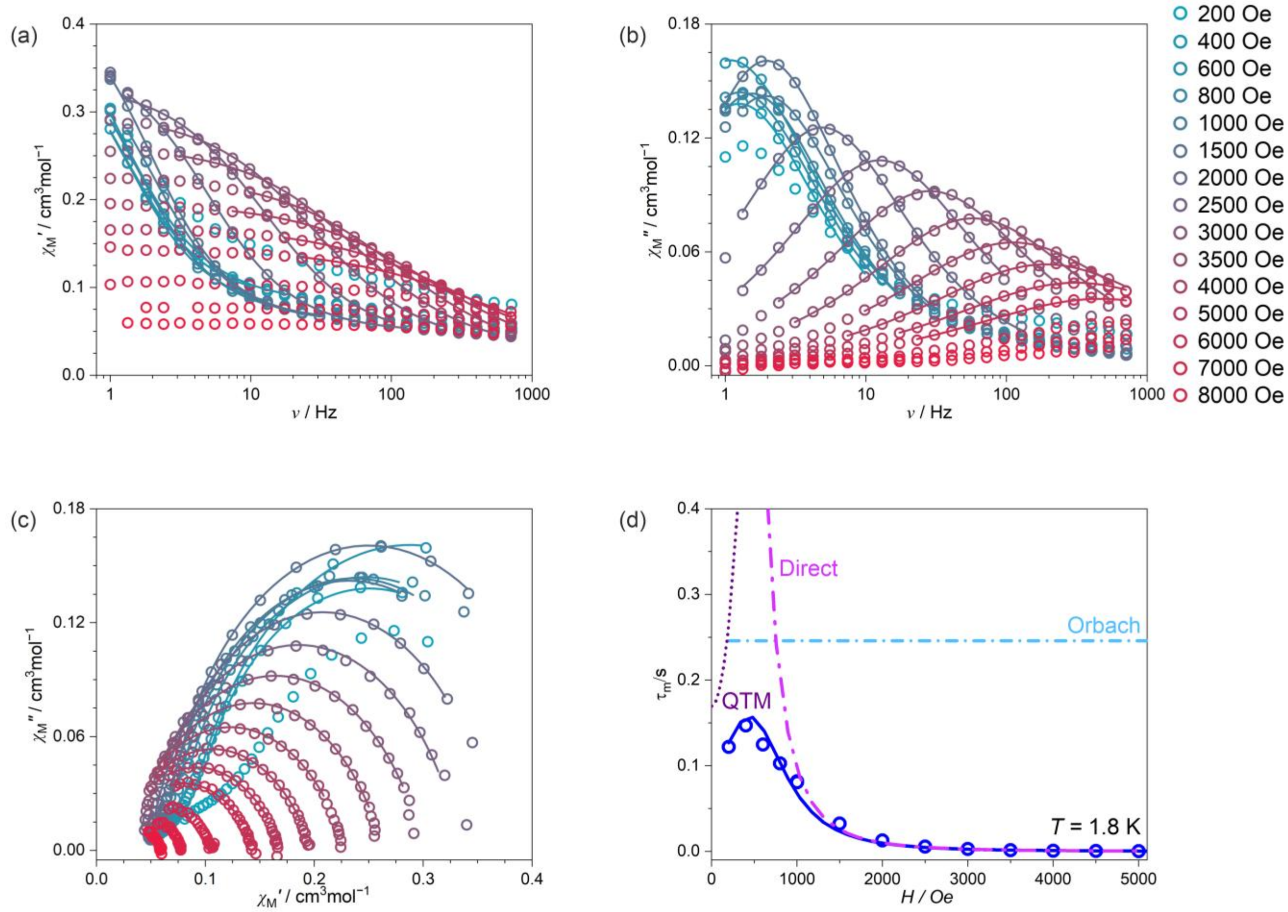

Fig. S18 Magnetic-field-variable alternate-current (*ac*) magnetic characteristics for **Er@EuAg** at T = 1.8 K, including the frequency dependences of the in-phase susceptibility, χ_M', (a) and the out-of-phase susceptibility, χ_M'', (b) under variable indicated *dc* fields, the related Argand plots (c), and the field dependence of the resulting relaxation time, τ_m (d). Colored solid lines in (a–c) represent the best fits using the generalized Debye model for a single relaxation process. The blue solid line in (d) shows the best fit taking into account the indicated relaxation processes, while the dashed colored lines represent the respective course of individual magnetic relaxation processes. The results in (d) were obtained within a simultaneous fit of both temperature- and field-variable data (this figure and Fig. S19). Best-fit parameters for the (d) part are gathered in Tables 1 and S11.

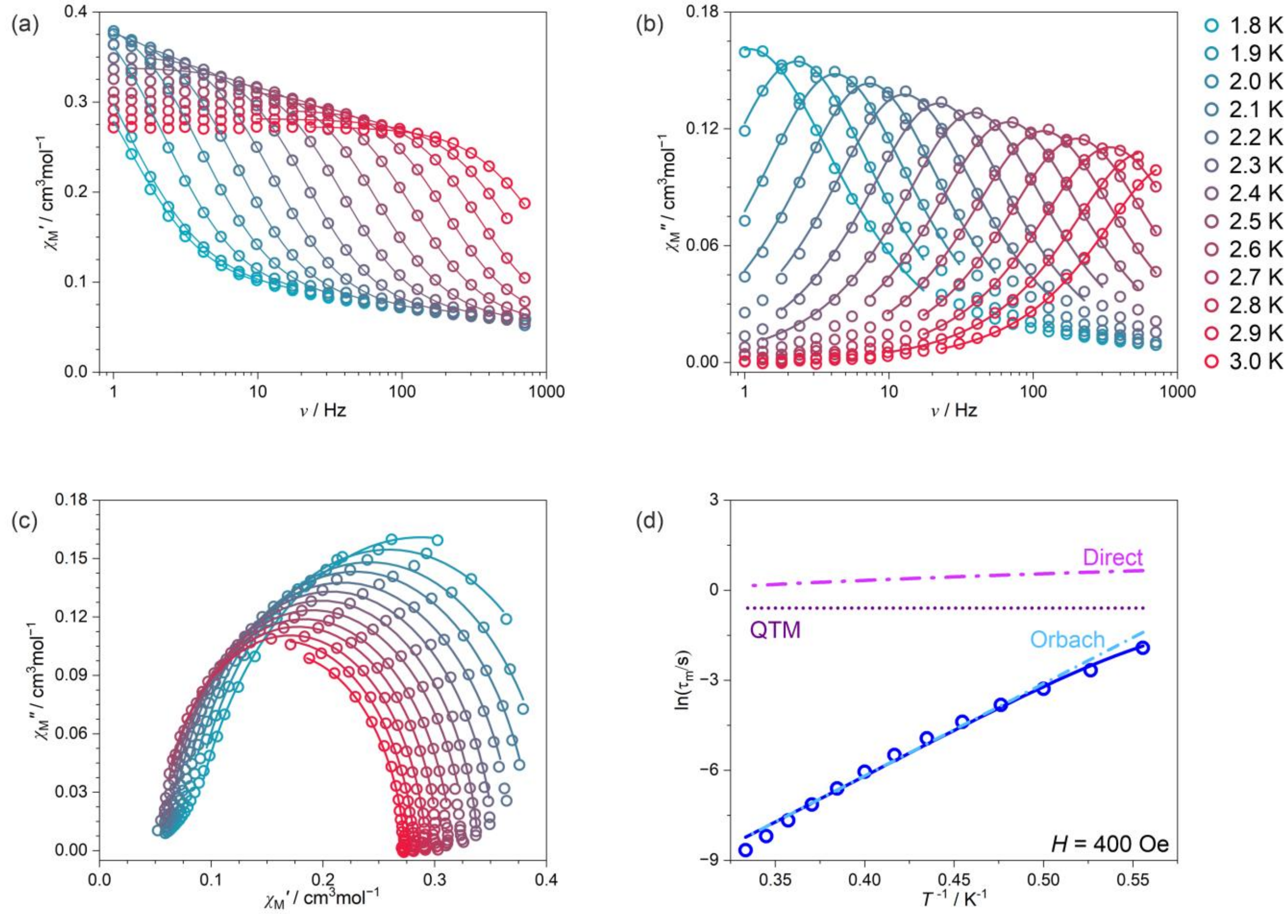

Fig. S19 Temperature-variable alternate-current (*ac*) magnetic characteristics for **Er@EuAg** at H_{dc} = 400 Oe, including the frequency dependences of the in-phase susceptibility, χ_M', (a) and the out-of-phase susceptibility, χ_M'', (b) under variable indicated *dc* fields, the related Argand plots (c), and the temperature dependence of the resulting relaxation time, τ_m (d). Colored solid lines in (a–c) represent the best fits using the generalized Debye model for a single relaxation process. The blue solid line in (d) shows the best fit taking into account the indicated relaxation processes, while the dashed colored lines represent the respective course of individual magnetic relaxation processes. The results in (d) were obtained within a simultaneous fit of both temperature- and field-variable data (this figure and Fig. S18). Best-fit parameters for the (d) part are gathered in Tables 1 and S11.

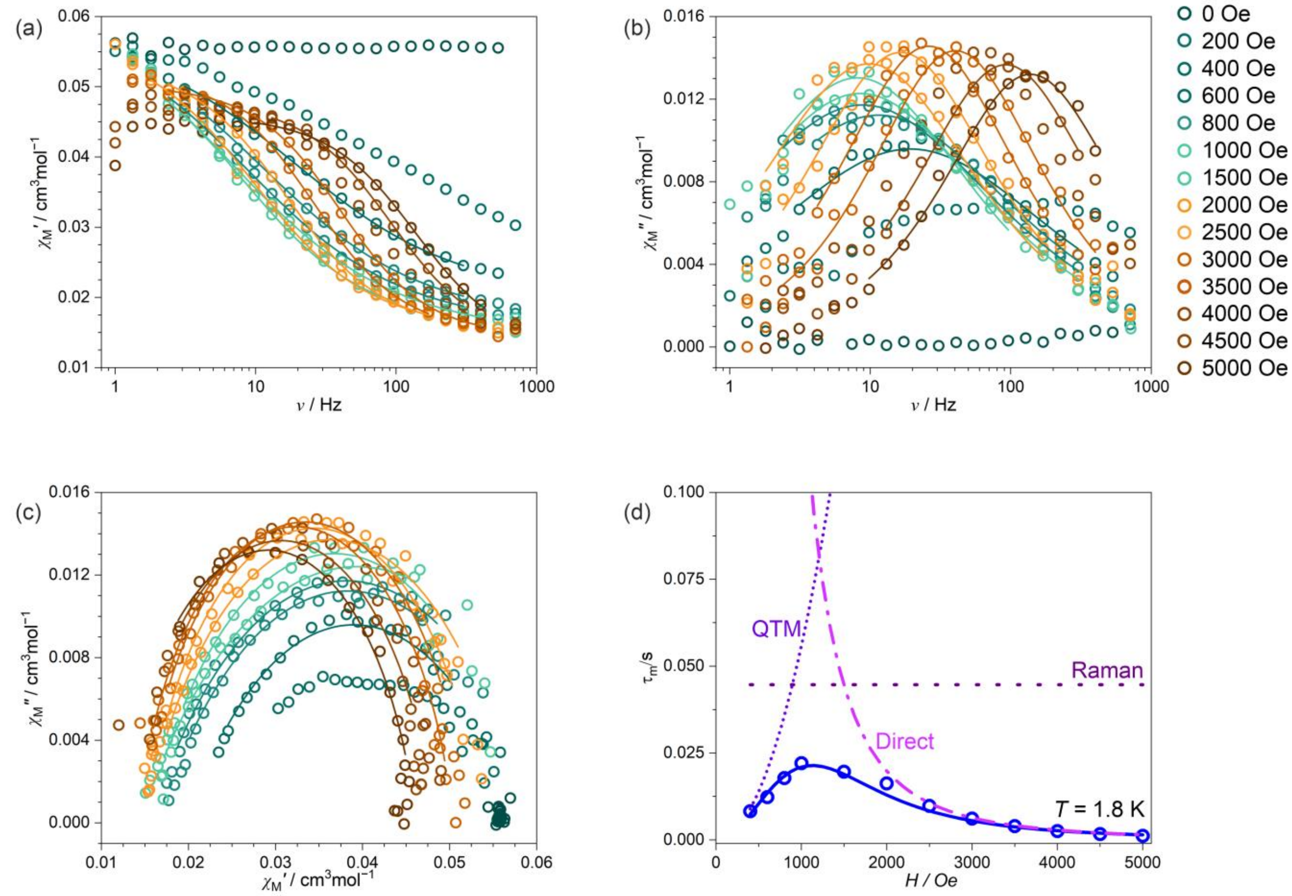

Fig. S20 Magnetic-field-variable alternate-current (*ac*) magnetic characteristics for **Yb@EuAg** at T = 1.8 K, including the frequency dependences of the in-phase susceptibility, χ_M', (a) and the out-of-phase susceptibility, χ_M'', (b) under variable indicated *dc* fields, the related Argand plots (c), and the field dependence of the resulting relaxation time, τ_m (d). Colored solid lines in (a–c) represent the best fits using the generalized Debye model for a single relaxation process. The blue solid line in (d) shows the best fit taking into account the indicated relaxation processes, while the dashed colored lines represent the respective course of individual magnetic relaxation processes. The results in (d) were obtained within a simultaneous fit of both temperature- and field-variable data (this figure and Fig. S21). Best-fit parameters for the (d) part are gathered in Tables 1 and S11.

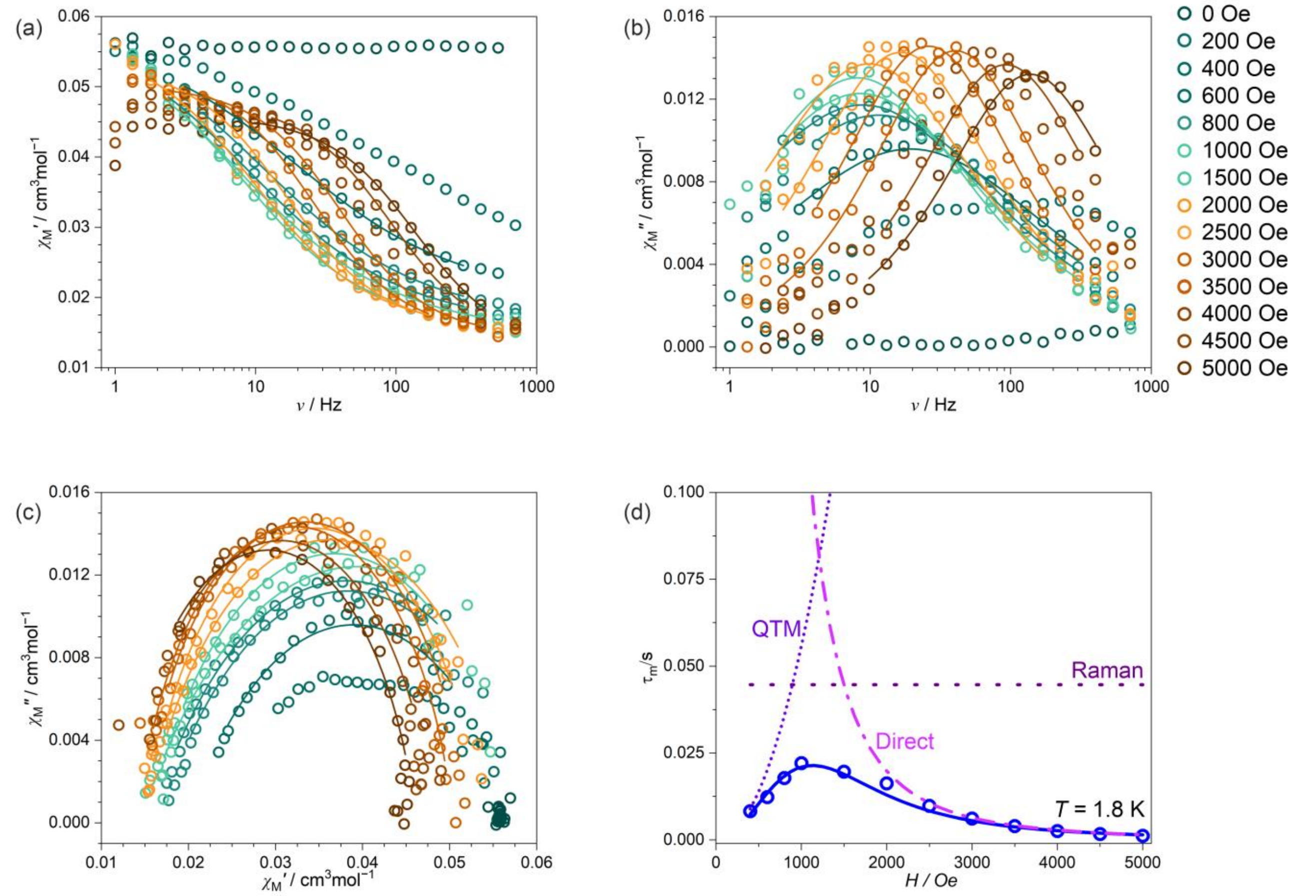

Fig. S21 Temperature-variable alternate-current (*ac*) magnetic characteristics for **Yb@EuAg** at H_{dc} = 1 kOe, including the frequency dependences of the in-phase susceptibility, χ_M', (a) and the out-of-phase susceptibility, χ_M'', (b) under variable indicated *dc* fields, the related Argand plots (c), and the temperature dependence of the resulting relaxation time, τ_m (d). Colored solid lines in (a–c) represent the best fits using the generalized Debye model for a single relaxation process. The blue solid line in (d) shows the best fit taking into account the indicated relaxation processes, while the dashed colored lines represent the respective course of individual magnetic relaxation processes. The results in (d) were obtained within a simultaneous fit of both temperature- and field-variable data (this figure and Fig. S20). Best-fit parameters for the (d) part are gathered in Tables 1 and S11.

Table S11 The summary of the best-fit parameters of slow magnetic relaxation processes for **ErAg**, **YbAg**, **Er@EuAg**, and **Yb@EuAg**, obtained within the three-dimensional simultaneous fitting procedure of the field dependencies at T = 1.8 K and the temperature dependencies at the optimal *dc* fields (Fig. S14–S21).[S9] For the related equations and detailed discussion, see the main text.

Compound	**ErAg**	**YbAg**	**Er@EuAg**	**Yb@EuAg**
A / s^{-1} K^{-1} Oe^{-m}	$8.3(6)\cdot10^{-10}$	$3.6(2)\cdot10^{-10}$	$8.9(3)\cdot10^{-10}$	$1.7(2)\cdot10^{-9}$
m	3.96(3)	3.24(1)	3.27(5)	2.79(1)
a / s^{-1}	3468(731)	171(52)	5.89(3)	$4.43(2)\cdot10^{9}$
b / Oe^{-2}	$7.8(8)\cdot10^{-6}$	$1.1(6)\cdot10^{-5}$	$1.4(9)\cdot10^{-5}$	247(31)
B / s^{-1} K^{-n}	0 (fixed)	0.94(24)	0 (fixed)	0.42(12)
n	0 (fixed)	6.02(23)	0 (fixed)	6.78(27)
τ_0 / s	$2.18(3)\cdot10^{-9}$	0 (fixed)	$1.05(6)\cdot10^{-8}$	0 (fixed)
ΔE / cm^{-1}	30.716 (*ab initio*)	0 (fixed)	30.716 (*ab initio*)	0 (fixed)

Comment on Fig. S22–S27 and Tables S12–S21 – the details of the *ab initio* calculations

The *ab initio* calculations for **EuAg**, **ErAg**, and **YbAg** were performed using an open-source quantum chemistry code: OpenMolcas (v23.06) for the experimental geometry obtained through the SC-XRD measurements, without the additional geometry optimization.[S11] The molecular fragment that was used in the computational procedure contained a lanthanide(III) center with its first coordination sphere and both $[Ag^{I}(CN)_2]^-$ metalloligands. In the first part, we conducted the SA-CASCF (State Average Complete Active Space Self-Consistent Field) type calculations, including scalar relativistic effects within a two-component second-order Douglas-Kroll-Hess (DKH2) Hamiltonian and relativistic Atomic Natural Orbital basis sets of the ANO-RCC type.[S12–S14] To save the disk space, the Cholesky decomposition of electron repulsion integrals was employed with a 10^{-8} threshold. For all considered systems, our models adopted the VTZP basis function for the lanthanide(III) center, VDZP for atoms in its first coordination sphere, and VDZ for the other atoms. In a CASSCF step, the active space was composed of seven 4f orbitals of each lanthanide ion and six, eleven, or thirteen active electrons for **EuAg**, **ErAg,** and **YbAg,** respectively. From the different possible distributions of the active electrons arise 7 septets, 140 quintets, 588 triplets, 490 singlet states for **EuAg**; 35 quartets and 112 doublet states for **ErAg**; and seven doublet states for **YbAg**. In the next step, all the previously optimized spin-free states were mixed within the Restricted Active Space State Interaction (RASSI) submodule by Spin-Orbit Coupling (SOC) within the atomic mean-field (AMFI) approximation.[S15,S16] As a result, we obtained spin, angular, and dipole momenta matrices between SOC states, which, with the SOC-coupling matrix itself, were used in the further simulation of magnetic and spectroscopic properties.

Magnetic properties

Simulations of magnetic properties, including $M(H)$ and $\chi_M T(T)$ dependencies, pseudo-*g*-tensors components, and Zeeman splitting for **YbAg** and **ErAg** (see Tables S12–S15), were performed with the SlothPy software.[S17] Additionally, after obtaining local magnetic properties of **ErAg**, we investigated the interaction between Er(III) magnetic centers within the coordination chain by employing the POLY_ANISO module of the OpenMolcas software. In the adopted methodology, the magnetic exchange coupling is examined using the *ab initio* calculated single-ion properties of anisotropic magnetic centers. The exchange interaction is incorporated within the Lines model using a single, effective isotropic exchange parameter *J* in the Hamiltonian:[S18]

$$H_{exch} = J \cdot \tilde{S}_1 \cdot \tilde{S}_2 \tag{S1}$$

where $\tilde{S}_1$ and $\tilde{S}_2$ are previously found *ab initio* pseudo-spin operators corresponding to the states with definite projections on the *z* quantization axis of the ground Kramers doublet. The magnetic coupling constant *J* is not accessible from the *ab initio* calculations due to the complexity of the system; thus, it was taken into account as the fitting parameter based on the standard deviation between the simulated and the experimental $\chi_M T(T)$ dependencies. Several models containing 2, 3, and 4 magnetic centers in a coordination chain with various parameters *J* were examined. The best fit to the experimental data was found for a model with three Er(III) centers and $J = -0.2$ cm^{-1}.

The investigation of the susceptibility 3-D dependence for **ErAg** revealed anisotropy changes at 5030, 28250, 50840, 90380, and 150000 Oe, which may be considered as magnetic phase transitions.

Luminescence of EuAg

Spectroscopic intensities of **EuAg** were obtained as proportional to the oscillator strength, f_{AB}, calculated from the *ab initio* dipole moments between D_0 and $F_{0–5}$ states for which the transitions occur. For any A to B transition, the oscillator strength may be presented as:

$$f_{AB} = \frac{2}{3}\frac{m_e}{\hbar^2}(E_B - E_A)|\langle A|R|B\rangle|^2 \tag{S2}$$

where E_B and E_A are energies of state B and A, respectively, and $\langle A|R|B\rangle$ is a transition moment between these two states. The calculated energy levels and values of the oscillator strengths between the mentioned states were gathered in Tables S16–S21. The theoretical intensities were used to convolute spectral lines with Gaussian functions (blue line in Fig. S27) with FWHM = 20 cm^{-1}. To improve reproducibility of the experimental data, the simulated emission spectrum as well as absorption energies were shifted to a wavelength corresponding to the $^5D_0 \rightarrow {}^7F_0$ transition, taken as a zero-zero line. For the emission spectrum collected at 10 K, we observe some additional peaks around 630 nm (near the $^5D_0 \rightarrow {}^7F_2$ transition) that are not present at 300 K. The energy of this transition responds to the calculated energy between the $^5D_1$ and $^7F_4$ states. The overlap between the $^5D_0 \rightarrow {}^7F_2$ and $^5D_1 \rightarrow {}^7F_4$ electronic transitions is mentioned in literature, but this observation was not taken into consideration in our model.[S19]

Table S12 Energy levels and pseudo-*g*-tensor components (g_x, g_y, g_z) of 8 ground Kramers doublets of Er(III) centers in **ErAg.**

ErAg				
Energy and pseudo-*g*-tensor components (g_x, g_y, g_z) of 8 ground Kramers doublets				
Doublet no.	Energy / cm^{-1}	Pseudo-*g*-tensor components		
		g_x	g_y	g_z
1	0.000	0.2101	0.3371	17.0313
2	30.716	1.6388	2.8000	13.6895
3	46.777	0.6635	2.1377	14.5638
4	76.184	0.9089	4.0158	8.4258
5	139.356	1.7484	2.9454	11.5247
6	178.543	0.8522	5.3776	9.8109
7	212.803	1.8889	5.7061	8.2185
8	253.263	0.4283	1.4023	14.9661

Table S13 Compositions of 8 ground Kramers doublets of the Er(III) centers in **ErAg**.

Composition of the ground Kramers doublets in the $\vert m_J\rangle$ basis on the quantization axes within the $J = 15/2$ manifold (contributions over 0.1% are shown)							
1st doublet	2nd doublet	3rd doublet	4th doublet	5th doublet	6th doublet	7th doublet	8th doublet
89.4% $\vert\pm15/2\rangle$ 1.3% $\vert\pm13/2\rangle$ 1.5% $\vert\pm11/2\rangle$ 3.7% $\vert\pm9/2\rangle$ 3.0% $\vert\pm7/2\rangle$ 0.3% $\vert\pm5/2\rangle$ 0.5% $\vert\pm3/2\rangle$ 0.4% $\vert\pm1/2\rangle$	2.2% $\vert\pm15/2\rangle$ 4.4% $\vert\pm13/2\rangle$ 2.0% $\vert\pm11/2\rangle$ 3.7% $\vert\pm9/2\rangle$ 13.3% $\vert\pm7/2\rangle$ 29.7% $\vert\pm5/2\rangle$ 23.2% $\vert\pm3/2\rangle$ 21.5% $\vert\pm1/2\rangle$	0.5% $\vert\pm15/2\rangle$ 20.6% $\vert\pm13/2\rangle$ 26.0% $\vert\pm11/2\rangle$ 33.8% $\vert\pm9/2\rangle$ 6.8% $\vert\pm7/2\rangle$ 3.0% $\vert\pm5/2\rangle$ 2.4% $\vert\pm3/2\rangle$ 6.8% $\vert\pm1/2\rangle$	1.4% $\vert\pm15/2\rangle$ 6.1% $\vert\pm13/2\rangle$ 5.3% $\vert\pm11/2\rangle$ 1.0% $\vert\pm9/2\rangle$ 40.7% $\vert\pm7/2\rangle$ 19.1% $\vert\pm5/2\rangle$ 19.7% $\vert\pm3/2\rangle$ 6.8% $\vert\pm1/2\rangle$	2.9% $\vert\pm15/2\rangle$ 28.9% $\vert\pm13/2\rangle$ 20.2% $\vert\pm11/2\rangle$ 31.4% $\vert\pm9/2\rangle$ 5.4% $\vert\pm7/2\rangle$ 1.5% $\vert\pm5/2\rangle$ 3.4% $\vert\pm3/2\rangle$ 6.3% $\vert\pm1/2\rangle$	2.3% $\vert\pm15/2\rangle$ 25.1% $\vert\pm13/2\rangle$ 22.3% $\vert\pm11/2\rangle$ 17.3% $\vert\pm9/2\rangle$ 3.8% $\vert\pm7/2\rangle$ 15.1% $\vert\pm5/2\rangle$ 6.3% $\vert\pm3/2\rangle$ 7.7% $\vert\pm1/2\rangle$	1.0% $\vert\pm15/2\rangle$ 12.6% $\vert\pm13/2\rangle$ 19.4% $\vert\pm11/2\rangle$ 0.8% $\vert\pm9/2\rangle$ 25.5% $\vert\pm7/2\rangle$ 20.7% $\vert\pm5/2\rangle$ 12.5% $\vert\pm3/2\rangle$ 7.6% $\vert\pm1/2\rangle$	0.3% $\vert\pm15/2\rangle$ 1.1% $\vert\pm13/2\rangle$ 3.3% $\vert\pm11/2\rangle$ 8.4% $\vert\pm9/2\rangle$ 1.5% $\vert\pm7/2\rangle$ 10.5% $\vert\pm5/2\rangle$ 32.1% $\vert\pm3/2\rangle$ 42.9% $\vert\pm1/2\rangle$

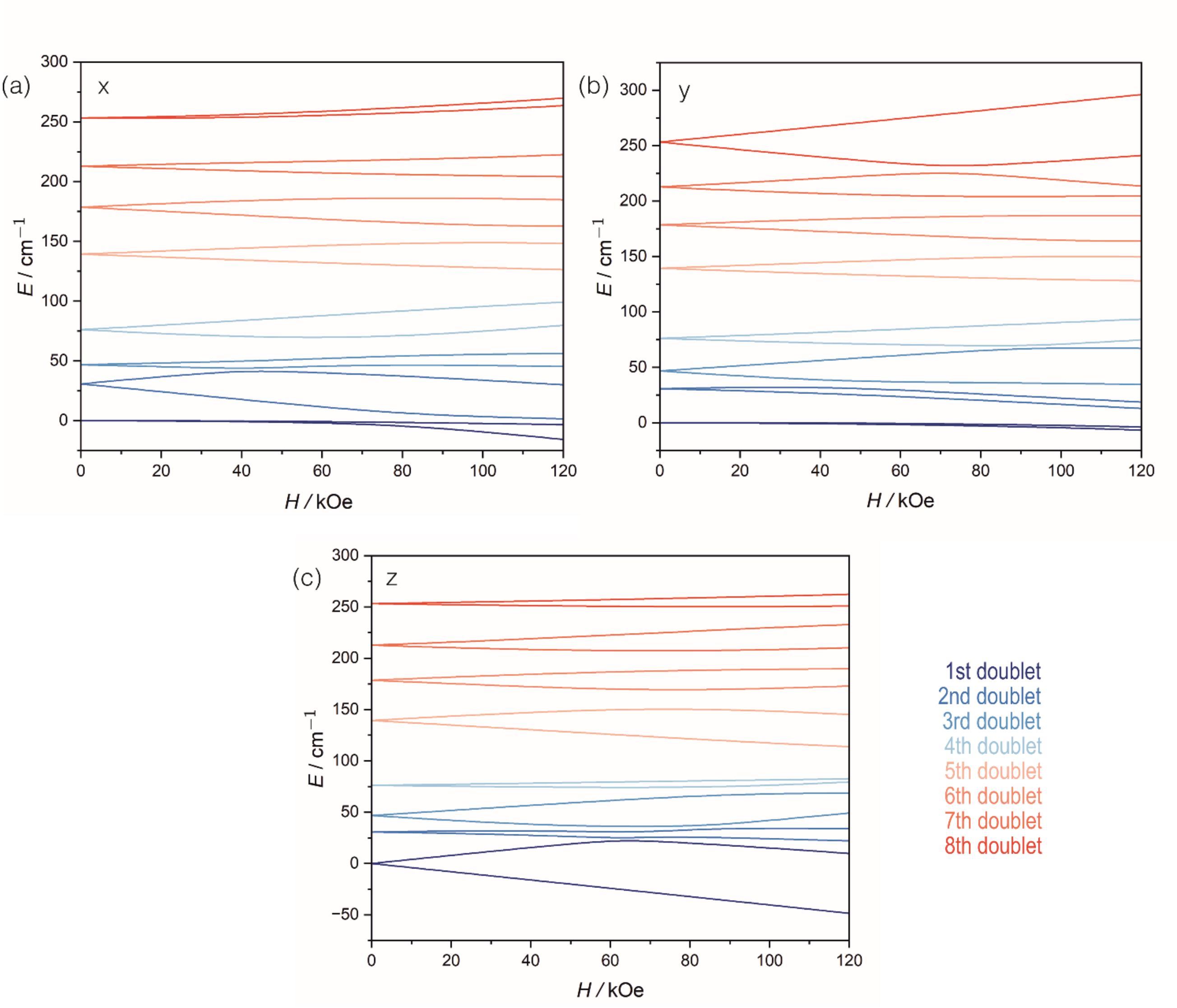

Fig. S22 The Zeeman splitting for the first 8 ground Kramers doublets of Er(III) in **ErAg**, along *x* (a), *y* (b), and *z* (c) magnetic axes.

Table S14 Energy levels and pseudo-*g*-tensor components (g_x, g_y, g_z) of 4 ground Kramers doublets of Yb(III) centers in **YbAg**.

YbAg				
Energy and pseudo-*g*-tensor components (g_x, g_y, g_z) of 4 ground Kramers doublets				
Doublet no.	Energy / cm^{-1}	Pseudo-*g*-tensor components		
		g_x	g_y	g_z
1.	0.000	0.5024	0.9773	7.1318
2.	200.462	0.3871	1.3445	5.6123
3.	305.197	0.7992	3.1239	3.3851
4.	389.968	1.0887	2.1851	6.4502

Table S15 Compositions of the 4 ground Kramers doublets of Yb(III) centers in **YbAg**.

Composition of the ground Kramers doublets in the $|m_J\rangle$ basis on the quantization axes within $J = 7/2$ manifold (contribution over 0.1% shown)			
1st doublet	2nd doublet	3rd doublet	4th doublet
85.5% $|\pm7/2\rangle$ 2.3% $|\pm5/2\rangle$ 7.7% $|\pm3/2\rangle$ 4.6% $|\pm1/2\rangle$	6.7% $|\pm7/2\rangle$ 70.1% $|\pm5/2\rangle$ 11.4% $|\pm3/2\rangle$ 11.8% $|\pm1/2\rangle$	6.3% $|\pm7/2\rangle$ 25.8% $|\pm5/2\rangle$ 48.3% $|\pm3/2\rangle$ 19.6% $|\pm1/2\rangle$	1.6% $|\pm7/2\rangle$ 1.8% $|\pm5/2\rangle$ 32.6% $|\pm3/2\rangle$ 64.1% $|\pm1/2\rangle$

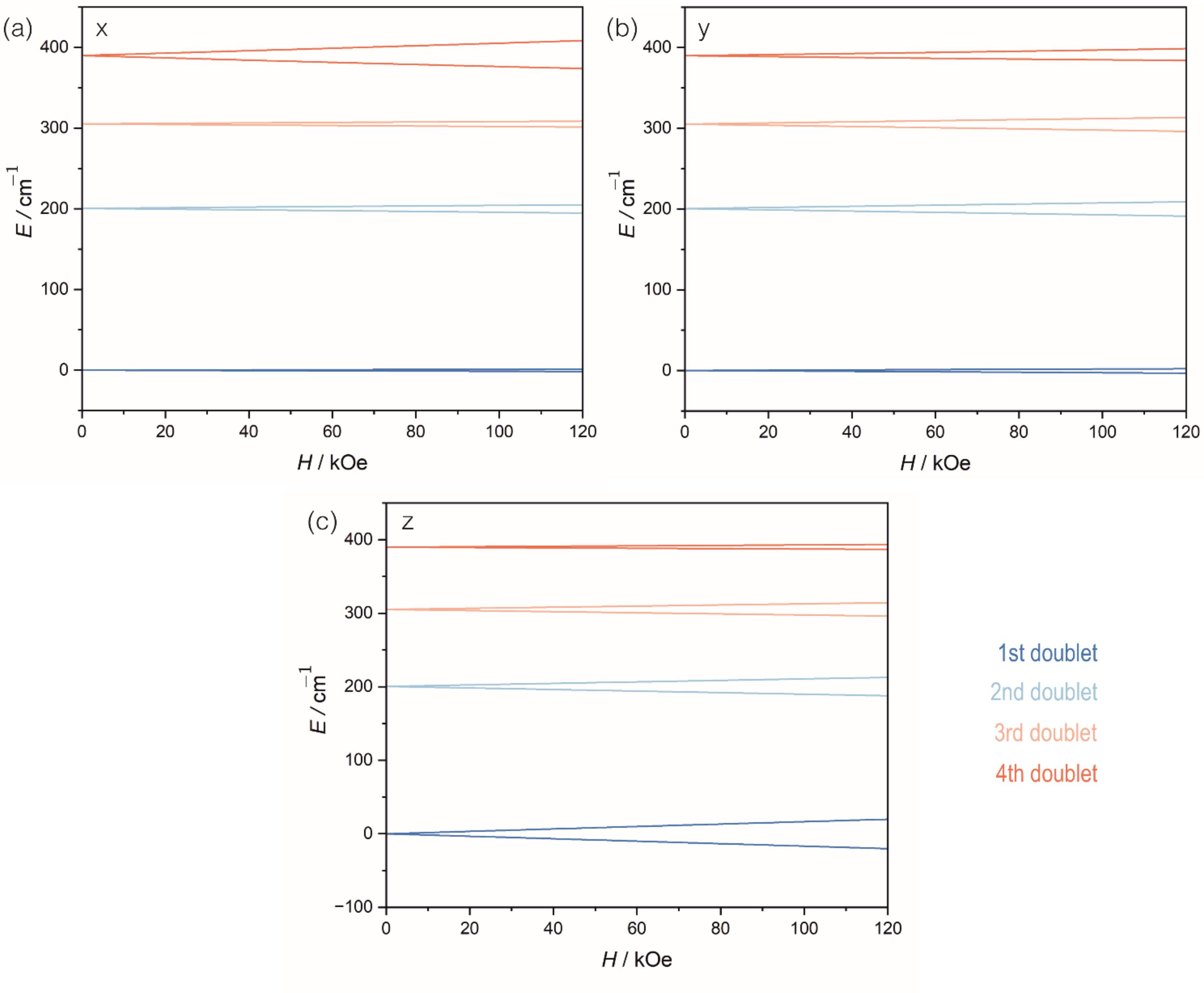

Fig. S23 The Zeeman splitting for the first 4 ground Kramers doublets of Yb(III) in **YbAg**, along *x* (a), *y* (b), and *z* (c) magnetic axes.

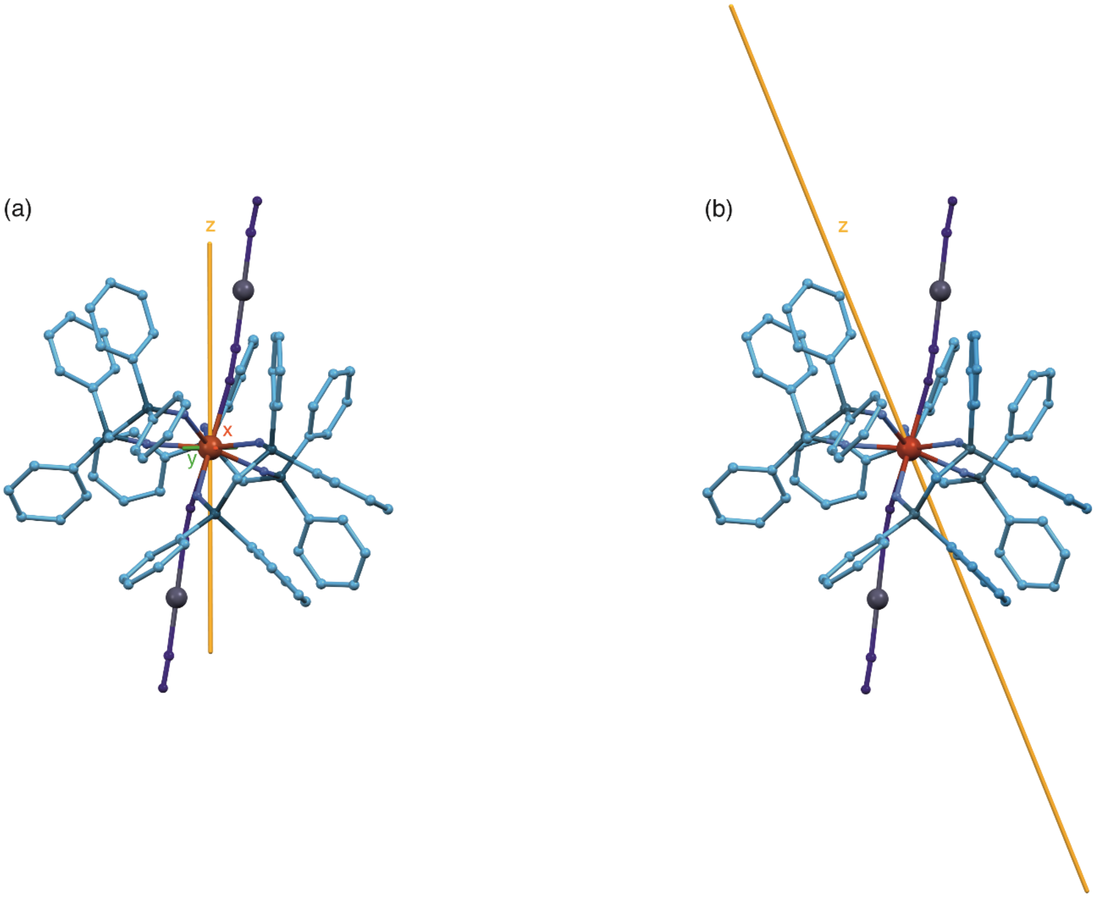

Fig. S24 The alignment of easy magnetic axes in **ErAg** (a) and **YbAg** (b). The visualized lengths of the axes represent the values of g_z components of the respective pseudo-g-tensors.

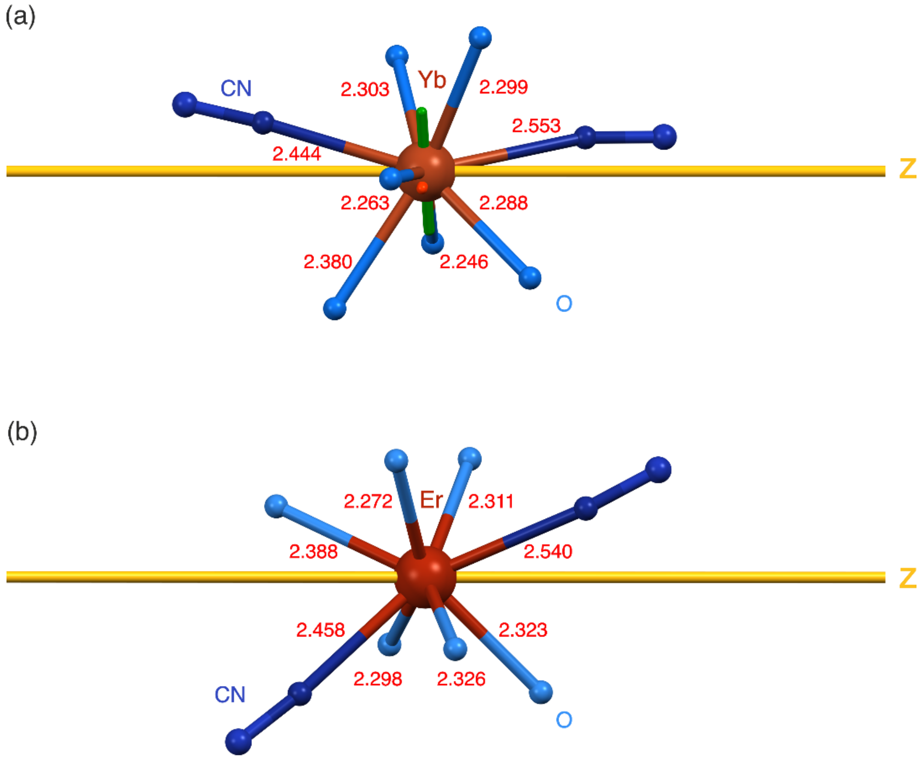

Fig. S25 Selected molecular fragments of **YbAg** (a) and **ErAg** (b) with the indicated interatomic distances in Å and the alignment of computed magnetic axes.

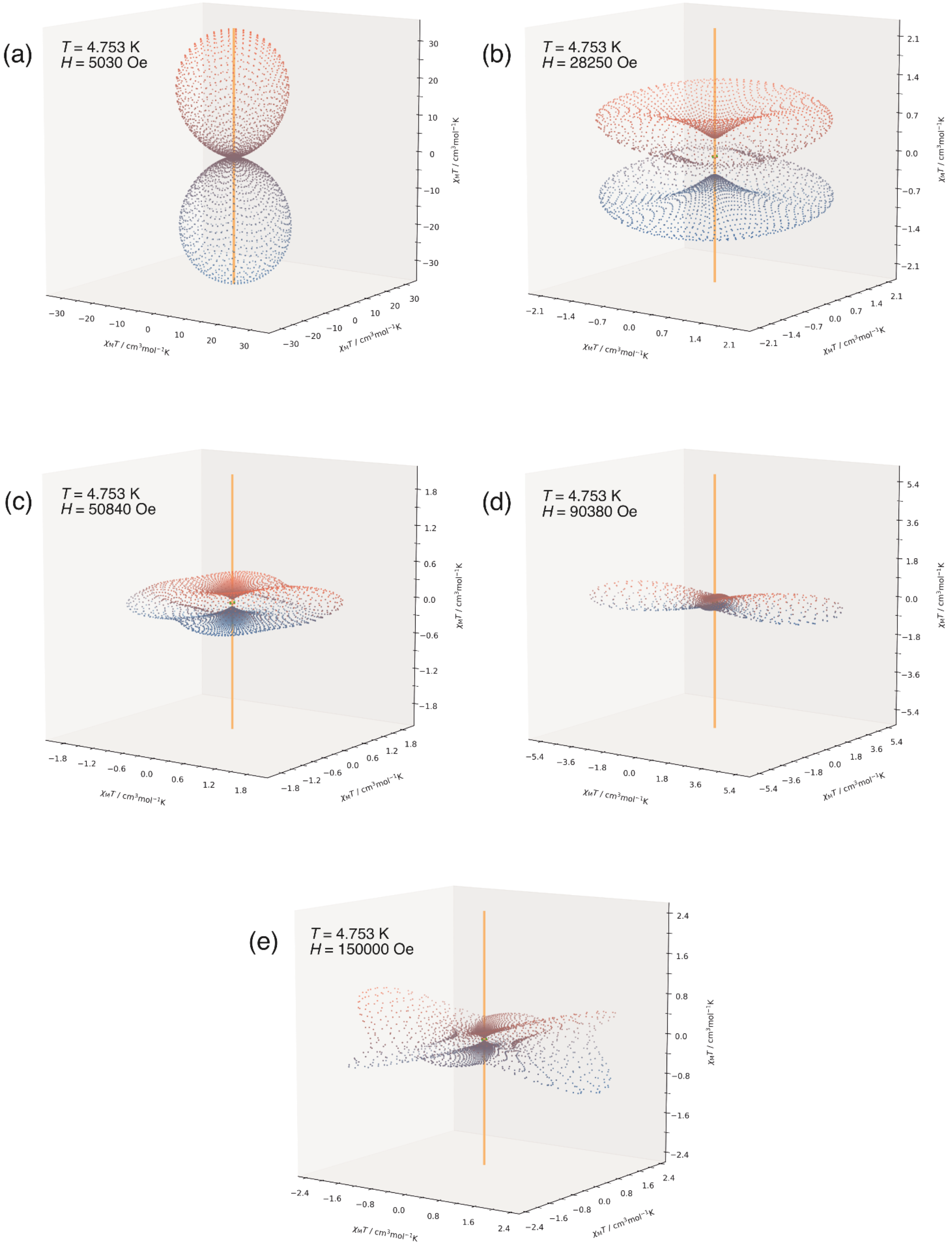

Fig. S26 The simulated 3-D dependencies of the $\chi_M T$ product for **ErAg** for the magnetic fields of 5.03 (a), 28.25 (b), 50.84 (c), 90.38 (d), and 150.00 kOe (e). The yellow rod represents an easy axis of the magnetization.

Table S16 (part 1/4) Calculated absorption energies for **EuAg** without additional scaling factors.

$^7F_0$ →	λ / nm	Energy / cm^{-1}	Oscillator strength /10^{11}	$^7F_0$ →	λ / nm	Energy / cm^{-1}	Oscillator strength /10^{11}
$^5D_0$	482.2	20738.3	7.5	$^5L_7$	333.7	29967.0	17.4
$^5D_1$	446.9	22376.4	0		333.7	29967.0	12.2
	446.5	22396.4	0	$^5G_2$	326	30674.8	2.5
	446.2	22411.5	0		326	30674.8	1.7
$^5D_2$	401.6	24900.4	1.3		326	30674.8	0.7
	401.2	24925.2	0.9		326	30674.8	1.8
	401	24937.7	0.5		325.6	30712.5	1.1
	400.8	24950.1	3.2	$^5G_3$	325.5	30722.0	0.1
	400.6	24962.6	0.2		324.9	30778.7	15.5
$^5D_3$	357.1	28003.4	0.1		324.8	30788.2	5.4
	357	28011.2	0.8		324.6	30807.1	56.6
	356.8	28026.9	0.4		324.3	30835.6	83.4
	356.7	28034.8	0.1		324.2	30845.2	19.3
	356.5	28050.5	2.9		324.1	30854.7	98.7
	356.4	28058.4	0.5	$^5G_4$	324	30864.2	20.7
	356.3	28066.2	0.2		323.6	30902.3	334.1
$^5L_6$	349.2	28636.9	178.4		323.6	30902.3	243.9
	349.2	28636.9	587.9		323.3	30931.0	90.4
	349.1	28645.1	55.2		323.3	30931.0	64.6
	349.1	28645.1	279		322.1	31046.3	6.3
	348.4	28702.6	40.8		322.1	31046.3	3.6
	348.3	28710.9	6.9		321.4	31113.9	4
	347.5	28777.0	2196.8		321.3	31123.6	10.1
	347.2	28801.8	3192	$^5G_5$	320.8	31172.1	3.2
	346.8	28835.1	1255.5		320.4	31211.0	29.2
	346	28901.7	11509.7		320.3	31220.7	16.2
	345.9	28910.1	21027.2		320.1	31240.2	74.1
	345.6	28935.2	28278.1		319.8	31269.5	165.9
	345.6	28935.2	31867.4		319.6	31289.1	46.9
$^5L_7$	336.5	29717.7	40.8		319.4	31308.7	125.1
	336.5	29717.7	51.7		319.4	31308.7	12.9
	336.5	29717.7	41.6		319.3	31318.5	188.6
	336.5	29717.7	46.5		319.2	31328.3	50.8
	336	29761.9	1.7		319.1	31338.1	95.3
	336	29761.9	5.2	$^5G_6$	318.8	31367.6	51.3
	335.3	20738.3	7.5		318.8	31367.6	263.5
	335.1	29841.8	108.1		318.6	31387.3	51.2
	334.8	29868.6	38		318.6	31387.3	890.5
	334.6	29886.4	51.2		318.5	31397.2	442.8
	334.6	29886.4	109.6		318.5	31397.2	1313.5
	334	29940.1	71.6		318.5	31397.2	998.1
	334	29940.1	71.8		318.4	31407.0	279.9

Table S16 (part 2/4) Calculated absorption energies for **EuAg** without additional scaling factors.

$^7F_0$ →	λ / nm	Energy / cm^{-1}	Oscillator strength /10^{11}	$^7F_0$ →	λ / nm	Energy / cm^{-1}	Oscillator strength /10^{11}
$^5G_6$	318.4	31407.0	2019.5	$^5I_9$	315.2	31725.9	359.4
	318.3	31416.9	4298		315.1	31736.0	211
	318.2	31426.8	3043.4		315	31746.0	192.6
	318.1	31436.7	789.5		315	31746.0	251
	318.1	31436.7	694.9		314.7	31776.3	31.1
$^5I_8$	317.9	31456.4	389.4		314.7	31776.3	56.9
	317.9	31456.4	7844.6		314.5	31796.5	11.2
	317.8	31466.3	5103.3		314.5	31796.5	64.5
	317.7	31476.2	1579.1	$^5I_{10}$	311.9	32061.6	5.1
	317.6	31486.1	568.5		311.9	32061.6	25.5
	317.5	31496.1	3230.4		311.5	32102.7	9.2
	317.5	31496.1	215.6		311.5	32102.7	31.8
	317.5	31496.1	3712.7		310.6	32195.8	5.4
	317.3	31515.9	840		310.6	32195.8	0.7
	317.3	31515.9	471.9		310.4	32216.5	5.9
	317.1	31535.8	435.9		310.4	32216.5	0.5
	317.1	31535.8	539.1		310.1	32247.7	2.3
	317.1	31535.8	1699.2		310	32258.1	4.5
	317	31545.7	1518.4		309.9	32268.5	0.1
	316.9	31555.7	721.6		309.7	32289.3	9.9
	316.9	31555.7	442.3		309.7	32289.3	4.3
	316.8	31565.7	889.6		309.5	32310.2	7.7
$^5D_4$	316.7	31575.6	1374.1		309.4	32320.6	27.7
	316.6	31585.6	496.2		309.2	32341.5	0.6
	316.3	31615.6	677.1		309.1	32352.0	1.7
	316.2	31625.6	583.9		308.5	32414.9	30.2
	316	31645.6	52.4		308.5	32414.9	25.9
	316	31645.6	20.2		308.3	32435.9	13.1
	315.9	31655.6	136.2		308.3	32435.9	11.7
	315.8	31665.6	21.3	$^5H_3$	277.4	36049.0	1.2
	315.8	31665.6	7.5		277.3	36062.0	4
$^5I_9$	315.7	31675.6	14.6		277	36101.1	0.6
	315.7	31675.6	0.3		276.7	36140.2	3
	315.6	31685.7	197.5		276.5	36166.4	14.1
	315.6	31685.7	160.4		276.3	36192.5	0.8
	315.6	31685.7	69.5		276.1	36218.8	2
	315.5	31695.7	49.5	$^5H_7$	273.8	36523.0	22.1
	315.4	31705.8	155.5		273.7	36536.4	16.1
	315.3	31715.8	131.3		273.6	36549.7	11
	315.3	31715.8	529.5		273.6	36549.7	1.5
	315.2	31725.9	171.6		273.4	36576.4	161.4
	315.2	31725.9	93.5		273.3	36589.8	49.6

Table S16 (part 3/4) Calculated absorption energies for **EuAg** without additional scaling factors.

$^7F_0$ →	λ / nm	Energy / cm^{-1}	Oscillator strength /10^{11}	$^7F_0$ →	λ / nm	Energy / cm^{-1}	Oscillator strength /10^{11}
$^5H_7$	273.3	36589.8	68.2	$^5P_0$	250.7	39888.3	0.1
	273.2	36603.2	87.2	$^5F_2$	247.3	40436.7	3.5
	273.1	36616.6	119.1		247.2	40453.1	2
	273.1	36616.6	61.2		247.1	40469.4	13.3
	273	36630.0	47.5		247	40485.8	11.5
	272.9	36643.5	1.5		246.9	40502.2	4.4
	272.8	36656.9	29.9	$^5F_1$	246.7	40535.1	8.4
	272.7	36670.3	60.7		246.6	40551.5	32.6
	272.7	36670.3	19.4		246.5	40568.0	7.2
$^5H_4$	272.6	36683.8	62.7	$^5F_3$	246.4	40584.4	50.5
	272.6	36683.8	84.7		246.4	40584.4	18.5
	272.5	36697.2	45.5		246.3	40600.9	198.7
	272.5	36697.2	21.7		246.3	40600.9	53.1
	272.4	36710.7	32.4		246.2	40617.4	84.3
	272.1	36751.2	44.8		246.2	40617.4	305.8
	272.1	36751.2	46.8		246.1	40633.9	69.3
	271.9	36778.2	94.2	$^5F_4$	246.1	40633.9	18
	271.9	36778.2	71		246.1	40633.9	0.3
$^5H_5$	270.9	36914.0	11.6		246	40650.4	48.9
	270.9	36914.0	551.9		246	40650.4	117.8
	270.9	36914.0	127.1		246	40650.4	4.1
	270.8	36927.6	319.7		245.9	40666.9	16.8
	270.6	36954.9	2475.8		245.7	40700.0	2.2
	270.6	36954.9	3997		245.6	40716.6	0.9
	270.5	36968.6	7943.6		245.4	40749.8	1
	270.5	36968.6	8719.6	$^5F_5$	243.6	41050.9	104.6
	270.4	36982.2	7156.5		243.6	41050.9	14.1
	270.3	36995.9	761.5		243.5	41067.8	56.2
	270.3	36995.9	2035.7		243.5	41067.8	5.9
$^5H_6$	270.2	37009.6	1482.8		243.4	41084.6	113
	270.2	37009.6	1425.4		243.4	41084.6	25.5
	270.1	37023.3	1554		243.4	41084.6	9.9
	270	37037.0	701		243.4	41084.6	10.4
	269.8	37064.5	3859.6		243.3	41101.5	52
	269.7	37078.2	534.4		243.3	41101.5	67.2
	269.7	37078.2	1505.1		243.3	41101.5	160
	269.6	37092.0	2660.1	$^5I_4$	243.3	41101.5	32.7
	269.4	37119.5	1753.5		243.2	41118.4	54.9
	269.3	37133.3	178.9		243.2	41118.4	13.4
	269.3	37133.3	92		243.1	41135.3	43.6
	269.3	37133.3	65.1		243.1	41135.3	51.8
	269.2	37147.1	152.4		243.1	41135.3	10.8

Table S16 (part 4/4) Calculated absorption energies for **EuAg** without additional scaling factors.

$^7F_0$ →	λ / nm	Energy / cm^{-1}	Oscillator strength /10^{11}	$^7F_0$ →	λ / nm	Energy / cm^{-1}	Oscillator strength /10^{11}
$^5I_4$	243	41152.3	27.7	$^5I_6$	240.1	41649.3	21.9
	243	41152.3	3.2		240.1	41649.3	23.4
	242.9	41169.2	11.3		240	41666.7	184.7
$^5I_5$	240.7	41545.5	630.5		240	41666.7	190.5
	240.7	41545.5	2459.4		240	41666.7	18.2
	240.6	41562.8	1336.3		239.9	41684.0	201
	240.6	41562.8	787.8	$^5I_7$	239.8	41701.4	178.8
	240.5	41580.0	312.3		239.8	41701.4	195.2
	240.5	41580.0	1200.4		239.8	41701.4	184.4
	240.5	41580.0	3448.7		239.7	41718.8	260.9
	240.4	41597.3	557.7		239.7	41718.8	81.3
	240.4	41597.3	5273.9		239.7	41718.8	95.6
	240.4	41597.3	2408.6		239.6	41736.2	25.4
	240.3	41614.6	2949.6		239.5	41753.7	35.3
$^5I_6$	240.3	41614.6	222.5		239.4	41771.1	78.3
	240.3	41614.6	1168.6		239.4	41771.1	38.3
	240.3	41614.6	466.2		239.4	41771.1	59.8
	240.2	41632.0	1124.2		239.3	41788.5	55.8
	240.2	41632.0	270.1		239.3	41788.5	22
	240.2	41632.0	970.5		239.2	41806.0	17.9
	240.1	41649.3	135.8		239.2	41806.0	24.4

Table S17 (part 1/4) Calculated absorption energies for **EuAg** shifted to match the experimental data.

$^7F_0$ →	λ / nm	Energy / cm^{-1}	Oscillator strength /10^{11}	$^7F_0$ →	λ / nm	Energy / cm^{-1}	Oscillator strength /10^{11}
$^5D_0$	586.9	20738.3	7.5	$^5L_7$	380.7	29967.0	17.4
$^5D_1$	535.4	22376.4	0		380.7	29967.0	12.2
	534.9	22396.4	0	$^5G_2$	370.7	30674.8	2.5
	534.5	22411.5	0		370.7	30674.8	1.7
$^5D_2$	471.7	24900.4	1.3		370.7	30674.8	0.7
	471.1	24925.2	0.9		370.7	30674.8	1.8
	470.9	24937.7	0.5		370.1	30712.5	1.1
	470.7	24950.1	3.2	$^5G_3$	370.1	30722.0	0.1
	470.3	24962.6	0.2		369.3	30778.7	15.5
$^5D_3$	411.5	28003.4	0.1		369.2	30788.2	5.4
	411.3	28011.2	0.8		368.9	30807.1	56.6
	411.1	28026.9	0.4		368.5	30835.6	83.4
	410.9	28034.8	0.1		368.4	30845.2	19.3
	410.7	28050.5	2.9		368.2	30854.7	98.7
	410.5	28058.4	0.5	$^5G_4$	368.2	30864.2	20.7
	410.3	28066.2	0.2		367.6	30902.3	334.1
$^5L_6$	401.1	28636.9	178.4		367.6	30902.3	243.9
	401.1	28636.9	587.9		367.2	30931.0	90.4
	400.9	28645.1	55.2		367.2	30931.0	64.6
	400.9	28645.1	279		365.7	31046.3	6.3
	400	28702.6	40.8		365.6	31046.3	3.6
	399.9	28710.9	6.9		364.8	31113.9	4
	398.7	28777.0	2196.8		364.6	31123.6	10.1
	398.4	28801.8	3192	$^5G_5$	364	31172.1	3.2
	397.9	28835.1	1255.5		363.5	31211.0	29.2
	396.7	28901.7	11509.7		363.3	31220.7	16.2
	396.7	28910.1	21027.2		363.1	31240.2	74.1
	396.3	28935.2	28278.1		362.7	31269.5	165.9
	396.2	28935.2	31867.4		362.5	31289.1	46.9
$^5L_7$	384.4	29717.7	40.8		362.3	31308.7	125.1
	384.4	29717.7	51.7		362.2	31308.7	12.9
	384.4	29717.7	41.6		362	31318.5	188.6
	384.4	29717.7	46.5		361.9	31328.3	50.8
	383.7	29761.9	1.7		361.8	31338.1	95.3
	383.7	29761.9	5.2	$^5G_6$	361.5	31367.6	51.3
	382.8	20738.3	7.5		361.4	31367.6	263.5
	382.5	29841.8	108.1		361.2	31387.3	51.2
	382.2	29868.6	38		361.2	31387.3	890.5
	381.9	29886.4	51.2		361.1	31397.2	442.8
	381.8	29886.4	109.6		361.1	31397.2	1313.5
	381.1	29940.1	71.6		361	31397.2	998.1
	381.1	29940.1	71.8		360.9	31407.0	279.9

Table S17 (part 2/4) Calculated absorption energies for **EuAg** shifted to match the experimental data.

$^7F_0$ →	λ / nm	Energy / cm^{-1}	Oscillator strength /10^{11}	$^7F_0$ →	λ / nm	Energy / cm^{-1}	Oscillator strength /10^{11}
$^5G_6$	360.9	31407.0	2019.5	$^5I_9$	356.8	31725.9	359.4
	360.8	31416.9	4298		356.7	31736.0	211
	360.6	31426.8	3043.4		356.6	31746.0	192.6
	360.5	31436.7	789.5		356.5	31746.0	251
	360.5	31436.7	694.9		356.2	31776.3	31.1
$^5I_8$	360.3	31456.4	389.4		356.2	31776.3	56.9
	360.2	31456.4	7844.6		355.9	31796.5	11.2
	360.2	31466.3	5103.3		355.9	31796.5	64.5
	360	31476.2	1579.1	$^5I_{10}$	352.6	32061.6	5.1
	360	31486.1	568.5		352.6	32061.6	25.5
	359.8	31496.1	3230.4		352	32102.7	9.2
	359.8	31496.1	215.6		352	32102.7	31.8
	359.7	31496.1	3712.7		350.9	32195.8	5.4
	359.5	31515.9	840		350.9	32195.8	0.7
	359.5	31515.9	471.9		350.7	32216.5	5.9
	359.3	31535.8	435.9		350.6	32216.5	0.5
	359.2	31535.8	539.1		350.3	32247.7	2.3
	359.2	31535.8	1699.2		350.2	32258.1	4.5
	359.1	31545.7	1518.4		350	32268.5	0.1
	359	31555.7	721.6		349.8	32289.3	9.9
	358.9	31555.7	442.3		349.7	32289.3	4.3
	358.9	31565.7	889.6		349.5	32310.2	7.7
$^5D_4$	358.7	31575.6	1374.1		349.4	32320.6	27.7
	358.6	31585.6	496.2		349.1	32341.5	0.6
	358.2	31615.6	677.1		349.1	32352.0	1.7
	358.1	31625.6	583.9		348.3	32414.9	30.2
	357.9	31645.6	52.4		348.3	32414.9	25.9
	357.8	31645.6	20.2		348	32435.9	13.1
	357.7	31655.6	136.2		348	32435.9	11.7
	357.6	31665.6	21.3	$^5H_3$	309.2	36049.0	1.2
	357.5	31665.6	7.5		308.9	36062.0	4
$^5I_9$	357.5	31675.6	14.6		308.6	36101.1	0.6
	357.4	31675.6	0.3		308.3	36140.2	3
	357.4	31685.7	197.5		308	36166.4	14.1
	357.3	31685.7	160.4		307.7	36192.5	0.8
	357.3	31685.7	69.5		307.5	36218.8	2
	357.2	31695.7	49.5	$^5H_7$	304.6	36523.0	22.1
	357	31705.8	155.5		304.6	36536.4	16.1
	357	31715.8	131.3		304.5	36549.7	11
	357	31715.8	529.5		304.4	36549.7	1.5
	356.9	31725.9	171.6		304.1	36576.4	161.4
	356.8	31725.9	93.5		304.1	36589.8	49.6

Table S17 (part 3/4) Calculated absorption energies for **EuAg** shifted to match the experimental data.

$^7F_0$ →	λ / nm	Energy / cm^{-1}	Oscillator strength /10^{11}	$^7F_0$ →	λ / nm	Energy / cm^{-1}	Oscillator strength /10^{11}
$^5H_7$	304	36589.8	68.2	$^5P_0$	276.3	39888.3	0.1
	304	36603.2	87.2	$^5F_2$	272.2	40436.7	3.5
	303.8	36616.6	119.1		272	40453.1	2
	303.8	36616.6	61.2		272	40469.4	13.3
	303.7	36630.0	47.5		271.8	40485.8	11.5
	303.6	36643.5	1.5		271.7	40502.2	4.4
	303.5	36656.9	29.9	$^5F_1$	271.5	40535.1	8.4
	303.3	36670.3	60.7		271.3	40551.5	32.6
	303.3	36670.3	19.4		271.3	40568.0	7.2
$^5H_4$	303.2	36683.8	62.7	$^5F_3$	271.1	40584.4	50.5
	303.2	36683.8	84.7		271.1	40584.4	18.5
	303.1	36697.2	45.5		271	40600.9	198.7
	303.1	36697.2	21.7		271	40600.9	53.1
	302.9	36710.7	32.4		270.9	40617.4	84.3
	302.6	36751.2	44.8		270.9	40617.4	305.8
	302.5	36751.2	46.8		270.8	40633.9	69.3
	302.3	36778.2	94.2	$^5F_4$	270.8	40633.9	18
	302.3	36778.2	71		270.7	40633.9	0.3
$^5H_5$	301.1	36914.0	11.6		270.7	40650.4	48.9
	301.1	36914.0	551.9		270.6	40650.4	117.8
	301	36914.0	127.1		270.6	40650.4	4.1
	301	36927.6	319.7		270.5	40666.9	16.8
	300.8	36954.9	2475.8		270.3	40700.0	2.2
	300.7	36954.9	3997		270.1	40716.6	0.9
	300.6	36968.6	7943.6		269.9	40749.8	1
	300.6	36968.6	8719.6	$^5F_5$	267.7	41050.9	104.6
	300.5	36982.2	7156.5		267.7	41050.9	14.1
	300.4	36995.9	761.5		267.6	41067.8	56.2
	300.4	36995.9	2035.7		267.6	41067.8	5.9
$^5H_6$	300.2	37009.6	1482.8		267.5	41084.6	113
	300.2	37009.6	1425.4		267.5	41084.6	25.5
	300.1	37023.3	1554		267.5	41084.6	9.9
	299.9	37037.0	701		267.5	41084.6	10.4
	299.7	37064.5	3859.6		267.4	41101.5	52
	299.7	37078.2	534.4		267.4	41101.5	67.2
	299.6	37078.2	1505.1		267.4	41101.5	160
	299.5	37092.0	2660.1	$^5I_4$	267.3	41101.5	32.7
	299.3	37119.5	1753.5		267.3	41118.4	54.9
	299.1	37133.3	178.9		267.2	41118.4	13.4
	299.1	37133.3	92		267.2	41135.3	43.6
	299	37133.3	65.1		267.1	41135.3	51.8
	299	37147.1	152.4		267.1	41135.3	10.8

Table S17 (part 4/4) Calculated absorption energies for **EuAg** shifted to match the experimental data.

$^7F_0$ →	λ / nm	Energy / cm^{-1}	Oscillator strength /10^{11}	$^7F_0$ →	λ / nm	Energy / cm^{-1}	Oscillator strength /10^{11}
$^5I_4$	267	41152.3	27.7	$^5I_6$	263.5	21.9	263.5
	267	41152.3	3.2		263.5	23.4	263.5
	266.9	41169.2	11.3		263.4	184.7	263.4
$^5I_5$	264.2	41545.5	630.5		263.4	190.5	263.4
	264.2	41545.5	2459.4		263.3	18.2	263.3
	264.1	41562.8	1336.3		263.3	201	263.3
	264.1	41562.8	787.8	$^5I_7$	263.2	178.8	263.2
	264	41580.0	312.3		263.2	195.2	263.2
	264	41580.0	1200.4		263.1	184.4	263.1
	264	41580.0	3448.7		263	260.9	263
	263.9	41597.3	557.7		263	81.3	263
	263.9	41597.3	5273.9		263	95.6	263
	263.8	41597.3	2408.6		262.9	25.4	262.9
	263.8	41614.6	2949.6		262.7	35.3	262.7
$^5I_6$	263.8	41614.6	222.5		262.7	78.3	262.7
	263.8	41614.6	1168.6		262.7	38.3	262.7
	263.7	41614.6	466.2		262.7	59.8	262.7
	263.7	41632.0	1124.2		262.5	55.8	262.5
	263.7	41632.0	270.1		262.5	22	262.5
	263.6	41632.0	970.5		262.5	17.9	262.5
	263.6	41649.3	135.8		262.4	24.4	262.4

Table S18 Energy splitting of $^7F_{0–5}$ terms (states from 1-37) and the energy of the $^5D_0$ multiplet of Eu^{III} centers in **EuAg**.

State	Energy / cm^{-1}	State	Energy / cm^{-1}	State	Energy / cm^{-1}
1	0.000	14	1992.923	27	4063.918
2	287.478	15	2017.786	28	4111.083
3	397.562	16	2040.786	29	4129.585
4	469.587	17	2909.083	30	4169.857
5	971.230	18	2963.400	31	4198.116
6	1027.049	19	2984.471	32	4236.823
7	1076.335	20	3007.669	33	4248.503
8	1136.378	21	3033.403	34	4250.863
9	1153.578	22	3060.456	35	4272.985
10	1940.156	23	3096.318	36	4278.621
11	1953.272	24	3120.115	37	5199.639
12	1956.331	25	3136. 086	-	-
13	1980.351	26	4058.267	-	-

Table S19 Calculated emission spectrum for **EuAg** without additional scaling factors.

$^5D_0$ →	λ / nm	Energy / cm^{-1}	Oscillator strength /10^{11}
$^7F_0$	482.2	20737.6	6.1
$^7F_1$	490.0	20450.1	0.02
	491.6	20340.0	0.03
	493.4	20268.0	0.01
$^7F_2$	505.9	19766.4	2
	507.3	19710.6	2.8
	508.6	19661.3	2.6
	510.2	19601.2	0.2
	510.6	19584.0	1.2
$^7F_3$	531.9	18797.5	0.9
	532.4	18784.3	0.2
	532.4	18781.3	0.4
	533.1	18757.3	0.2
	533.5	18744.7	0.002
	534.2	18719.8	0.1
	534.8	18696.8	0.1
$^7F_4$	560.9	17828.5	12.3
	562.6	17774.2	13.5
	563.3	17753.1	21.4
	564.0	17729.9	10.8
	564.8	17704.2	1.3
	565.7	17677.2	69.8
	566.8	17641.3	38.6
	567.6	17617.5	6.4
	568.2	17601.5	2.8
$^7F_5$	599.5	16679.4	0.4
	599.7	16673.7	0.5
	601.4	16626.5	0.8
	602.1	16608.0	0.1
	603.6	16567.8	0.03
	604.6	16539.5	0.1
	606.0	16500.8	0.1
	606.5	16489.1	0.1
	606.5	16486.7	0.03
	607.4	16464.6	0.1
	607.6	16459.0	0.02

Table S20 Calculated emission spectrum for **EuAg** with intensity scaling factors presented in Table S21 and energies shifted to match the experimental data.

$^5D_0$ →	λ / nm	Energy / cm^{-1}	Oscillator strength /10^{11}
$^7F_0$	580.2	17234.2	1.8
$^7F_1$	590.0	16946.7	17.9
	593.9	16836.6	24.7
	596.5	16764.6	7.7
$^7F_2$	614.9	16263.0	43.7
	617.0	16207.1	22.6
	618.9	16157.9	57.6
	621.2	16097.8	5.4
	621.9	16080.6	26.0
$^7F_3$	653.8	15294.0	4.5
	654.4	15280.9	1
	654.5	15277.9	2
	655.6	15253.9	1
	656.1	15241.2	0.01
	657.2	15216.4	0.5
	658.2	15193.4	0.5
$^7F_4$	698.0	14325.1	12.3
	700.7	14270.8	13.5
	701.8	14249.7	21.4
	702.9	14226.6	10.8
	704.2	14200.8	1.3
	705.5	14173.7	69.8
	707.3	14137.9	38.6
	708.5	14114.1	6.4
	709.3	14098.1	2.8
$^7F_5$	758.9	13175.9	0.4
	759.3	13170.3	0.5
	762.0	13123.1	0.8
	763.0	13104.6	0.1
	765.4	13064.4	0.03
	767.1	13036,.1	0.1
	769.4	12997.4	0.1
	770.0	12985.7	0.1
	770.2	12983.4	0.03
	771.5	12961.2	0.1
	771.8	12955.6	0.02

Table S21 Experimental intensity scaling factors for transitions between the $^5D_0$ and $^7F_{0–5}$ terms for **EuAg**.

Transition from $^5D_0$ to	Intensity experimental scaling factor
$^7F_0$	0.3
$^7F_1$	900
$^7F_2$	22
$^7F_3$	5
$^7F_4$	-
$^7F_5$	-

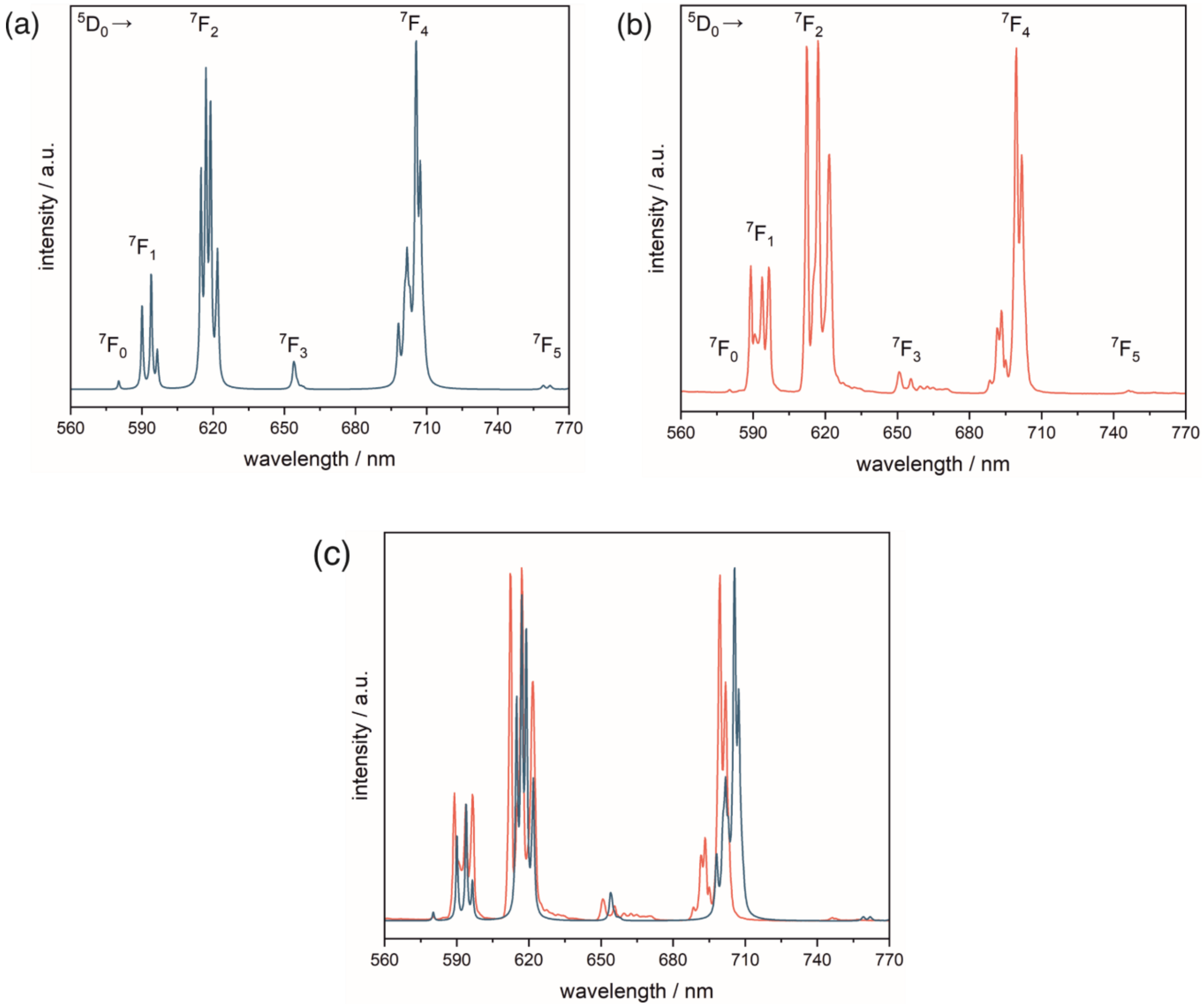

Fig. S27 Theoretical (calculated) emission spectrum of **EuAg** with simulated spectral lines considering the experimental scaling factors (a), the experimental emission spectra of **EuAg** at 10 K under excitation of λ_{exc} = 275 nm (b), the comparison of the theoretical spectrum with the experimental one (c). The theoretical spectrum was shifted to match the wavelength corresponding to the $^5D_0 \rightarrow {}^5F_0$ electronic transition. It should be noted here that the observed splitting of the emission bands corresponding to the indicated electronic transitions is related mainly to the crystal field effect that results in the energy splitting of the excited $^5F_{1-5}$ multiplets into the series of m_J levels. There is no influence of the crystal field on the emissive $^5D_0$ multiplet, as it reveals the $J = 0$ value; thus, there is only a single m_J level ($m_J = 0$). Similarly, the ground state of $^5F_0$ is also not split in the crystal field due to the analogous reason. However, the other $^5F_{1-5}$ multiplets are split in the crystal field of Eu(III) complexes into a series of m_J levels. As Eu(III) ions are of a non-Kramers character, the degeneracy of the sublevels corresponding to the $+m_J$ and $-m_J$ values is not ensured in the low-symmetry complexes (as is the case of Eu(III) complexes in **EuAg**). Therefore, in principle, the energies of all m_J levels with the total number of $(2J+1)$ for the particular multiplet can differ, resulting in the $(2J+1)$ components of the emission band. However, often the energies of two closely related sublevels corresponding to the $+m_J$ and $-m_J$ values can be very similar, leading to the observation of a limited number of emission components, e.g., 4 components for the emission band related to the $^5D_0 \rightarrow {}^5F_3$ ($J = 3$) electronic transition (corresponding to the $m_J = 0$, and three pairs of sublevels with $\pm m_J$) instead of the theoretical number of 7 components. This scenario (i.e., the expected number of crystal field states within the electronic multiplets, and the resulting number of related emission components) works even if the symmetry is low, and the m_J states are highly mixed.[S19,S24–S26] The eventual additional emission peaks within the spectrum of Eu(III) complexes can appear due to the emission from the excited $^5D_1$ multiplet, which might also be predicted by the *ab initio* calculations, but they are not considered here as they are expected to be very weak and they are not crucial in the context of the investigated optical thermometry.[S19]

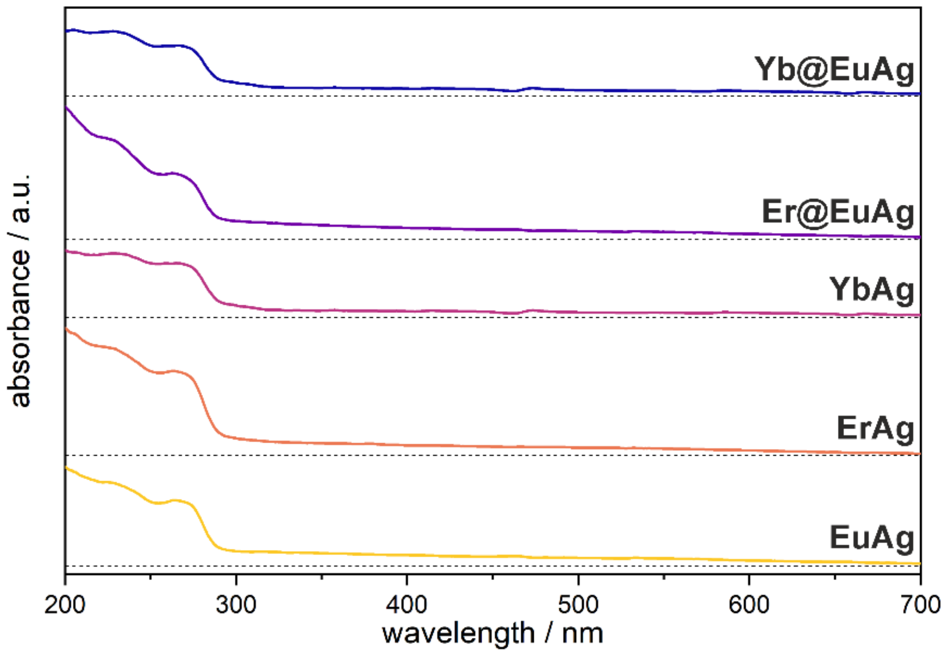

Fig. S28 Room-temperature solid-state UV-vis absorption spectra for **EuAr**, **ErAg**, **YbAg**, **Er@EuAg**, and **Yb@EuAg**, collected in the 200−700 nm range.

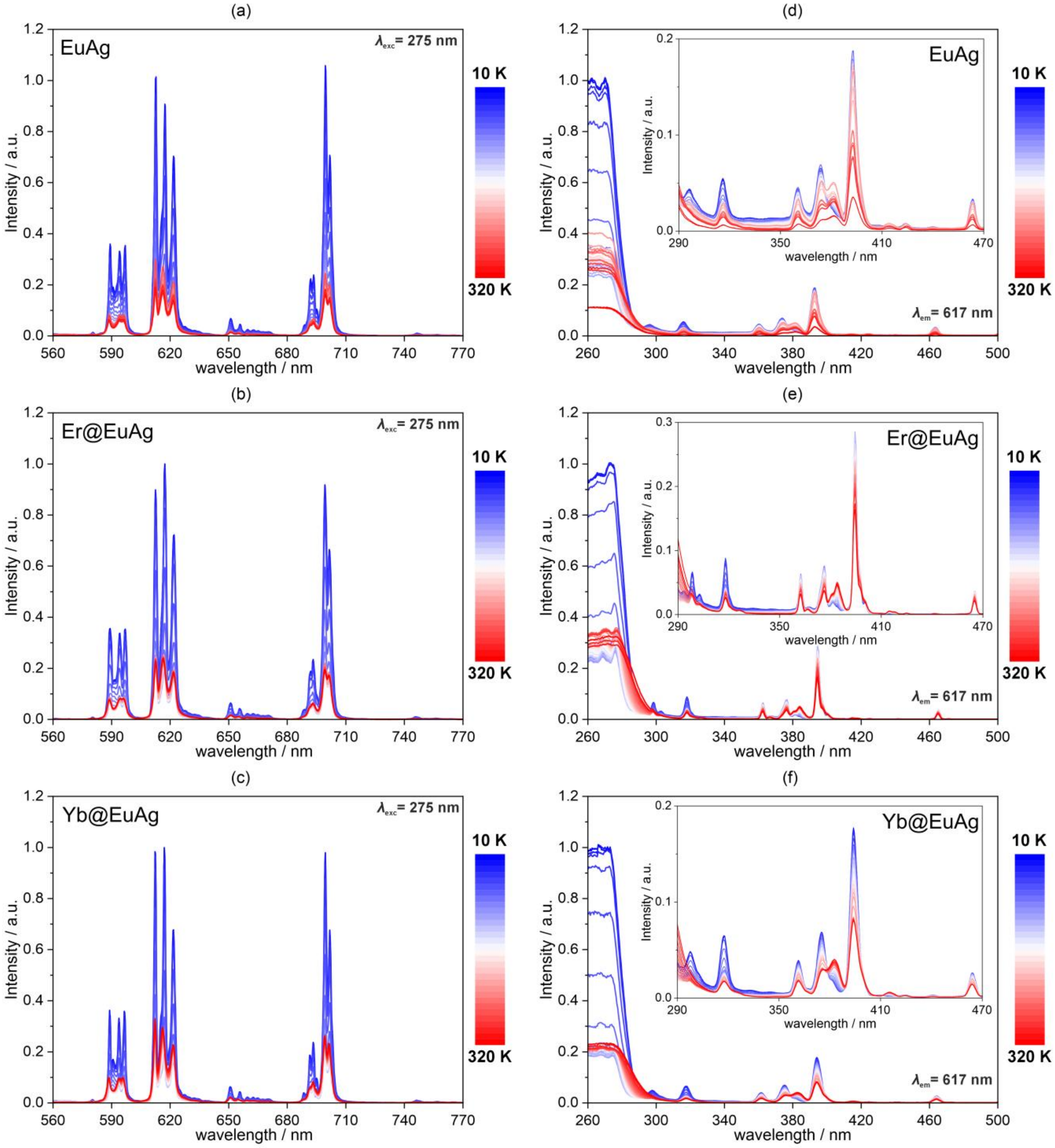

Fig. S29 Temperature-variable photoluminescence spectra, gathered in the 10−320 K temperature range: emission spectra for **EuAg** (a), **Er@EuAg** (b), and **Yb@EuAg** (c), under the excitation of λ_{exc} = 275 nm, presented in 550−770 nm range; the excitation spectra for **EuAg,** (d), **Er@EuAg**nm (e), and **Yb@EuAg**, for the emission at λ_{em} = 617 nm, (f) presented in 260−500 nm range, with a close-up of the 290−470 nm range presented in the insets.

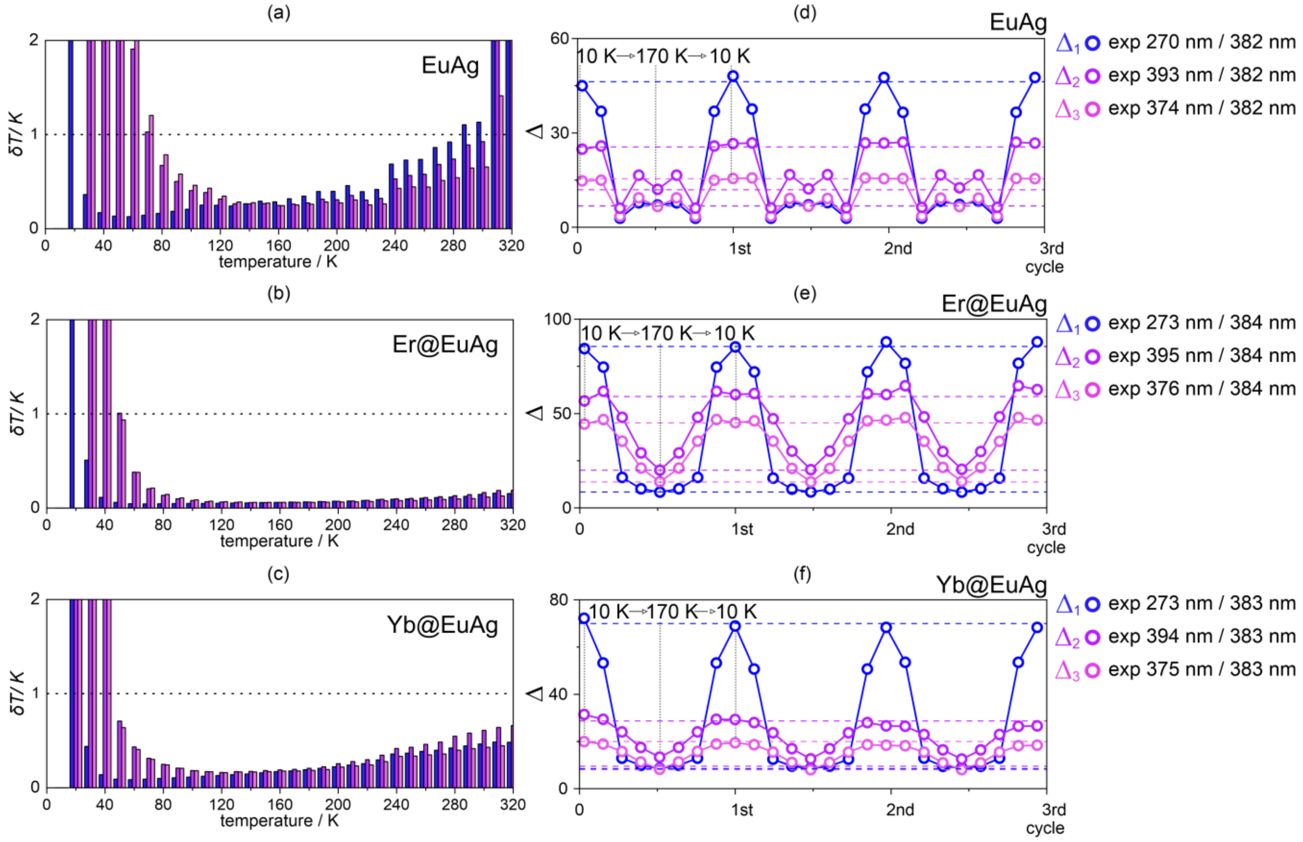

Fig. S30 Characteristics of the ratiometric luminescence thermometry of **EuAg** (a,d), **Er@EuAg** (b,e) and **Yb@EuAg** (c,f), exploring the intensities at the maxima of the selected excitation peaks (Fig. 5): the temperature uncertainties in the function of the temperature, $\delta T(T)$, (a–c); and the repeatability of the temperature dependence of each Δ parameter within three thermal cycles (e–f). The best-fit parameters are gathered in Table S22. Dashed lines in the (a–c) part represent the boundary of an arbitrary criterion for good-performing optical thermometers (i.e., $S_r > 1$ %K^{-1}, $\delta T < 1$ K).[S20] The related calibration curves are shown in the Fig. 6, main text.

Comment on Fig. S30 and Tables S22-S23 – ratiometric optical thermometry

For the design of ratiometric luminescent thermometry, the thermometric parameters were defined as the intensity ratio of two selected excitation bands, $\Delta = I_1/I_2$. The temperature dependencies of Δ parameters were employed to generate the thermometric calibration curves, $\Delta(T)$, which were fitted using the one-exponential Mott-Seitz model (equation 4, main text). To evaluate the related thermometric performance, we employed two common parameters, the relative thermal sensitivity, S_r (equation 5, main text), and the temperature uncertainty, δT (equation S3).[S20]

The δT is derived by using the equation for the experimental data of $\Delta(T)$ and the related best-fit $S_r(T)$ curves (equation S1):

$$\delta T(T) = \frac{\delta \Delta}{\Delta} \cdot \frac{1}{S_{\mathrm{r}}(T)} \tag{S3}$$

where ($\delta\Delta/\Delta$) is an experimental relative uncertainty of Δ at the indicated temperature.

At a certain temperature, the ($\delta\Delta/\Delta$) is estimated by using equation S2:

$$\frac{\delta \Delta}{\Delta} = \sqrt{\left(\frac{\delta I_1}{I_1}\right)^2 + \left(\frac{\delta I_2}{I_2}\right)^2} \tag{S4}$$

where δI_i is the uncertainty of the emission peak intensity.

For all the considered excitation peaks, used in the parametrization of the optical thermometry, this uncertainty was fixed at δI_i = 250 CPS, which corresponds to the background fluctuation level of the excitation spectra, while the I_i values are the emission intensities of the target peaks, taken from the raw excitation spectra.

Table S22 Best-fit parameters of the ratiometric thermometry calibration curves for **EuAg**, **Er@EuAg**, and **Yb@EuAg**, where *Δ* is defined as the ratio between the excitation peaks' intensities (at the maxima of the selected peaks; Fig. S30), obtained using the mono-exponential Mott–Seitz model (equation 5, main text).

Compound	Thermometric parameter (*Δ*)	Best-fit parameters		
		Δ_0	α_1	[$\Delta E_1/k_B$] / K
EuAg	$I^{\lambda=}_{270\ nm}/I^{\lambda=}_{382\ nm}$	49.7(15)	13.7(17)	172(12)
	$I^{\lambda=}_{374\ nm}/I^{\lambda=}_{382\ nm}$	3.02(2)	11.6(4)	407(7)
	$I^{\lambda=}_{393\ nm}/I^{\lambda=}_{382\ nm}$	8.18(5)	8.9(5)	403(11)
Er@EuAg	$I^{\lambda=}_{273\ nm}/I^{\lambda=}_{384\ nm}$	85.4(17)	58(10)	258(14)
	$I^{\lambda=}_{376\ nm}/I^{\lambda=}_{384\ nm}$	6.08(2)	24.4(6)	389(4)
	$I^{\lambda=}_{395\ nm}/I^{\lambda=}_{384\ nm}$	22.6(1)	18.4(9)	369(8)
Yb@EuAg	$I^{\lambda=}_{273\ nm}/I^{\lambda=}_{383\ nm}$	72.9(15)	46.7(74)	222(12)
	$I^{\lambda=}_{375\ nm}/I^{\lambda=}_{383\ nm}$	4.78(3)	15.2(6)	323(6)
	$I^{\lambda=}_{394\ nm}/I^{\lambda=}_{383\ nm}$	12.32(7)	13.2(5)	307(6)

Table S23 Temperature ranges for good-thermometric performance and the maximal S_r values of the thermometric calibration curves for **EuAg**, **Er@EuAg**, and **Yb@EuAg**, determined based on the temperature dependence of their excitation, where *Δ* parameters are defined as the ratio between the excitation peaks' intensities (at the maxima of the selected peaks; Fig. S30 and Table S22)

Compound	Thermometric parameter (*Δ*)	*T* range of good-thermometric performance ($S_r > 1\%\ K^{-1}$; δT < 1 K)	Maximal S_r value and related temperature
EuAg	$I^{\lambda=}_{270\ nm}/I^{\lambda=}_{382\ nm}$	32–114 K (range of 82 K)	2.13% K^{-1} (54.7 K)
	$I^{\lambda=}_{374\ nm}/I^{\lambda=}_{382\ nm}$	-	-
	$I^{\lambda=}_{393\ nm}/I^{\lambda=}_{382\ nm}$	-	-
Er@EuAg	$I^{\lambda=}_{273\ nm}/I^{\lambda=}_{384\ nm}$	37–154 K (117 K)	3.20% K^{-1} (64.0 K)
	$I^{\lambda=}_{376\ nm}/I^{\lambda=}_{384\ nm}$	81–165 K (84 K)	1.34% K^{-1} (111.5 K)
	$I^{\lambda=}_{395\ nm}/I^{\lambda=}_{384\ nm}$	86–151 K (65 K)	1.19% K^{-1} (111.2 K)
Yb@EuAg	$I^{\lambda=}_{273\ nm}/I^{\lambda=}_{383\ nm}$	32–139 K (107 K)	3.32% K^{-1} (57.2 K)
	$I^{\lambda=}_{375\ nm}/I^{\lambda=}_{383\ nm}$	76–142 K (66 K)	1.22% K^{-1} (100.6 K)
	$I^{\lambda=}_{394\ nm}/I^{\lambda=}_{383\ nm}$	76–131 K (55 K)	1.64% K^{-1} (97.8 K)

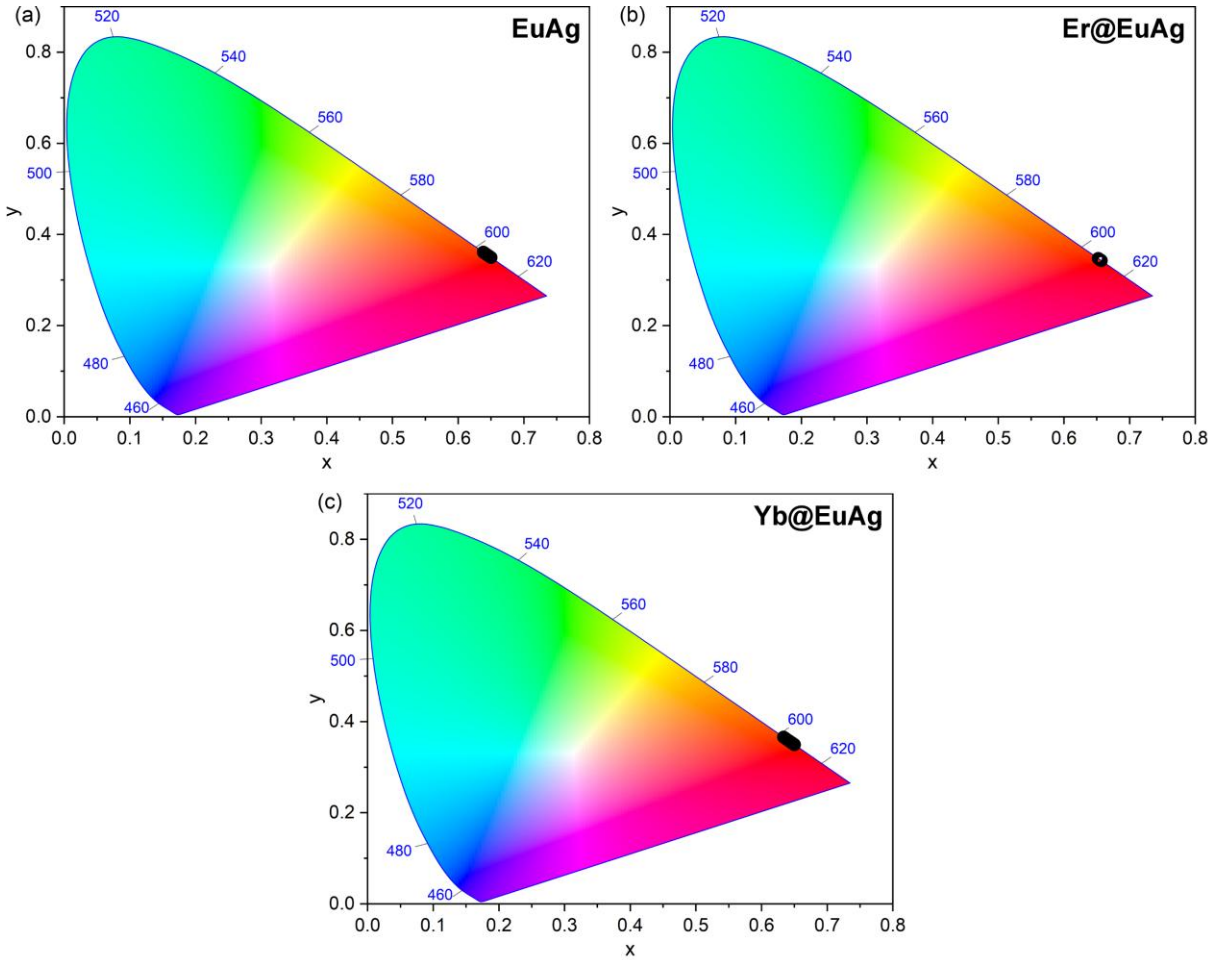

Fig. S31 The set of CIE 1931 chromaticity diagrams for temperature-variable photoluminescence data of **EuAg** (a), **Er@EuAg** (b), and **Yb@EuAg** (c), collected in the 10–310 K range under the λ_{exc} = 275 nm excitation. The related emission spectra are shown in Fig. S29, while the CIE 1931 chromaticity parameters are gathered in Table S24.

Table S24 The list of CIE 1931 chromaticity parameters for the solid-state emission patterns of **EuAg**, **Er@EuAg**, and **Yb@EuAg**, under the excitation of λ_{exc} = 275 nm, collected at the indicated temperatures.

Temperature / K	**EuAg**		**Er@EuAg**		**Yb@EuAg**	
	CIE 1931 chromaticity parameters					
	x	*y*	*x*	*y*	*x*	*y*
10	0.648	0.3520	0.656	0.344	0.647	0.353
20	0.647	0.353	0.655	0.344	0.647	0.353
30	0.645	0.354	0.655	0.344	0.647	0.353
40	0.643	0.356	0.656	0.344	0.646	0.353
50	0.642	0.358	0.655	0.344	0.645	0.354
60	0.641	0.359	0.654	0.345	0.643	0.357
70	0.640	0.360	0.653	0.347	0.637	0.361
80	0.639	0.360	0.652	0.347	0.636	0.364
90	0.6396	0.360	0.652	0.347	0.633	0.365
100	0.639	0.360	0.652	0.348	0.633	0.366
110	0.639	0.360	0.653	0.347	0.633	0.366
120	0.639	0.360	0.653	0.347	0.634	0.365
130	0.638	0.361	0.654	0.346	0.636	0.364
140	0.639	0.361	0.654	0.345	0.638	0.363
150	0.639	0.360	0.655	0.345	0.638	0.361
160	0.640	0.360	0.655	0.345	0.640	0.360
170	0.639	0.360	0.655	0.345	0.641	0.358
180	0.640	0.359	0.655	0.344	0.643	0.357
190	0.641	0.358	0.655	0.344	0.644	0.355
200	0.643	0.356	0.656	0.344	0.645	0.354
210	0.646	0.354	0.656	0.344	0.646	0.354
220	0.648	0.352	0.656	0.344	0.647	0.353
230	0.646	0.354	0.656	0.344	0.648	0.352
240	0.645	0.355	0.656	0.344	0.648	0.352
250	0.645	0.350	0.656	0.343	0.648	0.351
260	0.643	0.357	0.656	0.344	0.648	0.351
270	0.648	0.351	0.656	0.344	0.649	0.351
280	0.646	0.354	0.656	0.344	0.649	0.350
290	0.645	0.354	0.656	0.343	0.650	0.350
300	0.648	0.352	0.656	0.343	0.650	0.350
310	0.647	0.353	0.657	0.343	0.650	0.350
320	0.645	0.354	0.657	0.343	0.650	0.350

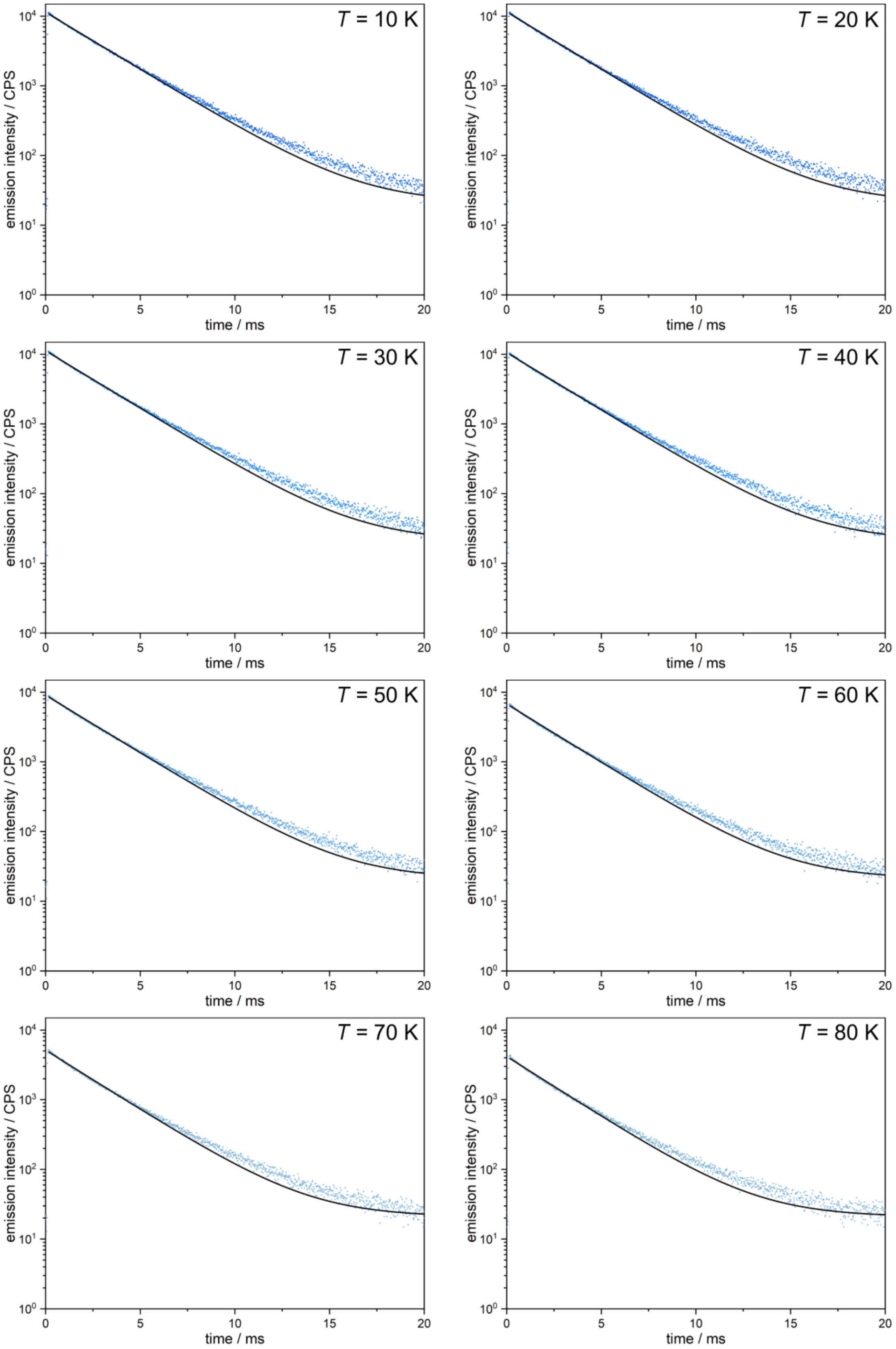

Fig. S32 Temperature-variable emission decay profiles for **EuAg**, gathered in the 10–80 K temperature range for λ_{exc} = 275 nm and λ_{em} = 617 nm. The experimental data were fitted using the mono-exponential decay function. The best-fit parameters are gathered in Table S25.

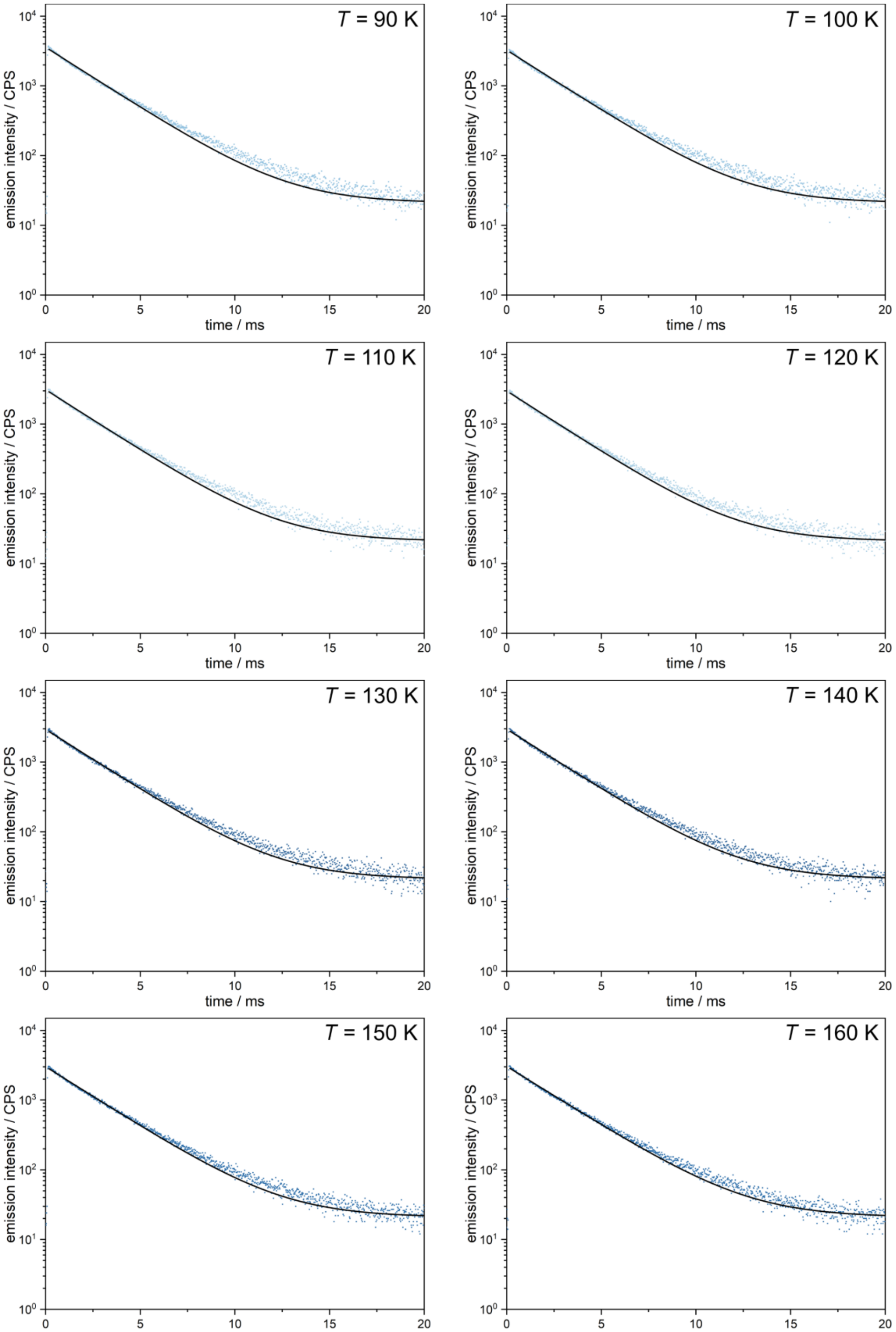

Fig. S33 Temperature-variable emission decay profiles for **EuAg**, gathered in the 90–160 K temperature range for λ_{exc} = 275 nm and λ_{em} = 617 nm. The experimental data were fitted using the mono-exponential decay function. The best-fit parameters are gathered in Table S25.

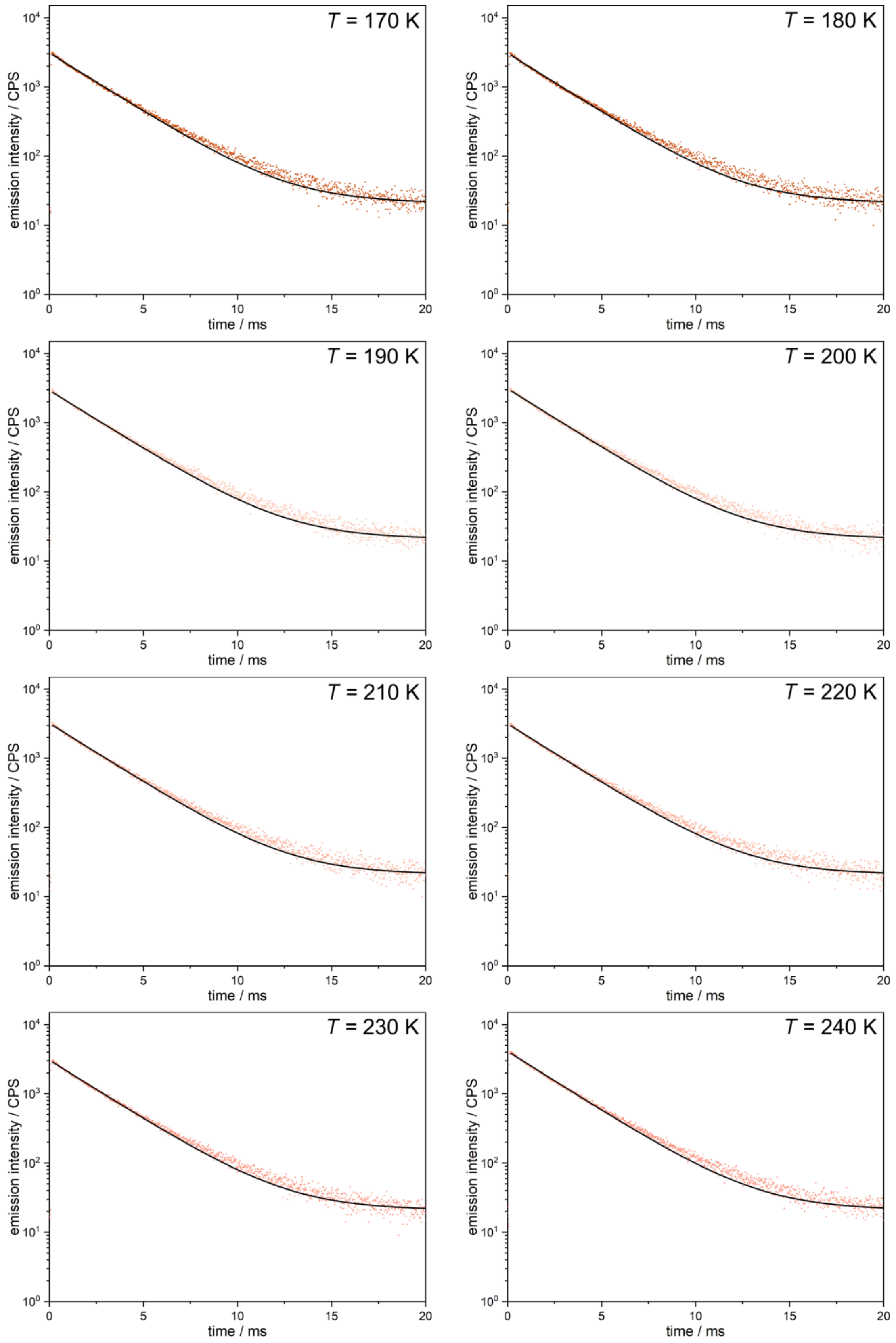

Fig. S34 Temperature-variable emission decay profiles for **EuAg**, gathered in the 170–240 K temperature range for λ_{exc} = 275 nm and λ_{em} = 617 nm. The experimental data were fitted using the mono-exponential decay function. The best-fit parameters are gathered in Table S25.

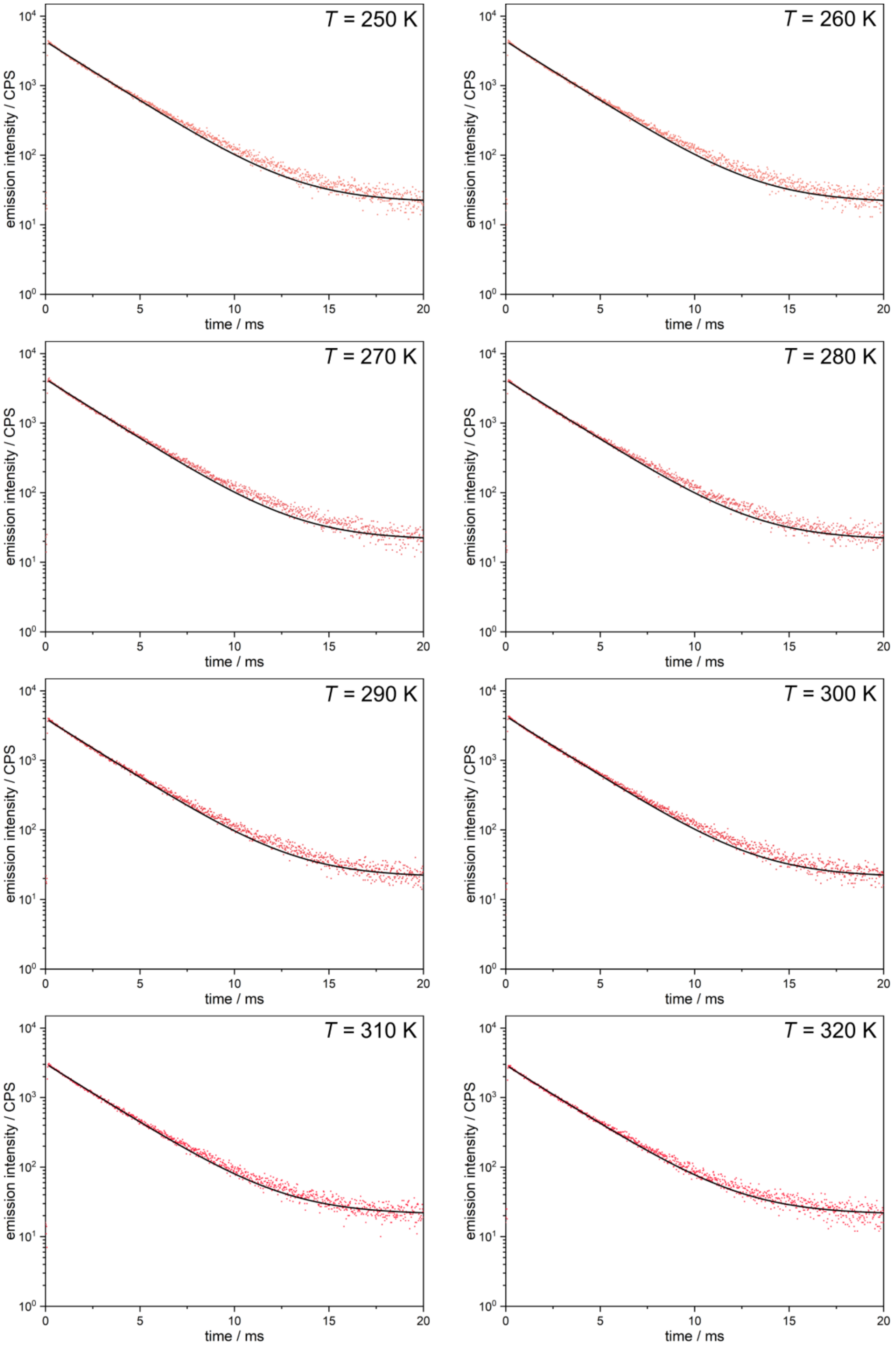

Fig. S35 Temperature-variable emission decay profiles for **EuAg**, gathered in the 250–320 K temperature range for λ_{exc} = 275 nm and λ_{em} = 617 nm. The experimental data were fitted using the mono-exponential decay function. The best-fit parameters are gathered in Table S25.

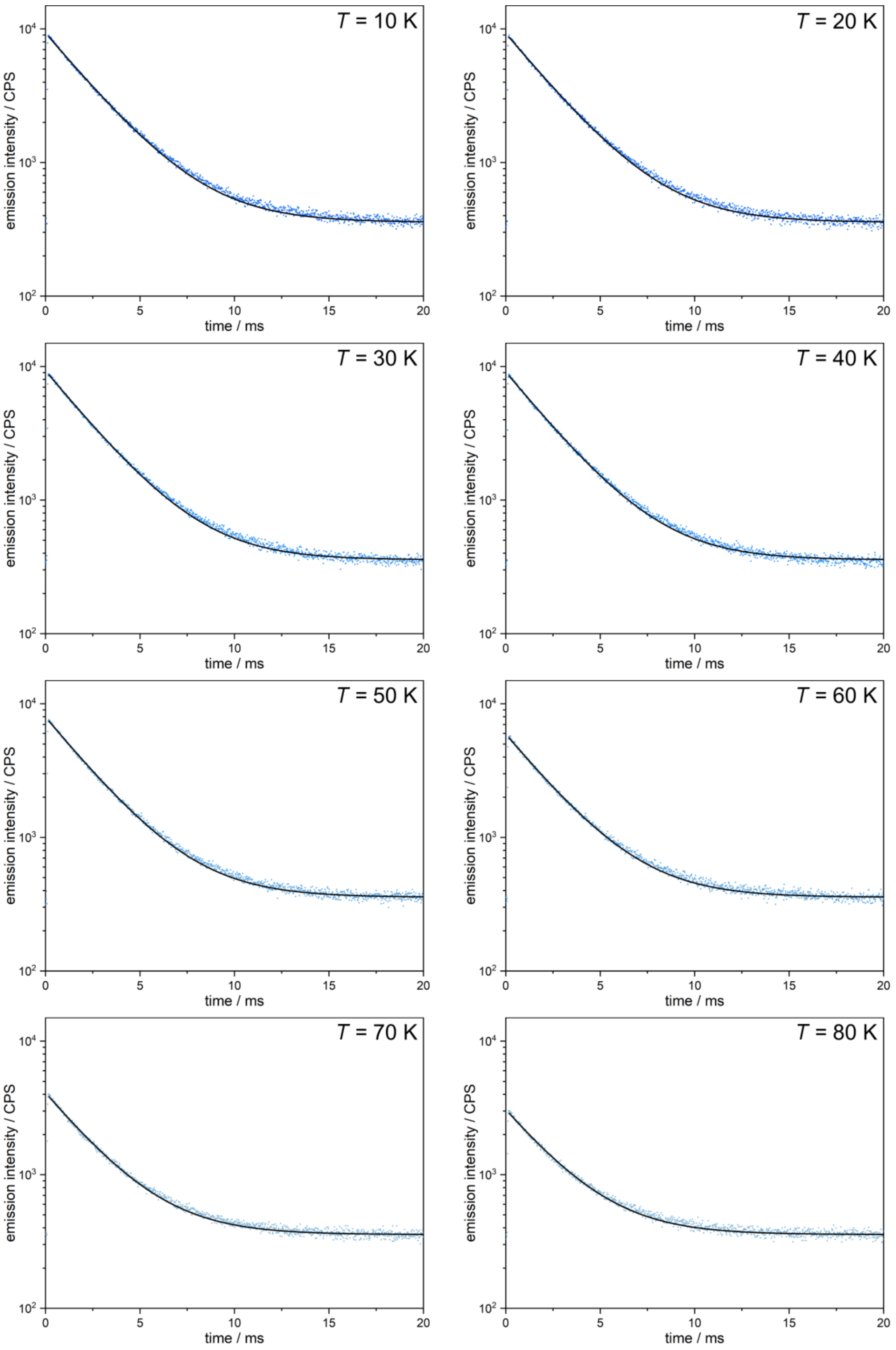

Fig. S36 Temperature-variable emission decay profiles for **Er@EuAg**, gathered in the 10–80 K temperature range for λ_{exc} = 275 nm and λ_{em} = 618 nm. The experimental data were fitted using the mono-exponential decay function. The best-fit parameters are gathered in Table S26.

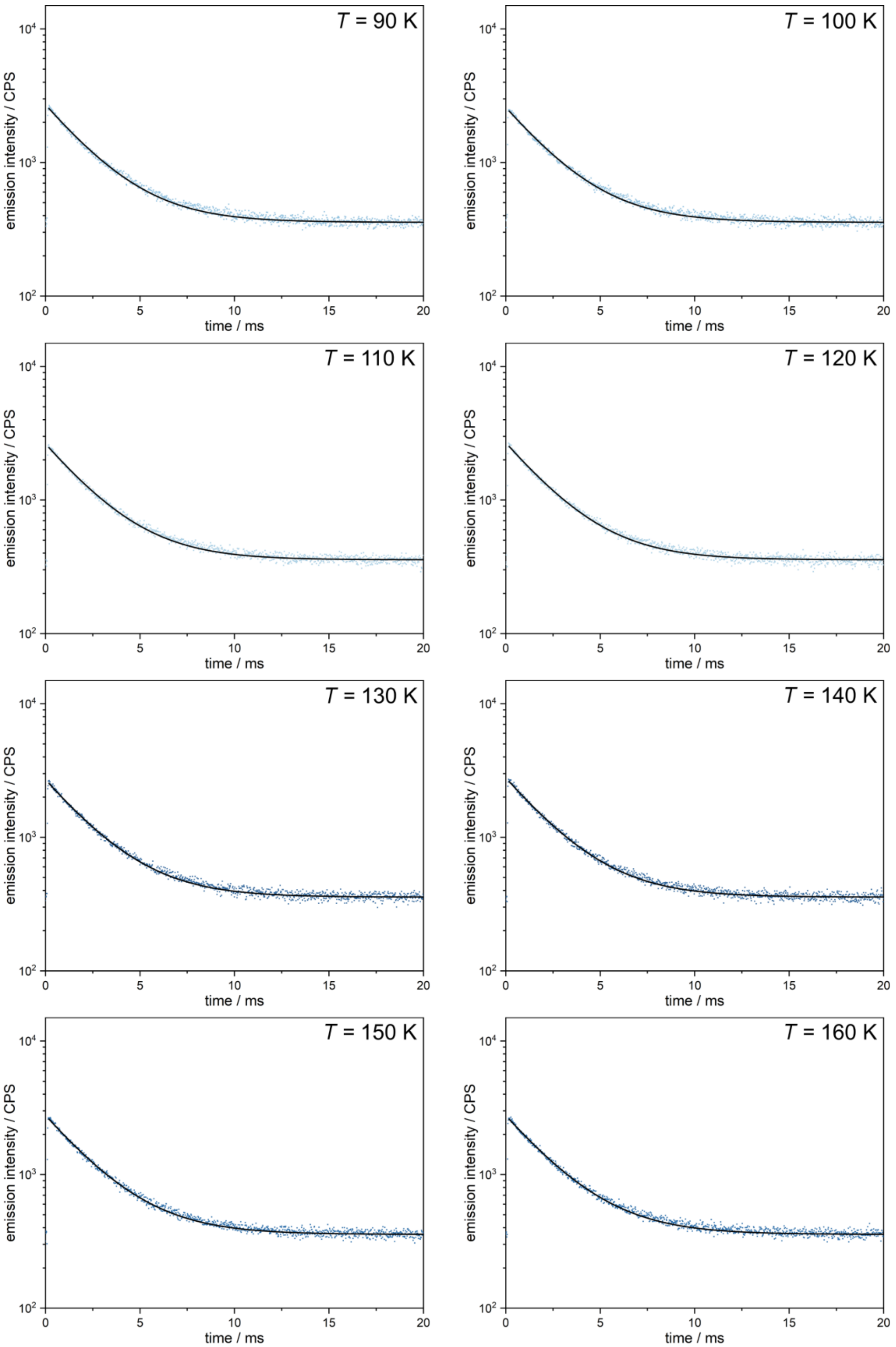

Fig. S37 Temperature-variable emission decay profiles for **Er@EuAg**, gathered in the 90–160 K temperature range for λ_{exc} = 275 nm and λ_{em} = 618 nm. The experimental data were fitted using the mono-exponential decay function. The best-fit parameters are gathered in Table S26.

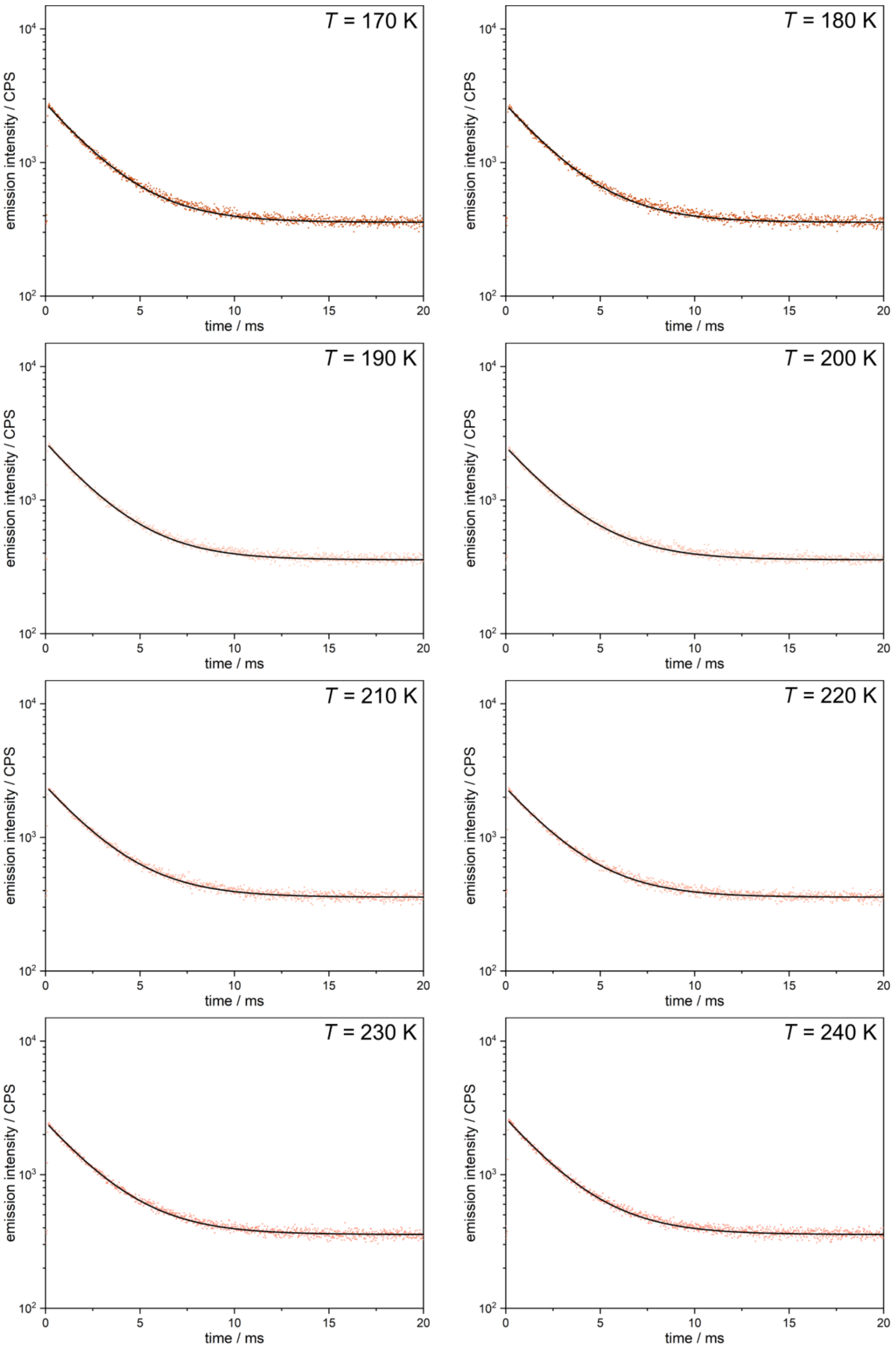

Fig. S38 Temperature-variable emission decay profiles for **Er@EuAg**, gathered in the 170–240 K temperature range for λ_{exc} = 275 nm and λ_{em} = 618 nm. The experimental data were fitted using the mono-exponential decay function. The best-fit parameters are gathered in Table S26.

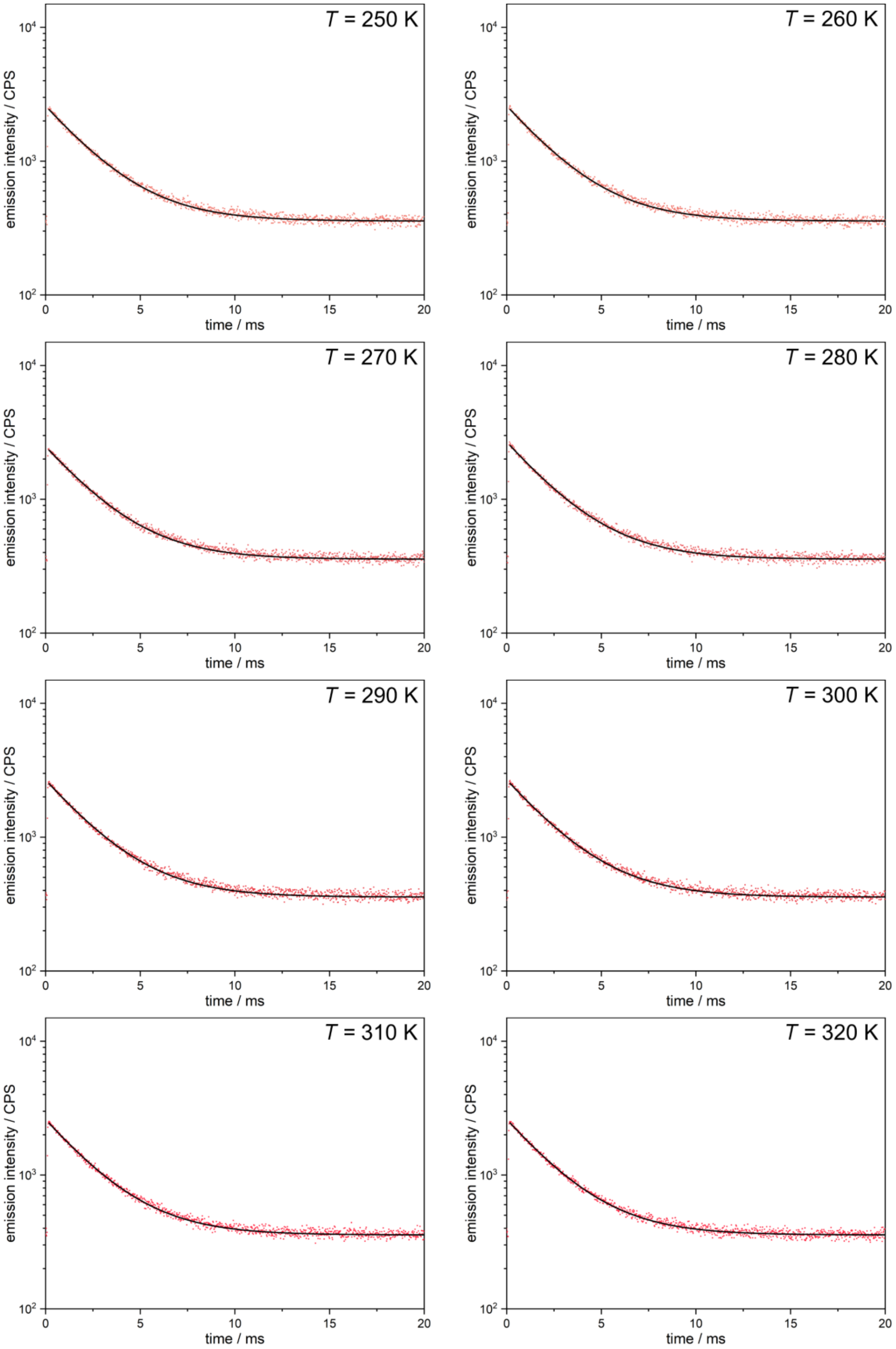

Fig. S39 Temperature-variable emission decay profiles for **Er@EuAg**, gathered in the 250–320 K temperature range for λ_{exc} = 275 nm and λ_{em} = 618 nm. The experimental data were fitted using the mono-exponential decay function. The best-fit parameters are gathered in Table S26.

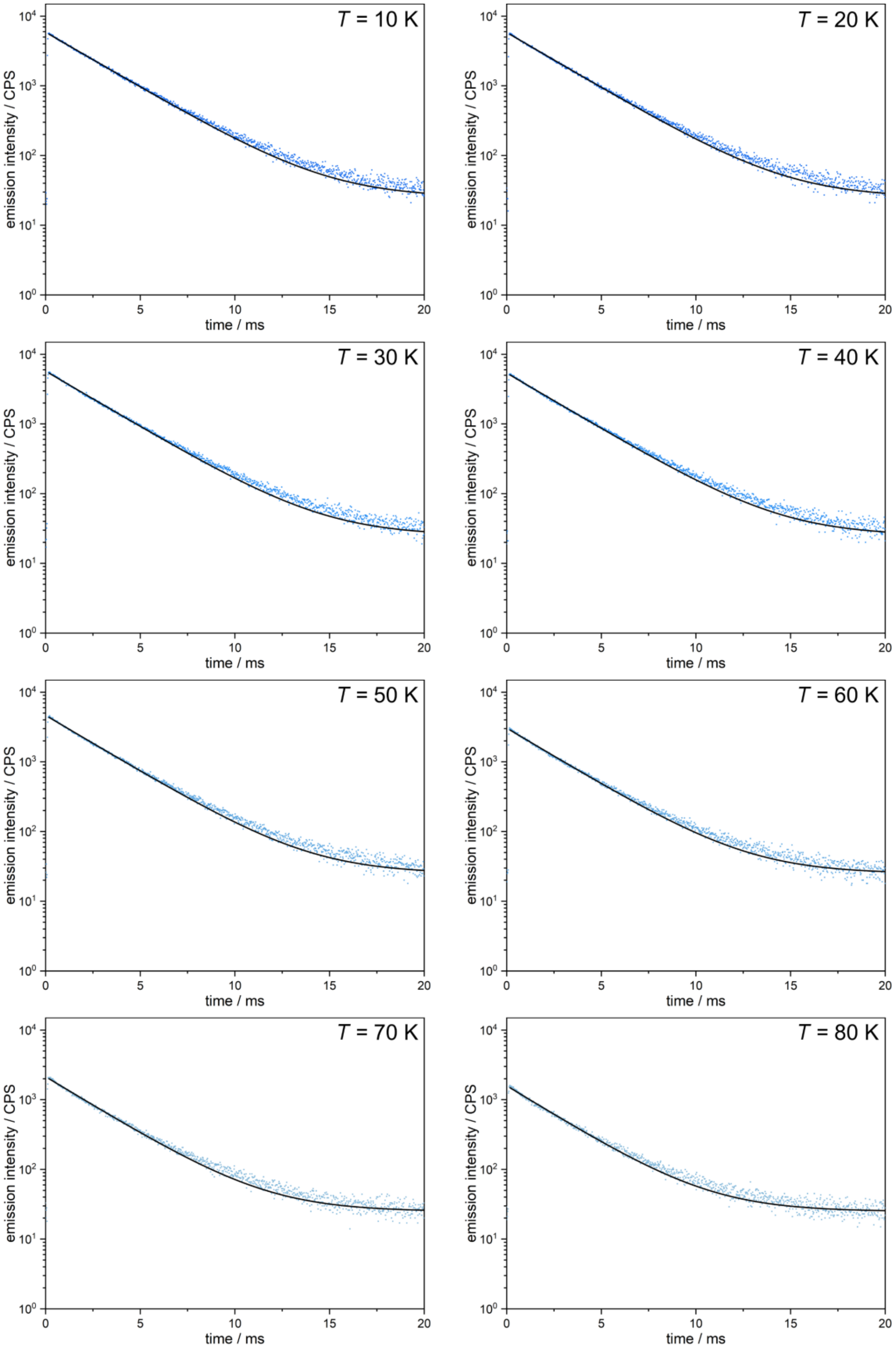

Fig. S40 Temperature-variable emission decay profiles for **Yb@EuAg**, gathered in the 10–80 K temperature range for λ_{exc} = 275 nm and λ_{em} = 617 nm. The experimental data were fitted using the mono-exponential decay function. The best-fit parameters are gathered in Table S27.

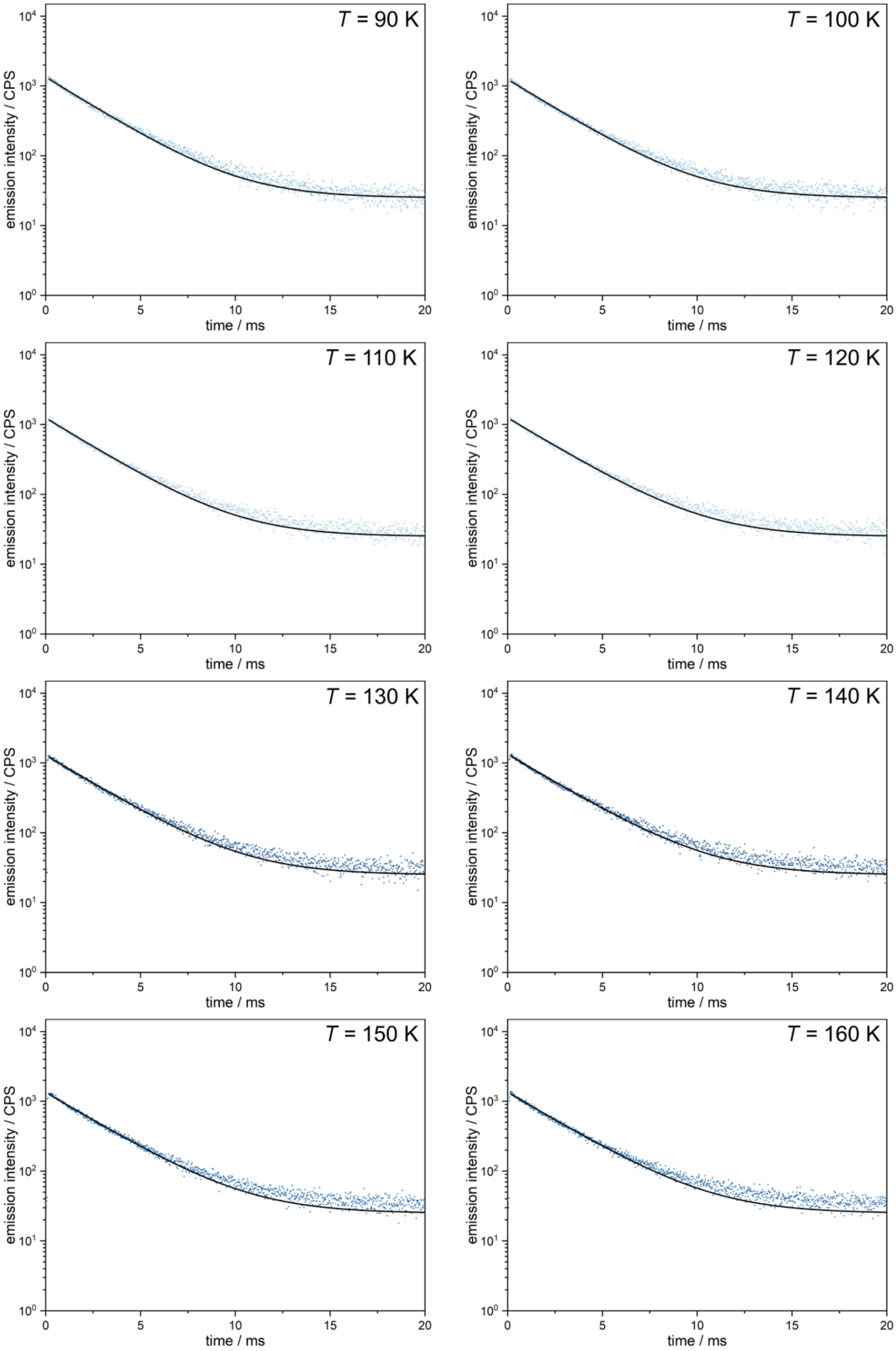

Fig. S41 Temperature-variable emission decay profiles for **Yb@EuAg**, gathered in the 90–160 K temperature range for λ_{exc} = 275 nm and λ_{em} = 617 nm. The experimental data were fitted using the mono-exponential decay function. The best-fit parameters are gathered in Table S27.

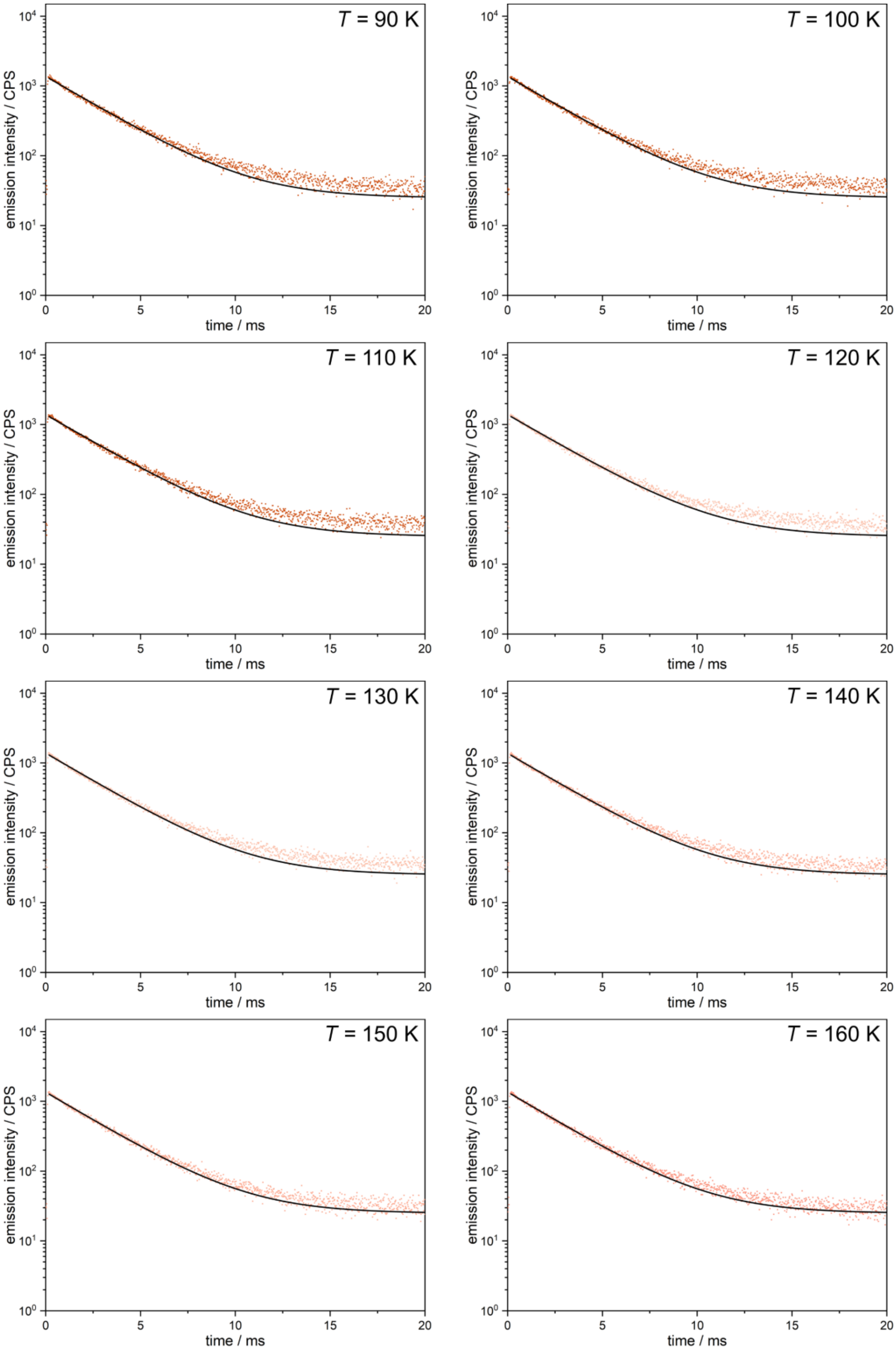

Fig. S42 Temperature-variable emission decay profiles for **Yb@EuAg**, gathered in the 170–240 K temperature range for λ_{exc} = 275 nm and λ_{em} = 617 nm. The experimental data were fitted using the mono-exponential decay function. The best-fit parameters are gathered in Table S27.

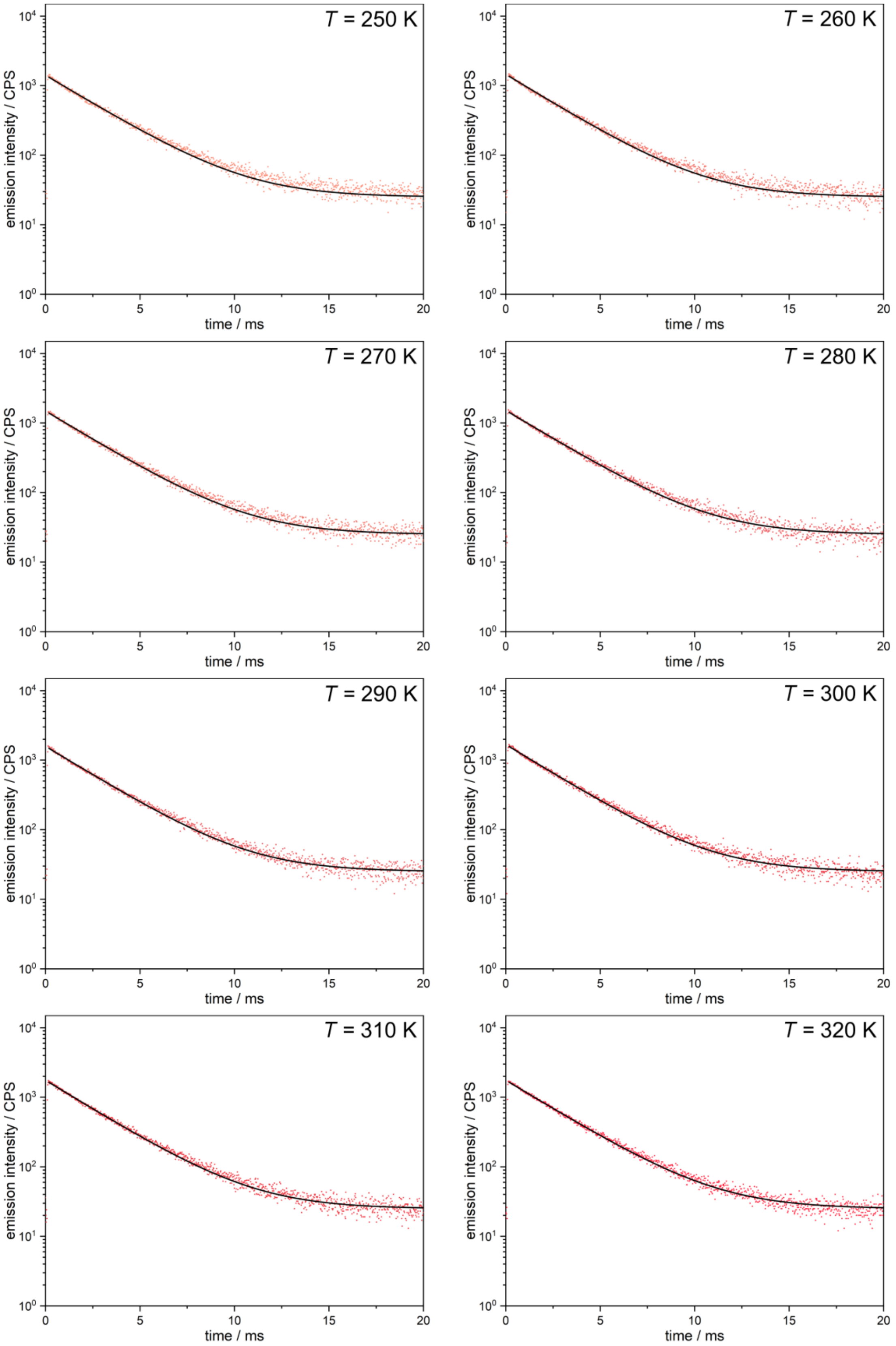

Fig. S43 Temperature-variable emission decay profiles for **Yb@EuAg**, gathered in the 250–320 K temperature range for λ_{exc} = 275 nm and λ_{em} = 617 nm. The experimental data were fitted using the mono-exponential decay function. The best-fit parameters are gathered in Table S27.

Table S25 Best-fit parameters to the mono-exponential decay function for the temperature-variable emission decay profiles of **EuAg** (λ_{exc} = 275 nm and λ_{em} = 617 nm).

Temperature / K	τ_1 / ms	χ^2
10	2.644(3)	0.99921
20	2.630(3)	0.99917
30	2.624(3)	0.99908
40	2.626(3)	0.99902
50	2.612(4)	0.9989
60	2.577(4)	0.99848
70	2.537(5)	0.99802
80	2.505(5)	0.99753
90	2.489(5)	0.99732
100	2.496(5)	0.99724
110	2.479(5)	0.99753
120	2.467(5)	0.99723
130	2.498(5)	0.99753
140	2.503(5)	0.99759
150	2.516(5)	0.99783
160	2.550(5)	0.99815
170	2.541(5)	0.99802
180	2.528(5)	0.99799
190	2.552(5)	0.99821
200	2.531(5)	0.9979
210	2.537(5)	0.99805
220	2.533(5)	0.99778
230	2.539(5)	0.99816
240	2.524(4)	0.99834
250	2.519(4)	0.99849
260	2.518(4)	0.99862
270	2.520(4)	0.99839
280	2.518(4)	0.99862
290	2.526(4)	0.99856
300	2.520(4)	0.99866
310	2.534(4)	0.99863
320	2.537(4)	0.99868

Table S26 Best-fit parameters to the mono-exponential decay function for the temperature-variable emission decay profiles of **Er@EuAg** (λ_{exc} = 275 nm and λ_{em} = 618 nm).

Temperature / K	τ_1 / ms	χ^2
10	2.544(3)	0.9993
20	2.521(3)	0.9993
30	2.492(3	0.99925
40	2.486(3)	0.9992
50	2.486(3)	0.99917
60	2.479(4)	0.99862
70	2.458(5)	0.99761
80	2.459(6)	0.99636
90	2.399(7)	0.99507
100	2.397(7)	0.99507
110	2.398(7)	0.99558
120	2.398(7)	0.99549
130	2.424(7)	0.99555
140	2.427(7)	0.99577
150	2.447(7)	0.99577
160	2.468(7)	0.99576
170	2.438(6)	0.996
180	2.465(7)	0.99566
190	2.444(7)	0.99596
200	2.477(7)	0.9948
210	2.471(7)	0.99511
220	2.456(7)	0.99482
230	2.475(7)	0.99522
240	2.464(7)	0.9955
250	2.470(7)	0.99581
260	2.455(7)	0.99562
270	2.475(7)	0.99533
280	2.465(7)	0.99575
290	2.471(7)	0.99565
300	2.481(7)	0.99547
310	2.450(7)	0.99558
320	2.449(7)	0.99588

Table S27 Best-fit parameters to the mono-exponential decay function for the temperature-variable emission decay profiles of **Yb@EuAg** (λ_{exc} = 275 nm and λ_{em} = 617 nm).

Temperature / K	τ_1 / ms	χ^2
10	2.740(3)	0.99932
20	2.724(3)	0.9993
30	2.709(3)	0.99918
40	2.701(3)	0.99911
50	2.685(4)	0.99902
60	2.665(4)	0.99848
70	2.623(5)	0.99752
80	2.586(7)	0.99625
90	2.561(7)	0.99554
100	2.582(7)	0.9955
110	2.589(7)	0.9958
120	2.641(7)	0.99602
130	2.658(7)	0.99587
140	2.674(7)	0.99573
150	2.673(8)	0.99538
160	2.689(8)	0.99445
170	2.700(8)	0.99451
180	2.705(8)	0.99419
190	2.725(8)	0.9943
200	2.731(8)	0.99453
210	2.682(8)	0.99496
220	2.683(7)	0.99565
230	2.666(7)	0.99644
240	2.655(7)	0.99661
250	2.638(7)	0.99649
260	2.594(6)	0.99703
270	2.622(6)	0.99727
280	2.635(5)	0.99773
290	2.601(5)	0.99763
300	2.584(6)	0.9974
310	2.591(5)	0.99791
320	2.624(5)	0.99825

Table S28 Absolute quantum yields of **EuAg**, **Er@EuAg**, and **Yb@EuAg**, collected at room temperature in the solid state, under the indicated excitation wavelength.

Compound	λ_{exc} / nm	Quantum yield (Φ)[S7]
EuAg	275	55.36%
Er@EuAg		54.48%
Yb@EuAg		54.12%

Comment to Fig. S44 and S45, as well as Table S29

In Fig. S44 and S45, and further in Table S29, the results of the alternative fitting procedures for the field- and temperature-dependences of the magnetic relaxation times in **ErAg** and **Er@EuAg** are presented. As it was presented and discussed in the main text of the article (Fig. 2 and Table 1), for the indicated pair of **ErAg** and **Er@EuAg**, we found that the most reliable, as well as the most consistent between the undiluted sample and the diluted one, best-fit curves and the related best-fit parameters are achievable when taking into account three relaxation pathways represented by Equation 2, i.e., Direct, QTM, and Orbach processes.

In general, four relaxation processes were considered to contribute to the overall magnetic relaxation in the reported compounds. They are represented by Equation S5:

$$\tau_{\mathrm{M}}^{-1} = \frac{a}{(1+bH^2)} + AH^mT + \tau_0 exp\left(\frac{-\Delta E}{k_B T}\right) + BT^n \qquad \text{(S5)}$$

where the first term corresponds to the quantum tunneling of magnetization (QTM), depicted by two parameters (*a* and *b*), the second represents the Direct process, the third parameterizes the Orbach relaxation pathway, while the last represents the Raman relaxation.[S9] In the approach presented in the main article (Fig. 2 and Table 1, shown also for the reference in Fig. S44 and S45, as well as Table S29, with the marking "main"), to avoid overparameterization, we used the set of three relaxation processes, excluding the Raman process, as well as we used the fixed value of the energy barrier related to the Orbach process, which was taken from the results of the *ab initio* calculations (i.e., the energy barrier was assigned to be the energy of the first excited m_J level, through which the Orbach relaxation is likely to occur due to its highly mixed m_J character, Table S12). Thanks to this strategy, we obtained the rational set of the fitting results for the pair of **ErAg** and **Er@EuAg**. First, we could obtain a good quality fitting using the analogous set of relaxation processes for both these compounds, differing only in the variable values of free parameters, as expected for the magnetic dilution effect. Moreover, the obtained trends of changes in the parameters seem to be rational, as the QTM contribution decreases with the magnetic dilution, which is an expected effect, being responsible for the overall enhancement of slow magnetic relaxation effects for the lanthanide(III)-based SMMs upon magnetic dilution due to the related cancellation of the unbeneficial dipolar interactions. Simultaneously, the other two processes, Orbach and Direct, are only subtly affected by the dilution, which is not surprising, as the related changes in the coordination sphere of magnetic centers are small, leading to rather subtle changes in the energy splitting of the m_J levels. Taking the above into account, we decided to use the indicated set of three relaxation processes (Direct, Orbach, QTM) in the analysis of the *ac* magnetic data of **ErAg** and **Er@EuAg**.

However, one can be surprised by this selection of relaxation processes in the description of the SMM features of **ErAg** and **Er@EuAg**, knowing that the Raman relaxation is usually more pronounced than the Orbach one for the SMMs showing the relaxation processes operating at such low temperatures. Thus, to further rationalize our approach, it is necessary to discuss the results of the additional fitting procedures, which were tested, attempting to exclude the Orbach relaxation (i.e., use the Raman process instead) or use it along with the Raman process.

In this context, using the combination of Direct, QTM, and Raman processes, it was possible to reach the reliable best-fit curves and parameters for **ErAg** (Fig. S44, Table S29), for which the resulting power "n" of the Raman relaxation was found to be 8.04(54), staying in the expected range of 2–9. At the same time, the parameters for QTM and Direct processes remain at reasonable levels. Thus, it can be concluded that this alternative fit, with the Raman relaxation instead of the Orbach one, can be considered as a reasonable alternative to the one presented in the main article (Fig. 2 and S44). However, the analogous procedure was found to be unsuccessful for the magnetically diluted compound of **Er@EuAg**, as it resulted in the Raman process described by the unphysical power "n" reaching 13, far outside the limit of 9. This strongly suggests that the Orbach relaxation has to be taken into account, especially since the QTM effect is distinctly quenched upon magnetic dilution, leading to the more reliable demonstration of the influence of either Raman or Orbach processes in the crucial temperature dependence of relaxation times in **Er@EuAg**. Therefore, it appears more reliable to use the original set of Orbach, Direct, and QTM processes for both compounds, while presenting the fitting procedure with the Orbach process exchanged with the Raman process as an alternative, working well only for the undiluted sample (Fig. S44). This approach also ensures a more consistent comparison of the parameters of QTM and Direct processes between these two compounds (Fig. 2 and Table 1).

As mentioned above, it was not possible to exclude the Orbach process for the case of the diluted compound of **Er@EuAg** and use the Raman process instead. However, it was found achievable to use the full set of four relaxation processes, i.e., Raman, Orbach with the fixed energy barrier from the *ab initio* studies (without this, the fitting results are unreliable), Direct, and QTM. The resulting best-fit curves are of good quality (Fig. S45), and the best-fit parameters seem reasonable (Table S29). However, the QTM contribution is affected due to the necessity to include the role of an additional process. Moreover, the Raman contribution becomes much less important in the description of the overall magnetic relaxation than the Orbach process. Last but not least, such an approach with four relaxation processes raised the issue of the accuracy of the obtained parameters due to the possible overparameterization. It seems that, for the diluted compound with the relatively high number of experimental points, the obtained set of parameters can be considered as relatively reliable, but this data treatment was not possible in the case of the undiluted sample, for which the number of accessible experimental points is much lower, making the related fit unreliable due to the overparameterization. Therefore, again, to ensure the consistent comparison between the compounds, it appears more reasonable to focus on the original set of three relaxation processes of QTM, Direct, and Orbach (thus, such the treatment is presented in the main article, Fig. 2 and Table 1), while mentioning the Raman process as the additional process that might operate, but (1) is not of primary importance as the QTM effect governs the relaxation in **ErAg**, while the Orbach relaxation dominates the relaxation in **Er@EuAg** due to the cancelling of the QTM, (2) cannot be reliably determined without affecting the consistency of the results due to the overparameterization issue, especially for the case of **ErAg** showing the limited number of experimental points that are accessible for fitting.

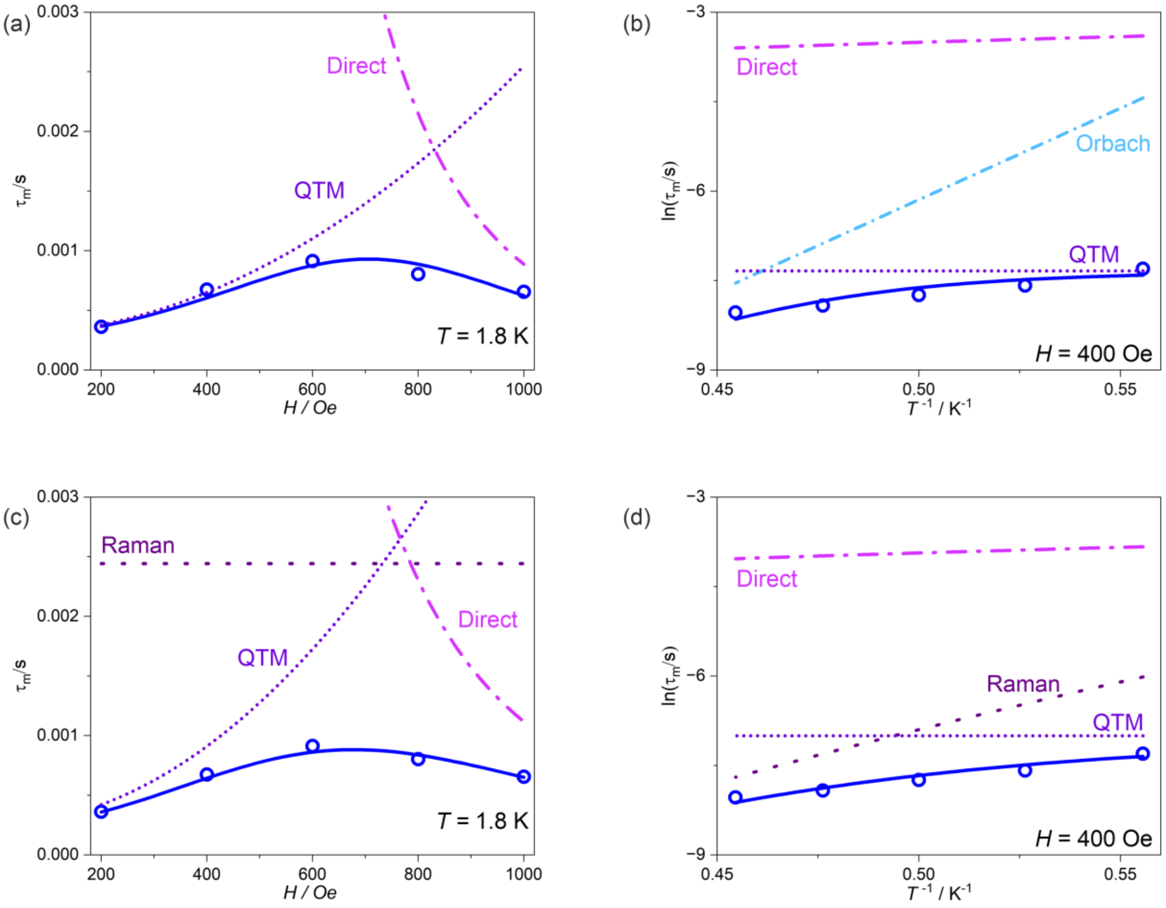

Fig. S44 Comparison of the field-dependences (a, c) and temperature-dependences (b, d) of relaxation times, τ_m of **ErAg**, with the course of individual relaxation processes for the three-dimensional fitting of the *H*- and *T*-dependences of relaxation time, taking into account the combination of Direct, QTM, and Orbach processes (a, b, denoted as **ErAg**$^{\text{main}}$ in Table S29), or the combination of Direct, QTM, and Raman processes (c, d, denoted as **ErAg**$^{\text{alternative}}$ in Table S29). The blue solid lines show the best fits taking into account the sums of the indicated relaxation processes, while the dashed colored lines represent the respective courses of the contributions from the indicated magnetic relaxation processes. Comparison of the resulting best-fit parameters is shown in Table S29.

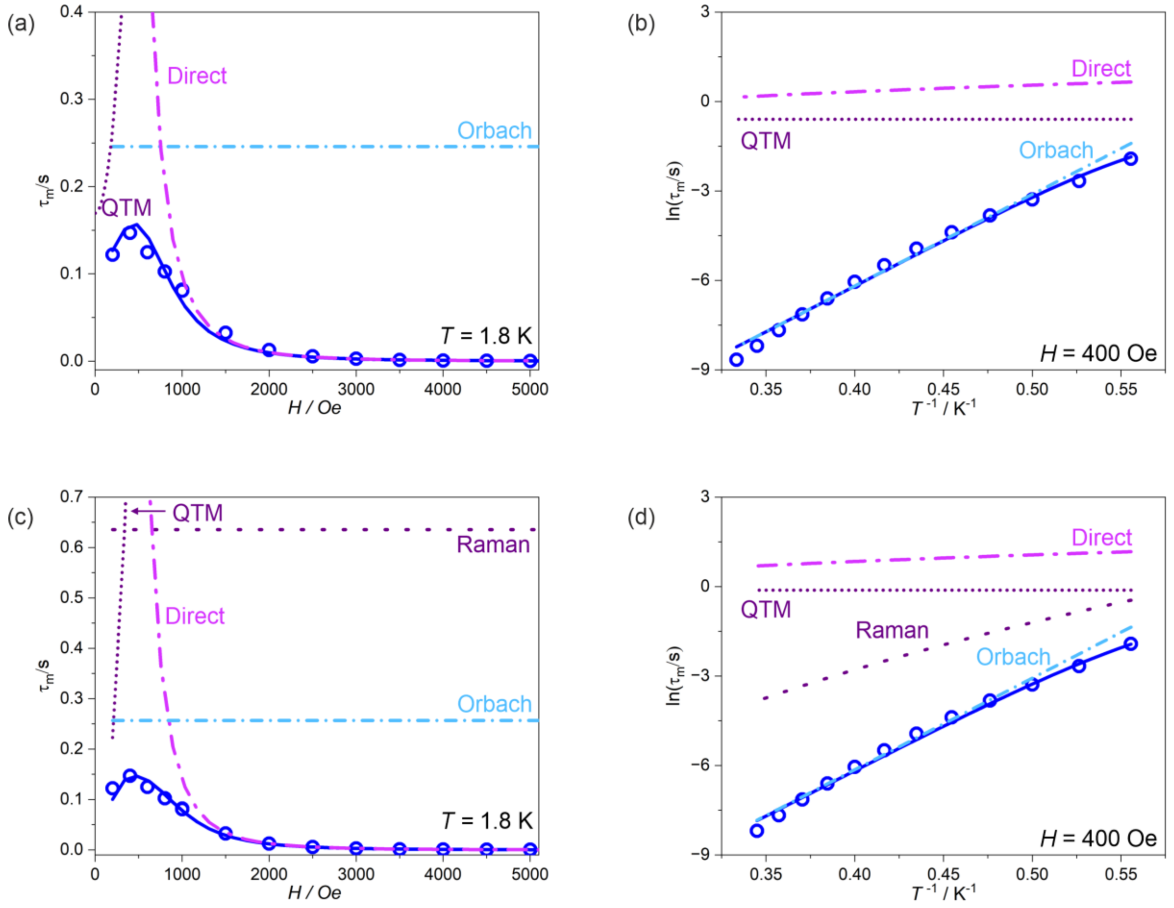

Fig. S45 Comparison of the field-dependences (a, c) and temperature-dependences (b, d) of relaxation times, τ_m of **Er@EuAg**, with the course of individual relaxation processes for the three-dimensional fitting of the *H*- and *T*-dependences of relaxation time, taking into account the combination of Direct, QTM, and Orbach processes (a, b, denoted as **Er@EuAg**$^{\text{main}}$ in Table S29), or the combination of Direct, QTM, Orbach, and Raman processes (c, d, denoted as **Er@EuAg**$^{\text{alternative}}$ in Table S29). The blue solid lines show the best fits taking into account the sums of the indicated relaxation processes, while the dashed colored lines represent the respective courses of the contributions from the indicated magnetic relaxation processes. Comparison of the resulting best-fit parameters is shown in Table S29.

Table S29 The comparison of the best-fit parameters of slow magnetic relaxation processes for **ErAg** and **Er@EuAg**, obtained within the three-dimensional simultaneous fitting procedures of the field dependencies at T = 1.8 K and the temperature dependencies at the optimal *dc* fields (Fig. S14, S15, S18, S19), taking into account the different sets of magnetic relaxation processes (see Fig. S44 and S45, and the related comment above for more details).

Compound	**ErAg**$^{\mathrm{main}}$	**ErAg**$^{\mathrm{alternative}}$	**Er@EuAg**$^{\mathrm{main}}$	**Er@EuAg**$^{\mathrm{alternative}}$
A / s^{-1} K^{-1} Oe^{-m}	8.3(6)·10^{-10}	5.68(3)·10^{-8}	8.9(3)·10^{-10}	2.0(2)·10^{-10}
m	3.96(3)	3.31(12)	3.27(5)	3.43(1)
a / s^{-1}	3468(731)	4384(1797)	5.89(3)	8607(4)
b / Oe^{-2}	7.8(8)·10^{-5}	2.0(2)·10^{-5}	1.4(9)·10^{-5}	0.05(3)
B / s^{-1} K^{-n}	-	3.99(17)	-	0.02(10)
n	-	8.04(54)	-	7.09(70)
τ_0 / s	2.18(3)·10^{-9}	-	1.05(6)·10^{-8}	1.02(4)·10^{-8}
ΔE / cm^{-1}	30.716 (*ab initio*)	-	30.716 (*ab initio*)	30.716 (*ab initio*)

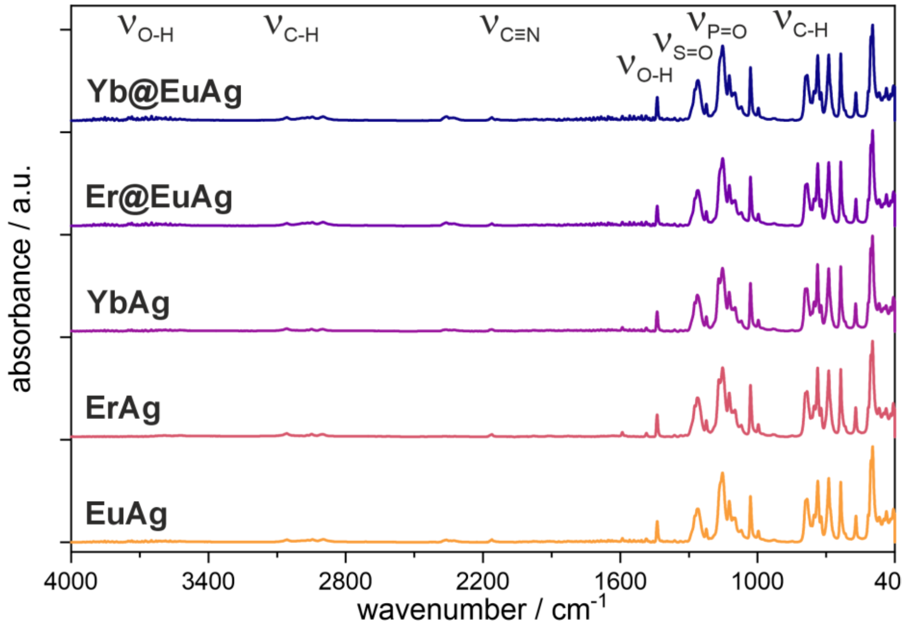

Fig. S46 Infrared (IR) absorption spectra of the polycrystalline powder samples of **EuAg**, **ErAg**, **YbAg**, **Er@EuAg**, and **Yb@EuAg** presented in the 4000–400 cm^{-1} range (ATR-FTIR spectra, see Experimental section for details).

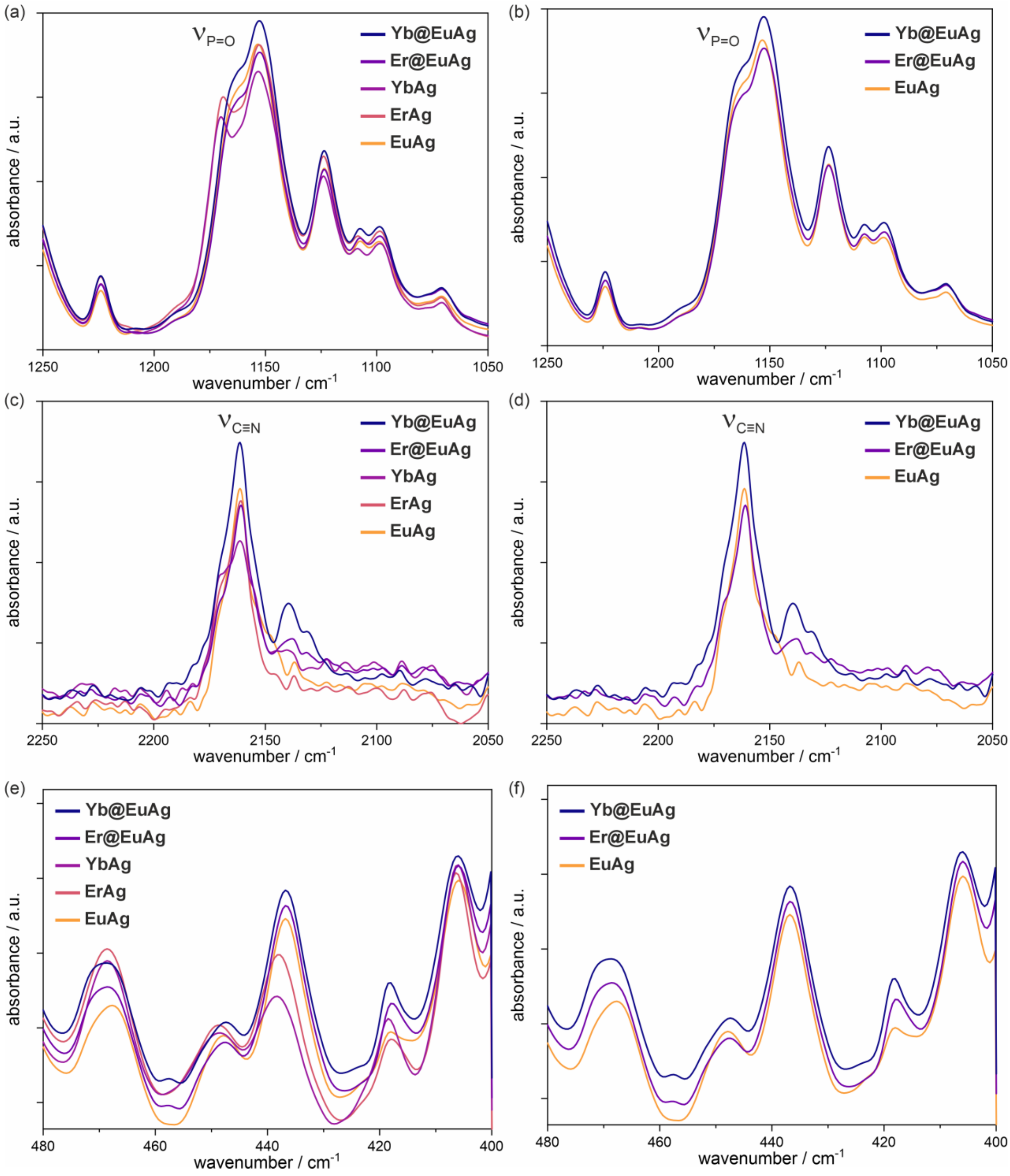

Fig. S47 Comparison of the infrared (IR) absorption spectra of the polycrystalline powder samples of **EuAg**, **ErAg**, **YbAg**, **Er@EuAg**, and **Yb@EuAg** (a, c, e) and direct comparison of the related IR spectra of **EuAg**, **Er@EuAg**, and **Yb@EuAg** (b, d, f), presented in the 1250–1050 cm^{-1} range containing characteristic stretching modes of P=O coordinated ligands (a, b), in the 2250–2050 cm^{-1} range containing characteristic stretching modes of bridging cyanido ligands (c, d),[S2] and in the 480–400 cm^{-1} range containing fingerprint of vibrational modes of lanthanide(3+) ions with the donor atoms of the coordinated ligands (d, e) (ATR-FTIR spectra, see Experimental section for details).

Comment to Fig. S48–S55 and Tables S30–S32:

To examine the efficiency of the Eu(III)-based dilution in improving the magnetic properties of Er(III) and Yb(III) centers in the reported compounds, and to check the eventual contributions of not purely diamagnetic Eu(III) centers to overall magnetic relaxation processes of **Er@EuAg** and **Yb@EuAg**, we decided to compare the obtained mentioned compounds with their Y(III)-based analogs, named **Er@YAg** and **Yb@YAg**, respectively. Thus, following the general procedure (see Experimental section for details), we synthesized the Y(III)-based mixed-lanthanide analogs, as a result obtaining **Er@YAg** of the composition of $\{[\mathrm{Y^{III}}_{0.94}\mathrm{Er^{III}}_{0.06}(\mathrm{dppmO_2})_3][\mathrm{Ag^I(CN)_2}]\}[\mathrm{OTf}]_2$ and **Yb@YAg** of the composition of $\{[\mathrm{Y^{III}}_{0.95}\mathrm{Yb^{III}}_{0.05}(\mathrm{dppmO_2})_3][\mathrm{Ag^I(CN)_2}]\}[\mathrm{OTf}]$. Their crystal structure and phase purity were confirmed by powder X-ray diffraction (P-XRD) performed at room temperature, comparing their experimental diffractograms with those calculated from the structural models of **YbAg** and **ErAg**, determined within the single-crystal X-ray diffraction (SC-XRD) structural analysis performed at 100 K (Fig. S48). The exact metal ratio between lanthanide centers was determined by the SEM-EDX metal analysis (Fig. S49 and S50, Tables S30 and S31). After this basic physicochemical and structural characterization, the polycrystalline samples of **Er@YAg** and **Yb@YAg** were investigated from the viewpoint of SMM characteristics by means of *ac* magnetic measurements. The related results are gathered in Fig. S51–S54. They were analyzed and fitted in the completely analogous manner as done for the Eu(III)-containing analogs. The resulting best-fit parameters and curves of the Y(III)-based compounds, compared with those containing the Eu(III) for magnetic dilution, are presented in Fig. S55 and Table S32. The thorough discussion on these properties is placed in the main article. Below, the description of the syntheses of **Er@YAg** and **Yb@YAg** is additionally presented.

Synthesis of Er@YAg

Er@YAg was synthesized using a modified general procedure, taking the proper mixture of $\mathrm{Er^{III}(OTf)_3}$ (4.9 mg, 0.008 mmol, 0.1 eq.) and $\mathrm{Y^{III}(OTf)_3}$ (38.6 mg, 0.072 mmol, 0.9 eq.), which gives the 9:1 molar ratio for trivalent metal ions. This results in colorless crystals with a 38% yield. Their structure, phase purity, and air stability were confirmed by P-XRD method (Fig. S48), while exact metal composition was determined by the SEM-EDX measurements (Table S30): $\{[\mathrm{Y^{III}}_{0.94}\mathrm{Er^{III}}_{0.06}(\mathrm{dppmO_2})_3][\mathrm{Ag^I(CN)_2}]\}[\mathrm{OTf}]_2$ (M_W = 1800.83 g·mol^{-1}).

Synthesis of Yb@YAg

Yb@YAg was synthesized using a modified general procedure, taking the proper mixture of $\mathrm{Yb^{III}(OTf)_3}$ (5.0 mg, 0.008 mmol, 0.1 eq.) and $\mathrm{Y^{III}(OTf)_3}$ (38.6 mg, 0.072 mmol, 0.9 eq.), which gives the 9:1 molar ratio for trivalent metal ions. This results in colorless crystals with a 42% yield. Their structure, phase purity, and air stability were confirmed by P-XRD method (Fig. S48), while exact metal composition was determined by the SEM-EDX measurements (Table S31): $\{[\mathrm{Y^{III}}_{0.95}\mathrm{Yb^{III}}_{0.05}(\mathrm{dppmO_2})_3][\mathrm{Ag^I(CN)_2}]\}[\mathrm{OTf}]_2$ (M_W = 1800.33 g·mol^{-1}).

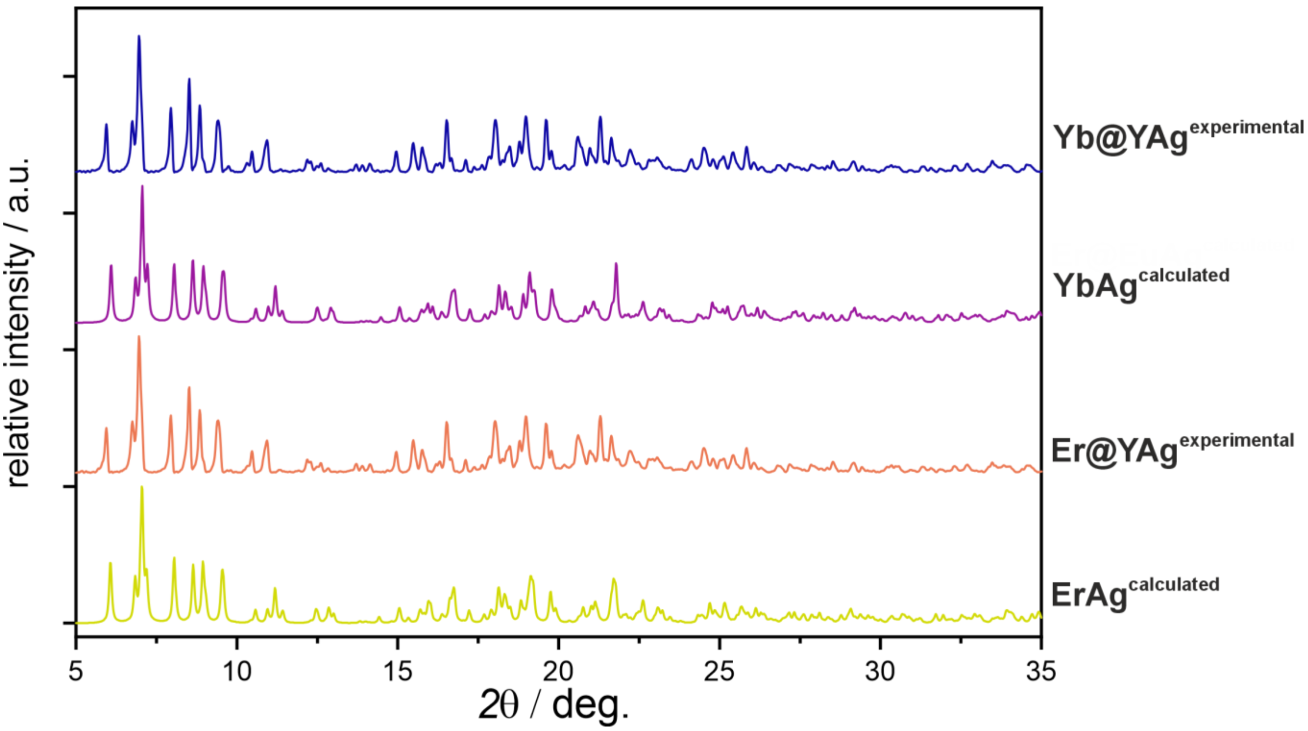

Fig. S48 Comparison of experimental (room temperature) P-XRD patterns of **Er@YAg** and **Yb@Yag** with the calculated ones for **ErAg** and **YbAg**, presented in the selected 5–35° range of the 2*Θ* angle. The calculated P-XRD patterns were obtained from the structural model determined within the single-crystal X-ray diffraction (SC-XRD) structural analysis (*T* = 100(2) K).

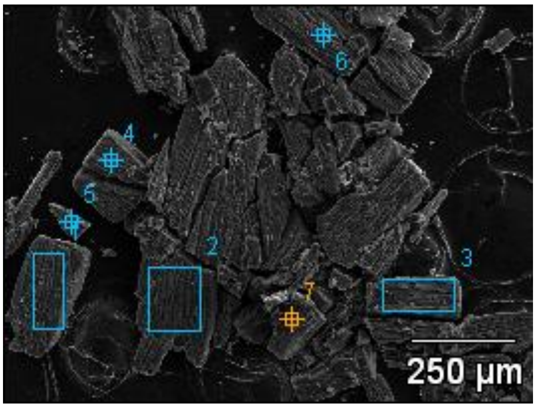

Fig. S49 The SEM image of the polycrystalline ground sample of **Er@YAg** with the indication of the areas 1–3 and points 4–7 targeted for the EDX microanalysis. The related results of the analysis are gathered in Table S30.

Table S30 Results of the SEM-EDX microanalysis of the lanthanides(III) composition in **Er@YAg** (see Fig. S49 for comparison).

Metal	$\mathrm{Er^{III}}$	$\mathrm{Y^{III}}$
measured atomic composition (only metals(III) included) / %	0.50(14)	8.69(45)
	0.60(18)	9.98(54)
	0.45(13)	7.99(43)
	0.58(19)	9.26(53)
	0.67(10)	11.04(42)
	0.45(13)	8.76(38)
	0.74(13)	9.95(32)
	0.55(13)	8.38(34)
	0.56(22)	8.93(50)
relative atomic composition (calculated for 1 $\mathrm{M^{III}}$ center)	0.06(7)	0.94(3)
proposed metal composition	0.06	0.94

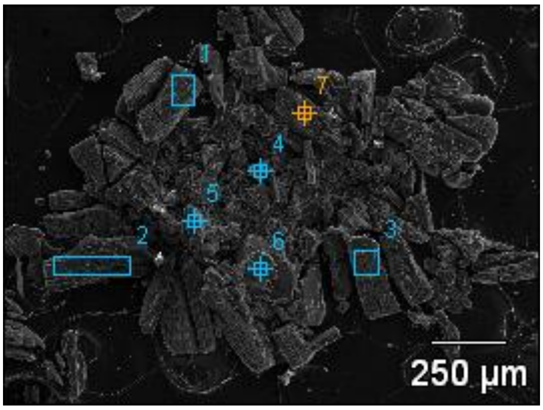

Fig. S50 The SEM image of the polycrystalline ground sample of **Yb@YAg** with the indication of the areas 1–3 and points 4–7 targeted for the EDX microanalysis. The related results of the analysis are gathered in Table S31.

Table S31 Results of the SEM-EDX microanalysis of the lanthanides(III) composition in **Yb@YAg** (see Fig. S50 for comparison).

Metal	$\mathrm{Yb^{III}}$	$\mathrm{Y^{III}}$
measured atomic composition (only metals(III) included) / %	0.61(14)	9.43(41)
	0.42(14)	10.02(36)
	0.52(16)	9.53(46)
	0.58(12)	8.89(38)
	0.67(17)	10.85(40)
	0.42(12)	10.50(31)
	0.65(18)	10.07(46)
	0.44(11)	7.31(106)
	0.54(12)	9.14(39)
relative atomic composition (calculated for 1 $\mathrm{M^{III}}$ center)	0.05(8)	0.95(2)
proposed metal composition	0.05	0.95

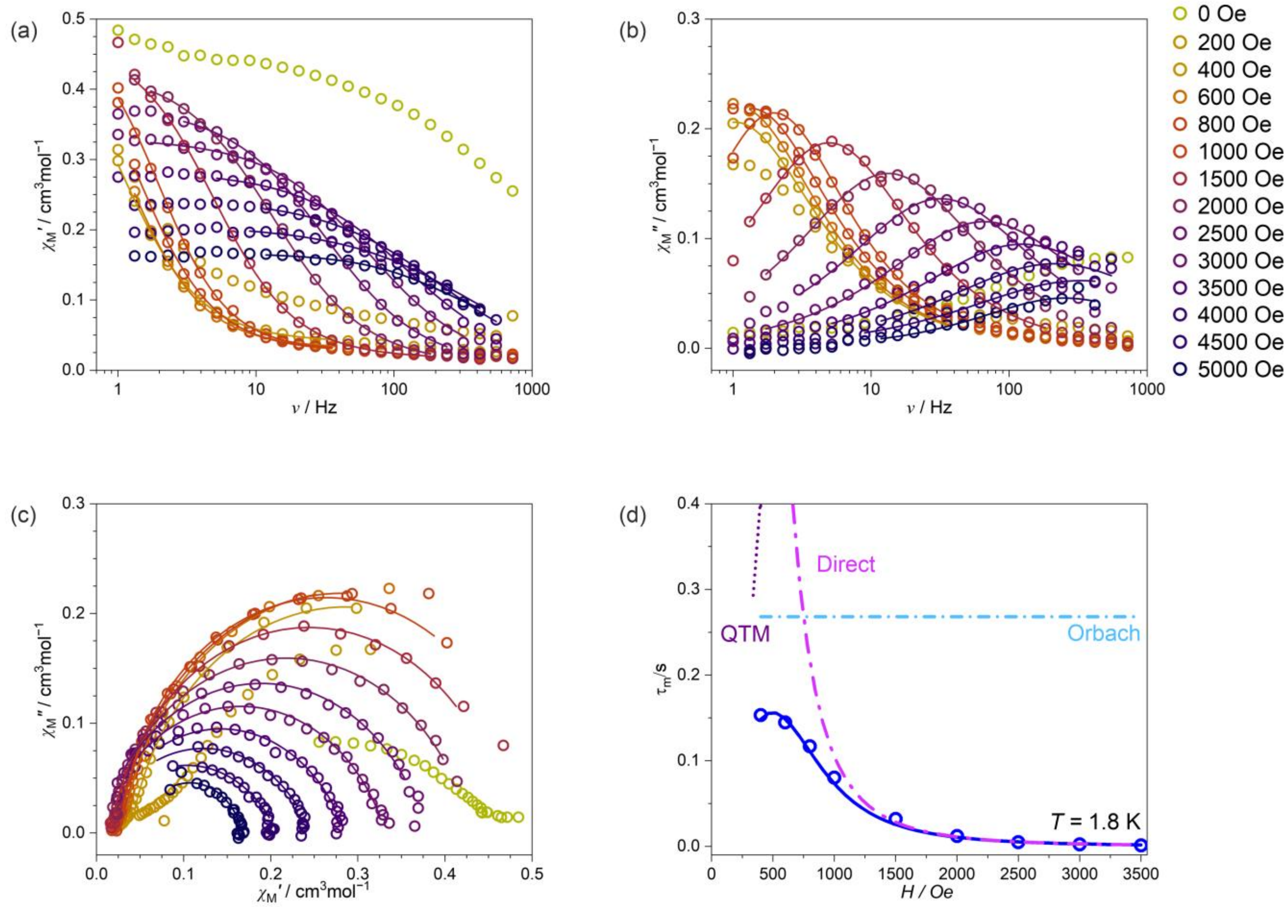

Fig. S51 Magnetic-field-variable alternate-current (*ac*) magnetic characteristics for **Er@YAg** at T = 1.8 K, including the frequency dependences of the in-phase susceptibility, χ_M', (a) and the out-of-phase susceptibility, χ_M'', (b) under variable indicated *dc* fields, the related Argand plots (c), and the field dependence of the resulting relaxation time, τ_m (d). Colored solid lines in (a–c) represent the best fits using the generalized Debye model for a single relaxation process. The blue solid line in (d) shows the best fit taking into account the indicated relaxation processes, while the dashed colored lines represent the respective course of individual magnetic relaxation processes. The results in (d) were obtained within a simultaneous fit of both temperature- and field-variable data (this figure and Fig. S52). Best-fit parameters for the (d) part are gathered in Table S32.

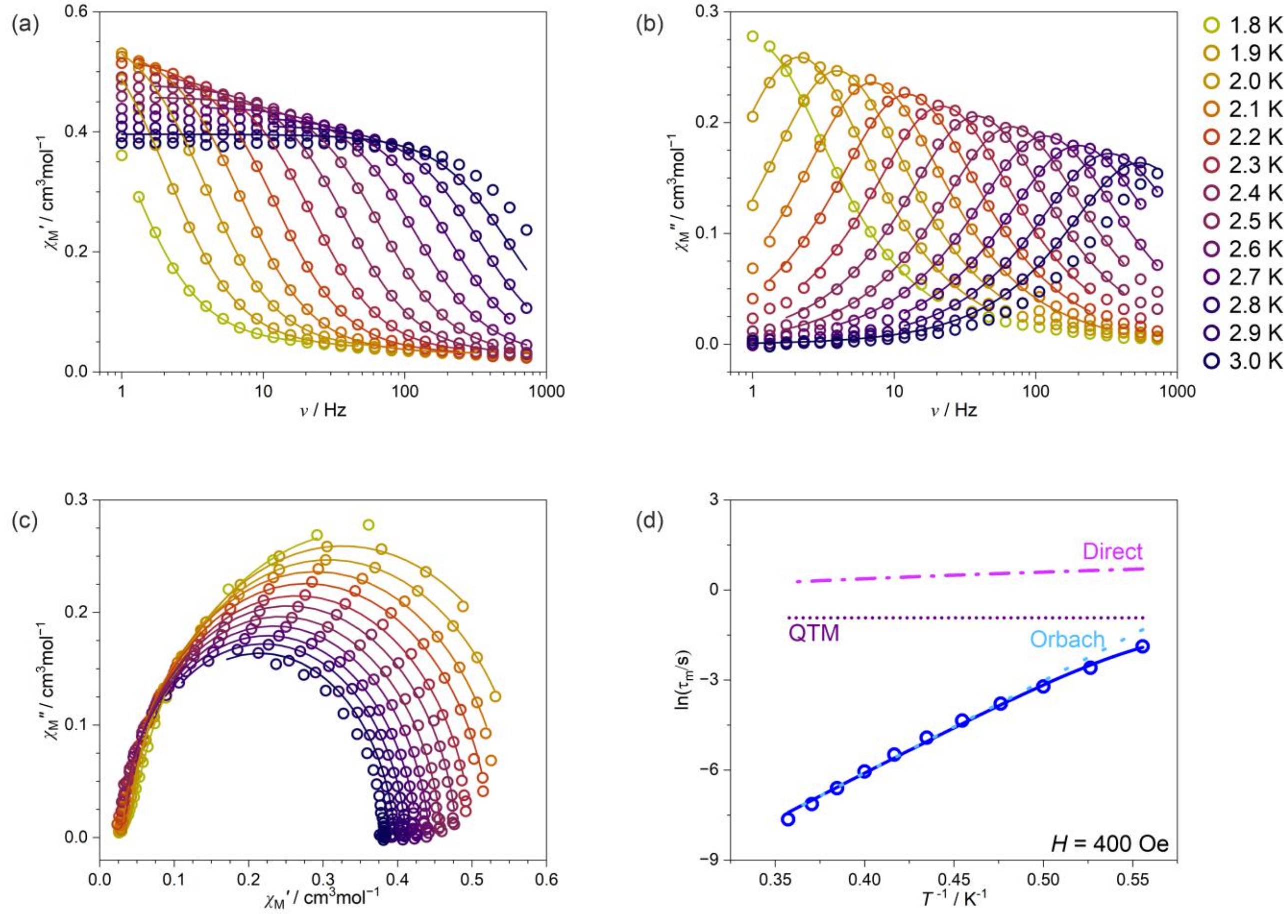

Fig. S52 Temperature-variable alternate-current (*ac*) magnetic characteristics for **Er@YAg** at H_{dc} = 400 Oe, including the frequency dependences of the in-phase susceptibility, χ_M', (a) and the out-of-phase susceptibility, χ_M'', (b) under variable indicated *dc* fields, the related Argand plots (c), and the temperature dependence of the resulting relaxation time, τ_m (d). Colored solid lines in (a–c) represent the best fits using the generalized Debye model for a single relaxation process. The blue solid line in (d) shows the best fit taking into account the indicated relaxation processes, while the dashed colored lines represent the respective course of individual magnetic relaxation processes. The results in (d) were obtained within a simultaneous fit of both temperature- and field-variable data (this figure and Fig. S51). Best-fit parameters for the (d) part are gathered in Table S32.

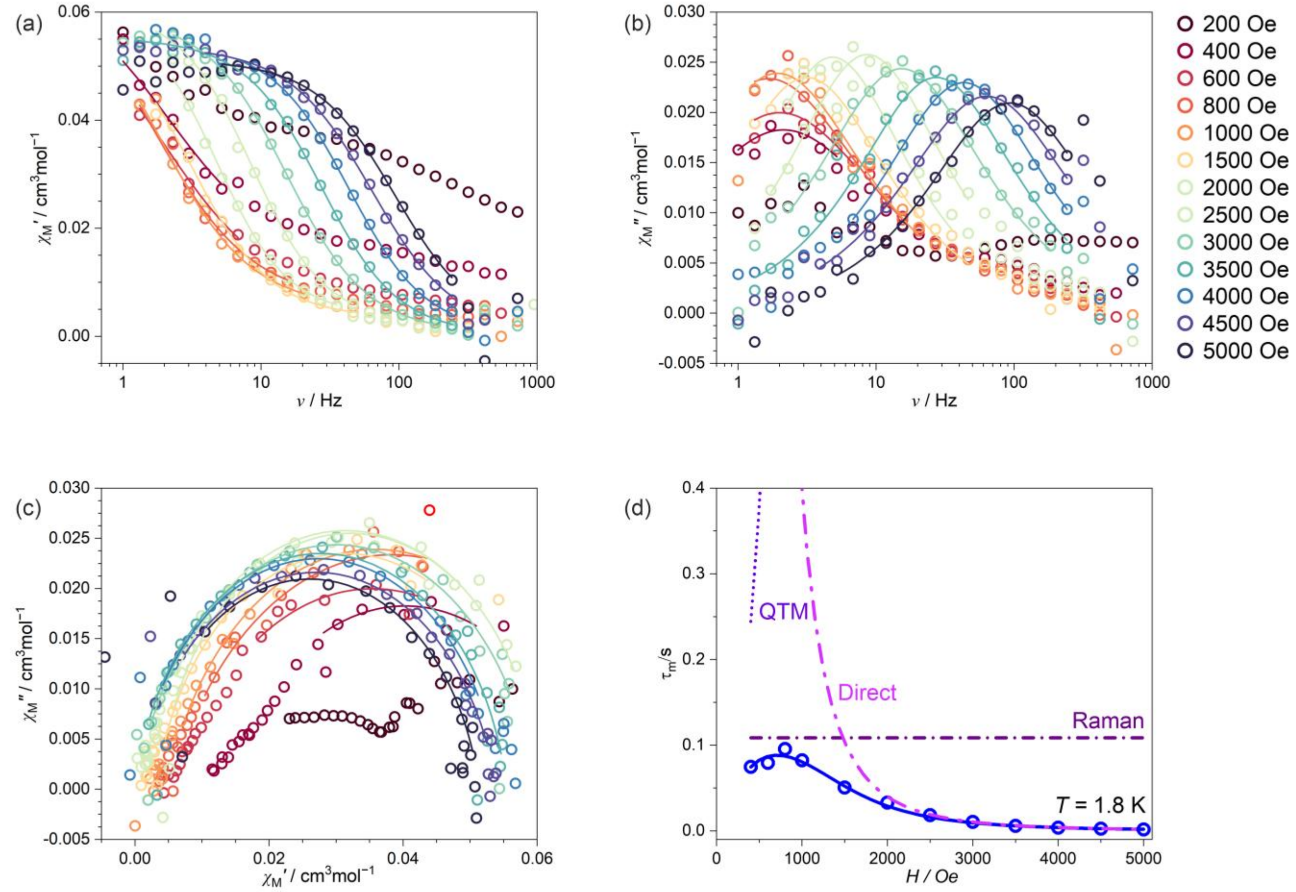

Fig. S53 Magnetic-field-variable alternate-current (*ac*) magnetic characteristics for **Yb@YAg** at T = 1.8 K, including the frequency dependences of the in-phase susceptibility, χ_M', (a) and the out-of-phase susceptibility, χ_M'', (b) under variable indicated *dc* fields, the related Argand plots (c), and the field dependence of the resulting relaxation time, τ_m (d). Colored solid lines in (a–c) represent the best fits using the generalized Debye model for a single relaxation process. The blue solid line in (d) shows the best fit taking into account the indicated relaxation processes, while the dashed colored lines represent the respective course of individual magnetic relaxation processes. The results in (d) were obtained within a simultaneous fit of both temperature- and field-variable data (this figure and Fig. S54). Best-fit parameters for the (d) part are gathered in Table S32.

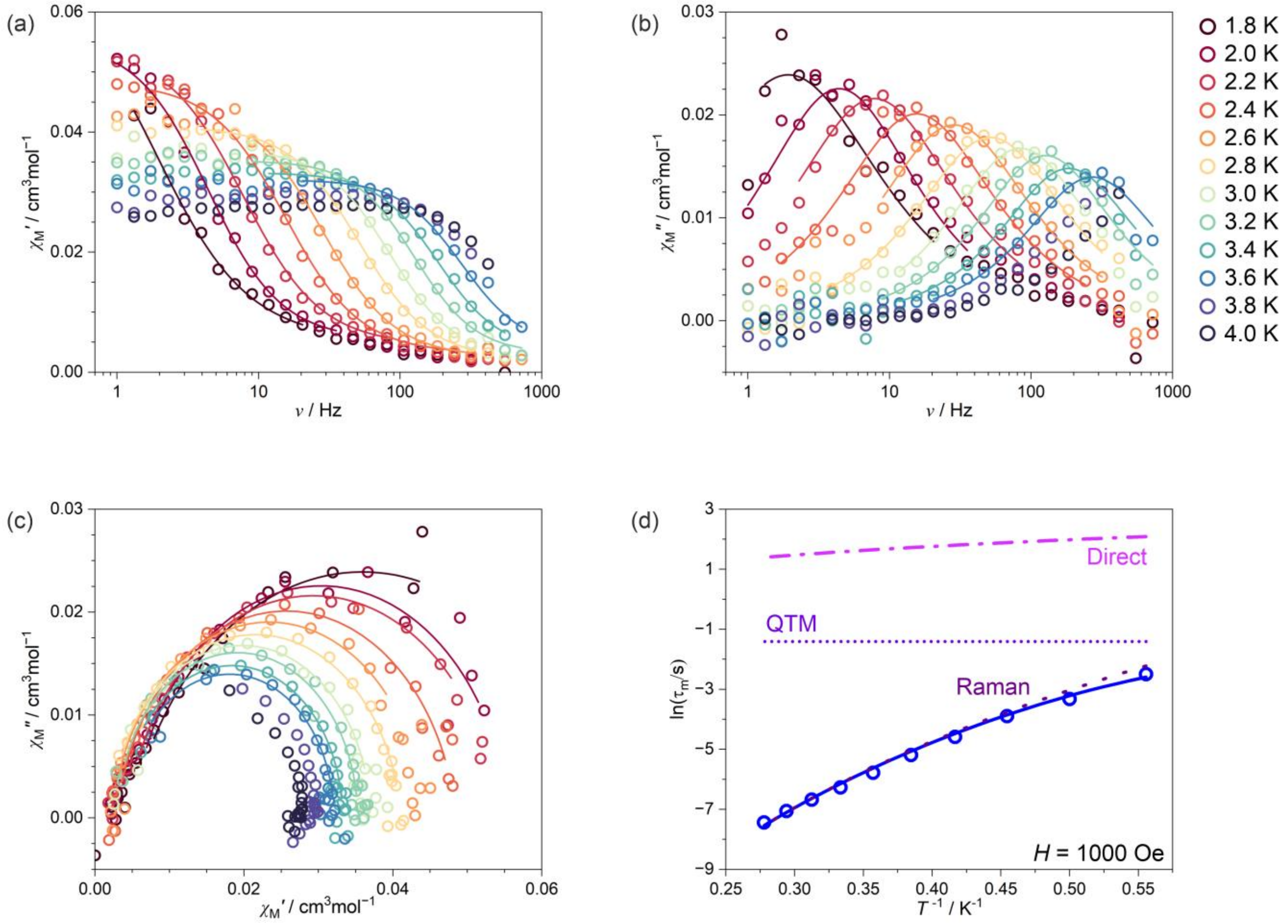

Fig. S54 Temperature-variable alternate-current (*ac*) magnetic characteristics for **Yb@YAg** at H_{dc} = 1 kOe, including the frequency dependences of the in-phase susceptibility, χ_M', (a) and the out-of-phase susceptibility, χ_M'', (b) under variable indicated *dc* fields, the related Argand plots (c), and the temperature dependence of the resulting relaxation time, τ_m (d). Colored solid lines in (a–c) represent the best fits using the generalized Debye model for a single relaxation process. The blue solid line in (d) shows the best fit taking into account the indicated relaxation processes, while the dashed colored lines represent the respective course of individual magnetic relaxation processes. The results in (d) were obtained within a simultaneous fit of both temperature- and field-variable data (this figure and Fig. S53). Best-fit parameters for the (d) part are gathered in Table S32.

Table S32 The summary of the best-fit parameters of slow magnetic relaxation processes for **Er@YAg** and **Yb@YAg**, obtained within the three-dimensional simultaneous fitting procedure of the field dependencies at T = 1.8 K and the temperature dependencies at the optimal *dc* fields (Fig. S51–S54),[S9] and their comparison with the best-fit parameters of slow magnetic relaxation processes for **Yb@Ag** and **Er@EuAg** (Fig. S18–S21 Tables 1 and S11). For the related equations and detailed discussion, see the main text and the comment to Fig. S48–S55 and Tables S30–S32 above.

Compound	**Er@YAg**	**Er@EuAg**	**Yb@YAg**	**Yb@EuAg**
A / s^{-1} K^{-1} Oe^{-m}	$1.1(3)\cdot10^{-9}$	$8.9(3)\cdot10^{-10}$	$1.7(2)\cdot10^{-10}$	$1.7(2)\cdot10^{-9}$
m	3.23(1)	3.27(5)	3.3(6)	2.79(1)
a / s^{-1}	35.4(7)	5.89(3)	$6.2(6)\cdot10^{6}$	$4.43(2)\cdot10^{9}$
b / Oe^{-2}	$8.18(2)\cdot10^{-5}$	$1.4(9)\cdot10^{-5}$	9.4(4)	247(31)
B / s^{-1} K^{-n}	0 (fixed)	0 (fixed)	0.10(2)	0.42(12)
n	0 (fixed)	0 (fixed)	7.66(17)	6.78(27)
τ_0 / s	$9.60(7)\cdot10^{-7}$	$1.05(6)\cdot10^{-8}$	0 (fixed)	0 (fixed)
ΔE / cm^{-1}	30.716 (*ab initio*)	30.716 (*ab initio*)	0 (fixed)	0 (fixed)

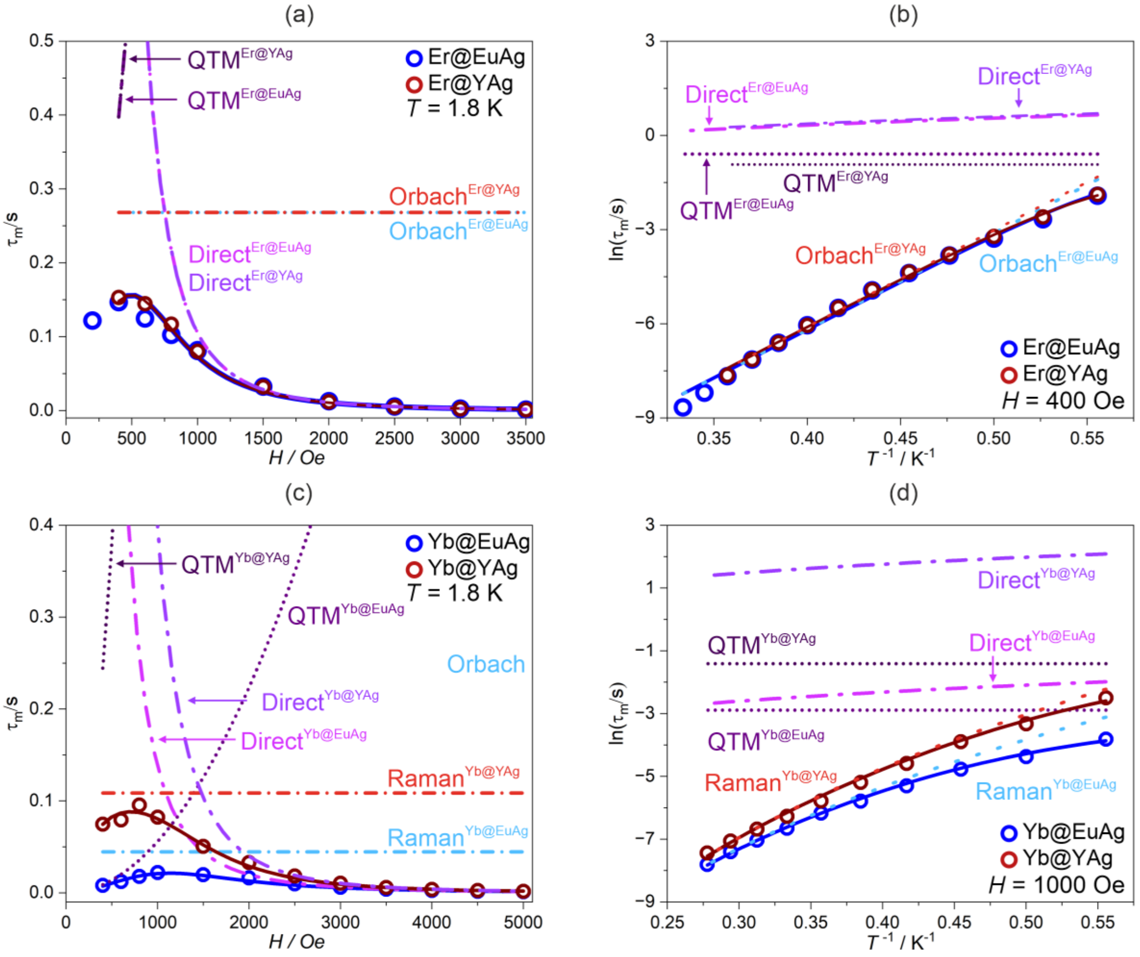

Fig. S55 Comparison of the field-dependences (a, c) and the temperature dependences (b, d) of magnetic relaxation time, τ_m of **Er@EuAg** and **Er@YAg** (a, b), as well as **Yb@EuAg** and **Yb@YAg** (c, d). The solid lines show the best fits taking into account the indicated relaxation processes, while the dashed colored lines represent the respective courses of individual magnetic relaxation processes. The results were obtained within a simultaneous fit of both temperature- and field-variable data. Best-fit parameters for the part are gathered in Table S32.

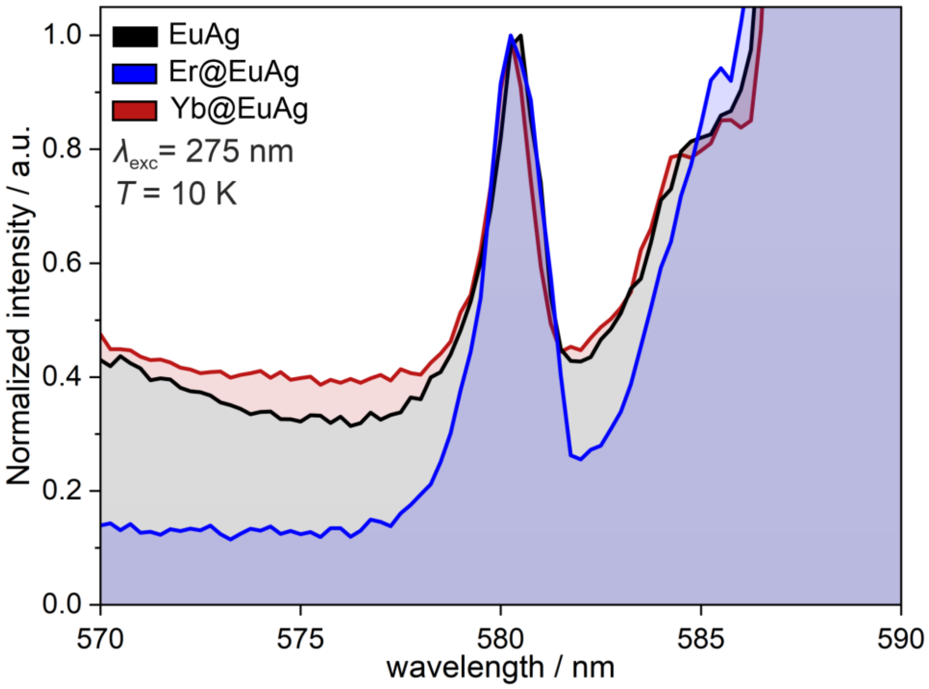

Fig. S56 Comparison of the emission spectra close-up (570–590 nm range) visualizing the band corresponding to the $^5D_0 \rightarrow {}^7F_0$ electronic transition for **EuAg**, **Er@EuAg**, and **Yb@EuAg**, under the excitation of λ_{exc} = 275 nm, gathered at 10 K. Presented spectra are normalized to the lower energy band corresponding to the $^5D_0 \rightarrow {}^7F_4$ electronic transition (not shown here). Note that, due to the character of the presented electronic transition (between two states with J = 0, thus not revealing the crystal-field related energy splitting), a single-band representation is related to the presence of a single crystallographic position of Eu(III) centers in the crystal structure of the indicated compounds. In this context, the addition of Er(III) and Yb(III) dopants seems to induce only subtle structural changes on the Eu(III) centers, as no distinct splitting of the presented band is observed; thus, it can be stated that the dopants do not induce the appearance of the second distinct type of Eu(III) complexes with modulated geometry/bond lengths (then, the second small peak could have been observed). In the alternative scenario, the energy shift of the $^5D_0 \rightarrow {}^7F_0$ could have been observed when the dopants distort the coordination sphere of Eu(III) centers. In this regard, only an extremely small energy shift can be noticed, which suggests that the structural distortion of Eu(III) centers is observed, but is very subtle.

Comment to Table S33 and Fig. S57:

The calculations of experimental Judd-Ofelt (JO) parameters,[S21–S23] Ω_2 and Ω_4, for the **EuAg**, **Er@EuAg**, and **Yb@EuAg** in the 10–310 K range, were performed using the JOES[S21] software based on the experimental emission spectra, without the additional normalization. For these calculations, we took into account the $^5D_0 \rightarrow {}^5F_{1,2,4}$ electronic transitions, using the ratio of the bands' integrated intensity of $^5D_0 \rightarrow {}^5F_{2,4}$ electronic transitions to the band's integrated intensity of $^5D_0 \rightarrow {}^5F_1$ electronic transition (a magnetic dipole reference). The range span for each transition was fixed for all compounds at all selected temperatures (i.e., 585–603 nm for $^5D_0 \rightarrow {}^5F_1$, 609–638 nm for $^5D_0 \rightarrow {}^5F_2$, and 686–712 nm for $^5D_0 \rightarrow {}^5F_4$). The background subtraction was performed in the JOES software, where the background baseline is treated as the minimum of the spectra. The results are gathered in Table S33, visualized in Fig. S57, and discussed in the main article.

Table S33 The experimental Judd-Ofelt (JO) parameters for the **EuAg**, **Er@EuAg**, and **Yb@EuAg** compounds in the 10–310 K range, calculated from the respective emission spectra at the indicated temperatures (Fig. S29).

Compound	Temperature / K	Ω_2 / 10^{-20}cm^{-2}	Ω_4 / 10^{-20}cm^{-2}	Ω_2 / 10^{-20}cm^{-2}	Ω_4 / 10^{-20}cm^{-2}
		Background subtracted		Background non-subtracted	
EuAg	10	3.857	5.596	3.826	5.567
	60	3.761	5.602	3.726	5.567
	110	3.82	5.366	3.774	5.328
	160	4.102	5.218	4.033	5.178
	210	3.964	5.552	3.898	5.495
	260	4.326	5.804	4.238	5.732
	310	4.429	6.476	4.322	6.357
Er@EuAg	10	3.804	5.322	3.791	5.312
	60	3.646	5.191	3.63	5.179
	110	3.827	5.137	3.804	5.123
	160	4.085	5.176	4.053	5.158
	210	4.152	5.1	4.111	5.08
	260	4.281	5.251	4.221	5.219
	310	4.383	5.215	4.326	5.186
Yb@EuAg	10	3.88	5.72	3.855	5.697
	60	3.788	5.731	3.763	5.704
	110	3.882	5.336	3.826	5.294
	160	4.153	5.462	4.091	5.419
	210	4.278	5.677	4.205	5.62
	260	4.399	5.691	4.309	5.625
	310	4.628	5.733	4.511	5.653

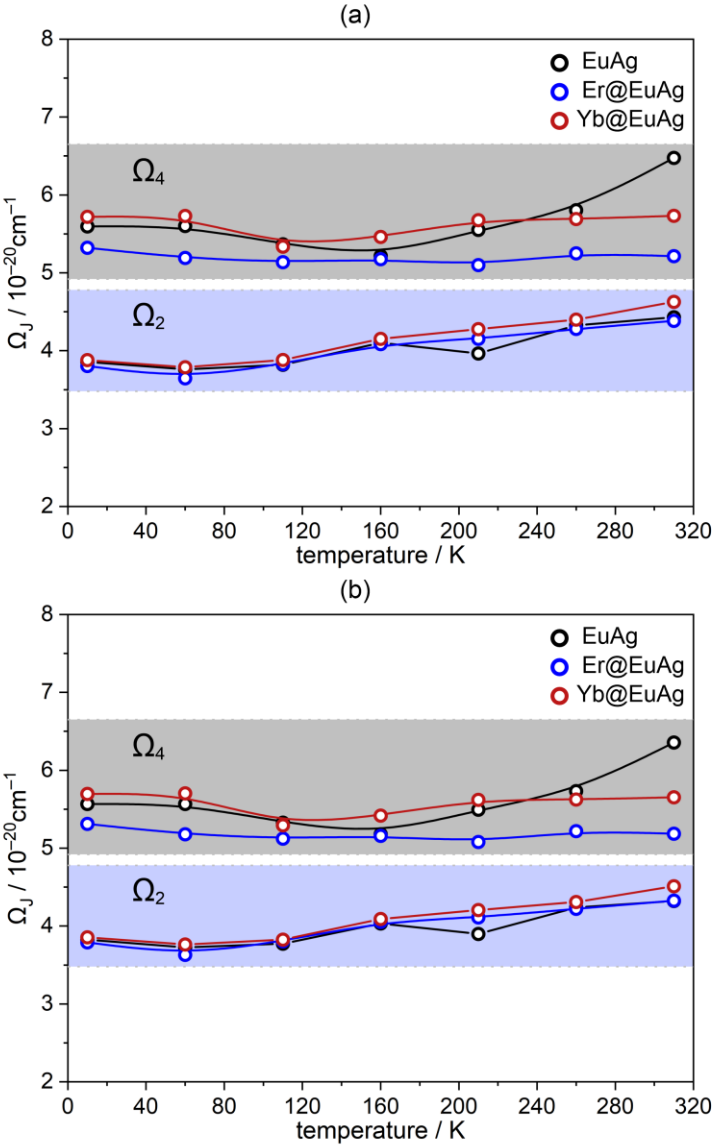

Fig. S57 Comparison of the temperature dependences of the Judd-Ofelt (JO) parameters, Ω_2 and Ω_4, for **EuAg**, **Er@EuAg**, and **Yb@EuAg** in the 10–310 K range, calculated based on the respective emission spectra with subtracted (a) and non-subtracted background (b). To visualize the temperature trends in the JO parameters, the B-spline line was used to connect the calculated parameters. Moreover, the color backgrounds were used to distinguish the temperature variations of the two different parameters.

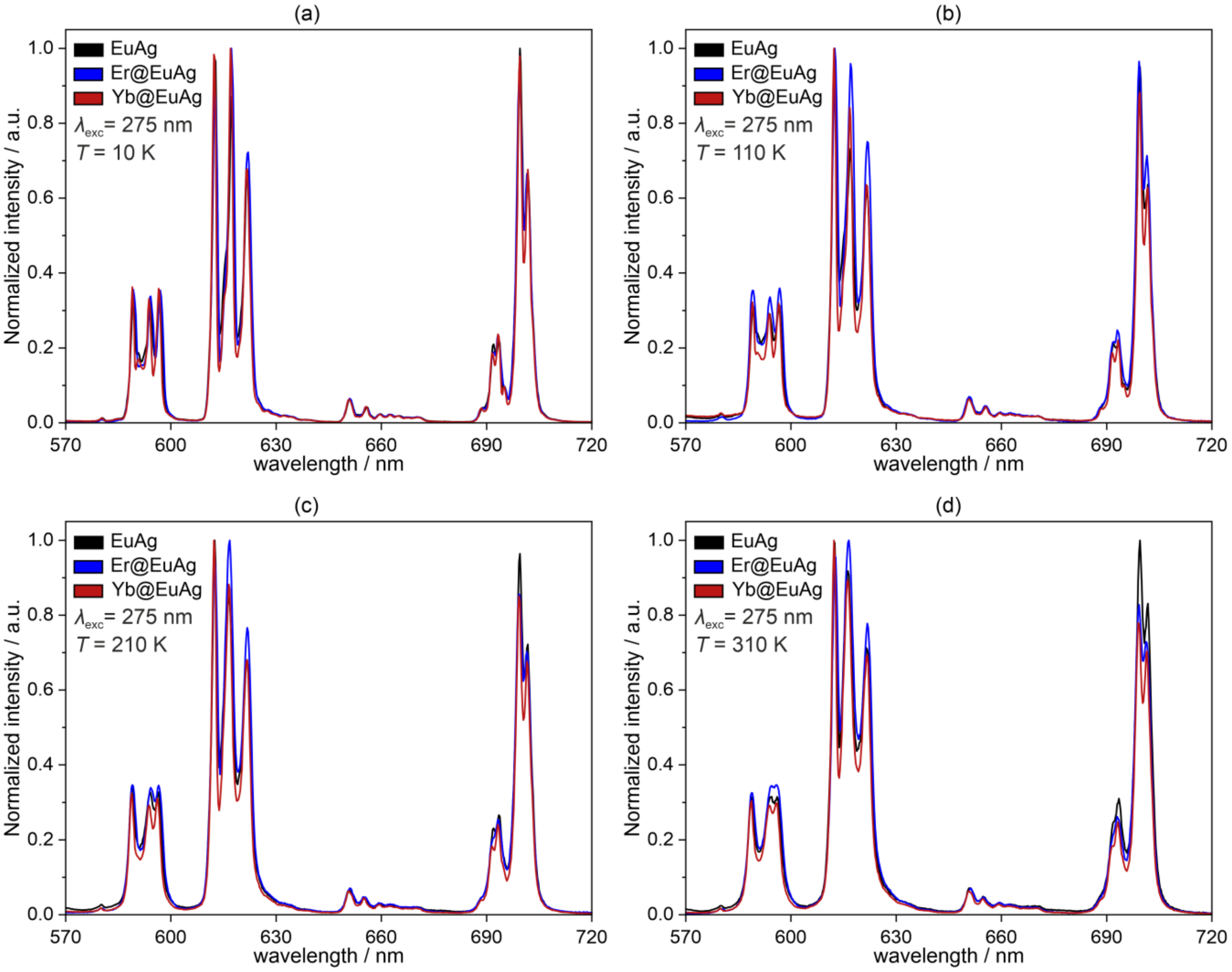

Fig. S58 Comparison of normalized emission spectra for **EuAg**, **Er@EuAg**, and **Yb@EuAg** under the excitation of λ_{exc} = 275 nm, presented in the 570−720 nm range; gathered at 10 K (a), 110 K (b), 210 K (c), and 310 K (d). Note that the energy shifts for the observed emission components related to the crystal-field sublevels of the excited $^5F_{1-4}$ states are very small upon the addition of Er(III) and Yb(III) centers, which agrees with the detected small structural changes and the resulting subtle variation of the electronic structure depicted by the *ab initio* calculations (see the main article for broader discussion and Table S34 below). More pronounced changes are observed for the relative intensities of these emission components, which can be correlated with the Er(III)- and Yb(III)-induced changes in the geometrical parameters of emissive Eu(III) complexes and the simultaneous changes in the phonon mode schemes within the crystal lattice affecting the long-range interactions within the investigated solid. For broader discussion, see the related part of the main article, including the discussion on the Judd-Ofelt parameters at variable temperatures (Table S33 and Fig. S57).

Table S34 (part 1/2) Energy splitting of $^7F_{0-5}$ terms and energy of $^5D_0$ of Eu^{III} complexes for **EuAg**, **Eu@ErAg**, and **Eu@YbAg**, where the results estimating the properties of **Eu@ErAg** was calculated for Eu(III) complexes artificially embedded into the **ErAg** framework without the structure optimization, and, analogously, the results estimating the properties of **Eu@YbAg** was calculated for Eu(III) complexes artificially embedded into the **YbAg** framework without the structure optimization (see the main article for details).

State	Term	Energy / cm^{-1}		
		EuAg	**Eu@ErAg**	**Eu@YbAg**
1	$^7F_0$	0.000	0.000	0.000
2	$^7F_1$	287.478	299.616	289.789
3		397.562	390.456	397.578
4		469.587	455.750	460.324
5	$^7F_2$	971.230	957.303	954.496
6		1027.049	1019.880	1013.863
7		1076.335	1067.181	1067.547
8		1136.378	1138.152	1143.116
9		1153.578	1153.033	1161.936
10	$^7F_3$	1940.156	1932.499	1933.451
11		1953.272	1948.426	1948.523
12		1956.331	1953.701	1955.179
13		1980.351	1971.412	1972.791
14		1992.923	1988.609	1987.215
15		2017.786	2015.394	2019.550
16		2040.786	2046.337	2051.190
17	$^7F_4$	2909.083	2876.744	2872.418
18		2963.400	2952.912	2948.967
19		2984.471	2979.933	2976.757
20		3007.669	2995.747	2995.180
21		3033.403	3026.728	3030.132
22		3060.456	3061.531	3064.689
23		3096.318	3100.279	3102.630
24		3120.115	3126.563	3134.232
25		3136. 086	3152.370	3160.567

Table S34 (part 2/2) Energy splitting of $^7F_{0\text{-}5}$ terms and energy of $^5D_0$ of Eu^{III} complexes for **EuAg**, **Eu@ErAg**, and **Eu@YbAg**, where the results estimating the properties of **Eu@ErAg** was calculated for Eu(III) complexes artificially embedded into the **ErAg** framework without the structure optimization, and, analogously, the results estimating the properties of **Eu@YbAg** was calculated for Eu(III) complexes artificially embedded into the **YbAg** framework without the structure optimization (see the main article for details).

State	Term	Energy / cm^{-1}		
		EuAg	**EuErAg**	**EuYbAg**
26	$^7F_5$	4058.267	4050.017	4043.058
27		4063.918	4056.250	4049.274
28		4111.083	4100.090	4095.126
29		4129.585	4125.029	4124.935
30		4169.857	4164.742	4159.592
31		4198.116	4196.070	4196.485
32		4236.823	4229.404	4234.231
33		4248.503	4241.456	4245.055
34		4250.863	4251.302	4255.522
35		4272.985	4273.591	4285.528
36		4278.621	4285.000	4296.508
37	$^5D_0$	5199.639	5215.301	5199.551

References to the Supporting Information

S1 A. Hoffman, M. Zychowicz, J. Wang, K. Matsuura, F. Kagawa, J. Rzepiela, M. Heczko, S. Baś, H. Tokoro, S. Ohkoshi and S. Chorazy, Photoluminescent, dielectric, and magnetic responsivity to the humidity variation in SHG-active pyroelectric manganese(II)-based molecular material, *Chem. Sci.*, 2025, **16**, 8979−8997.

S2 K. Kumar, G. Li, O. Stefanczyk, S. Chorazy, K. Nakabayashi and S. Ohkoshi, Slow magnetic relaxation in Nd(III) and Sm(III) complexes formed in three-dimensional lanthanide-dicyanidometallate(I) frameworks exhibiting luminescent properties, *J. Mater. Chem.* C, 2023, **11**, 1008–1020.

S3 Bruker. *APEX4*, *SAINT* and *SADABS*. Bruker AXS Inc., Madison, Wisconsin, USA, 2021.

S4 G. M. Sheldrick, SHELXT – Integrated space-group and crystal-structure determination, *Acta Crystallogr., Sect. A: Found. Adv.,* 2015, **71**, 3–8.

S5 L. J. Farrugia, *WinGX* and *ORTEP* for Windows: an update, *J. Appl. Crystallogr.,* 2012, **45**, 849–854.

S6 C. F. Macrae , I. Sovago, S. J. Cottrell, P. T. A. Galek, P. McCabe, E. Pidcock, M. Platings, G. P. Shields, J. S. Stevens, M. Towler and P. A. Wood, Mercury 4.0: from visualization to analysis, design and prediction, *J. Appl. Cryst*., 2020, **53**, 226–235.

S7 S. Chorazy, J. J. Zakrzewski, J. Wang, S. Ohkoshi and B. Sieklucka, Incorporation of hexacyanidoferrate(III) ion in photoluminescent trimetallic Eu(3-pyridone)[$Co_{1-x}Fe_x(CN)_6$] chains exhibiting tunable visible light absorption and emission properties, *CrystEngComm*, 2018, **20**, 5695–5706.

S8 M. Llunell, D. Casanova, J. Cirera, J. Bofill, P. Alemany, S. Alvarez, M. Pinsky and D. Avnir, *SHAPE v. 2.1. Program for the Calculation of Continuous Shape Measures of Polygonal and Polyhedral Molecular Fragments*, University of Barcelona: Barcelona, Spain, 2013.

S9 M. Liberka, M. Zychowicz, W. Zychowicz and S. Chorazy, Neutral dicyanidoferrate(II) metalloligands for the rational design of dysprosium(III) single-molecule magnets, *Chem. Commun*, 2022, **58**, 6381–6384.

S10 D. Casanova, J. Cirera, M. Llunell, P. Alemany, D. Avnir and S. Alvarez, Minimal Distortion Pathways in Polyhedral Rearrangements, *J. Am. Chem. Soc*., 2004, **126**, 1755–1763.

S11 G. Li Manni, I. Fdez. Galván, A. Alavi, et al. The OpenMolcas Web: A Community-Driven Approach to Advancing Computational Chemistry, *J. Chem. Theory. Comput.*, 2023, **19**, 6933–6991.

S12 B.O. Roos, R. Lindh, P.-A. Malmqvist, V. Veryazov, P.-O. Widmark, Main Group Atoms and Dimers Studied with a New Relativistic ANO Basis Set, *J. Phys. Chem. A*, 2004, **108**, 2851–2858.

S13 B.O. Roos, R. Lindh, P.-A. Malmqvist, V. Veryazov, P.-O. Widmark, New Relativistic ANO Basis Sets for Transition Metal Atoms, *J. Phys. Chem. A,* 2005, **109**, 6575–6579.

S14 B.O. Roos, R. Lindh, P.-A. Malmqvist, V. Veryazov, P.-O. Widmark, A. C. Borin, New Relativistic Atomic Natural Orbital Basis Sets for Lanthanide Atoms with Applications to the Ce Diatom and LuF_3, *J. Phys. Chem. A*, 2008, **112**, 11431–11435.

S15 P. A. Malmqvist, B. O. Roos and B. Schimmelpfennig, The restricted active space (RAS) state interaction approach with spin–orbit coupling, B., *Chem. Phys. Lett*., 2002, **357**, 230−240.

S16 B. A. Heß, C. M. Marian, U. Wahlgren and O. A. Gropen, A mean-field spin-orbit method applicable to correlated wavefunctions, *Chem. Phys. Lett*., 1996, **251**, 365−371.

S17 M. Zychowicz, H. Dzielak, J. Rzepiela and S. Chorazy, Synergy of Experiment and Broadened Exploration of Ab Initio Calculations for Understanding of Lanthanide–Pentacyanidocobaltate Molecular Nanomagnets and Their Optical Properties, *Inorg. Chem.*, 2024, **63**, 19213–19226.

S18 M. E. Lines, Orbital Angular Momentum in the Theory of Paramagnetic Clusters, *J. Chem. Phys.*, 1971, **55**, 2977–2984.

S19 K. Binnemans, Interpretation of europium(III) spectra, *Coord. Chem. Rev.*, 2015, **295**, 1–45.

S20 C. D. S. Brites, S. Balabhadra and L. D. Carlos, Lanthanide-Based Thermometers: At the Cutting-Edge of Luminescence Thermometry, *Adv. Opt. Mater.*, 2019, **7**, 1801239.

S21 A. Ćirić, S. Stojadinović, M. Sekulić, M.D. Dramićanin, JOES: An application software for Judd-Ofelt analysis from Eu^{3+} emission spectra, *J. Lumin.*, 2019, **205**, 351–356.

S22 C. Görller-Walrand, K. Binnemans, in *Handbook on the Physics and Chemistry of Rare Earths*, ed. K. A. Gschneidner Jr., L. Eyring, Elsevier, North-Holland, Volume 25, 1998, **167**, 101–264.

S23 M. P. Hehlen, M. G. Brik and K. W. Krämer, 50th anniversary of the Judd–Ofelt theory: An experimentalist's view of the formalism and its application, *J. Lumin*., 2013, **136**, 221–239.

S24 F. Pointillart, B. Le Guennic, S. Golhen, O. Cador, O. Maury and L. Ouahab, A redox-active luminescent ytterbium based single molecule magnet, *Chem. Commun*., 2013, **49**, 615–617.

S25 R. Marin, G. Brunet and M. Murugesu, Shining New Light on Multifunctional Lanthanide Single-Molecule Magnets, *Angew. Chem. Int. Ed*., 2021, **60**, 1728–1746.

S26 J. Wang, J. J. Zakrzewski, M. Zychowicz, Y. Xin, H. Tokoro, S. Chorazy and S. Ohkoshi, Desolvation-Induced Highly Symmetrical Terbium(III) Single-Molecule Magnet Exhibiting Luminescent Self-Monitoring of Temperature, *Angew. Chem. Int. Ed*., 2023, **62**, e202306372.